# Lattice studies of the $Sp(4)$ gauge theory with two fundamental and three antisymmetric Dirac fermions

Ed Bennett[ORCID],[1,*] Deog Ki Hong[ORCID],[2,†] Ho Hsiao,[3,‡] Jong-Wan Lee[ORCID],[2,4,§] C.-J. David Lin[ORCID],[3,5,6,‖] Biagio Lucini[ORCID],[7,1,¶] Michele Mesiti,[1,**] Maurizio Piai[ORCID],[8,††] and Davide Vadacchino[ORCID][9,10,‡‡]

[1]*Swansea Academy of Advanced Computing, Swansea University, Fabian Way, SA1 8EN Swansea, Wales, United Kingdom*
[2]*Department of Physics, Pusan National University, Busan 46241, Korea*
[3]*Institute of Physics, National Yang Ming Chiao Tung University, 1001 Ta-Hsueh Road, Hsinchu 30010, Taiwan*
[4]*Extreme Physics Institute, Pusan National University, Busan 46241, Korea*
[5]*Center for High Energy Physics, Chung-Yuan Christian University, Chung-Li 32023, Taiwan*
[6]*Centre for Theoretical and Computational Physics, National Yang Ming Chiao Tung University, 1001 Ta-Hsueh Road, Hsinchu 30010, Taiwan*
[7]*Department of Mathematics, Faculty of Science and Engineering, Swansea University, Fabian Way, SA1 8EN Swansea, Wales, United Kingdom*
[8]*Department of Physics, Faculty of Science and Engineering, Swansea University, Singleton Park, SA2 8PP, Swansea, Wales, United Kingdom*
[9]*School of Mathematics and Hamilton Mathematics Institute, Trinity College, Dublin 2, Ireland*
[10]*Centre for Mathematical Sciences, University of Plymouth, Plymouth, PL4 8AA, United Kingdom*

We consider the $Sp(4)$ gauge theory coupled to $N_f = 2$ fundamental and $n_f = 3$ antisymmetric flavors of Dirac fermions in four dimensions. This theory serves as the microscopic origin for composite Higgs models with $SU(4)/Sp(4)$ coset, supplemented by partial top compositeness. We study numerically its lattice realization, and couple the fundamental plaquette action to Wilson-Dirac fermions in mixed representations, by adopting a (rational) hybrid Monte Carlo method, to perform nontrivial tests of the properties of the resulting lattice theory. We find evidence of a surface (with boundaries) of first-order bulk phase transitions in the three-dimensional space of bare parameters (one coupling and two masses). Explicit evaluation of the Dirac eigenvalues confirms the expected patterns of global symmetry breaking. After investigating finite-volume effects in the weak-coupling phase of the theory, for the largest available lattice we study the mass spectra of the lightest spin-0 and spin-1 flavored mesons composed of fermions in each representation, and of the lightest half-integer spin composite particle made of fermions in different representations—the chimera baryon. This work sets the stage for future systematical studies of the nonperturbative dynamics in phenomenologically relevant regions of parameter space.

*e.j.bennett@swansea.ac.uk
†dkhong@pusan.ac.kr
‡thepaulxiao@gmail.com
§jwlee823@pusan.ac.kr
‖dlin@nycu.edu.tw
¶b.lucini@swansea.ac.uk
**michele.mesiti@swansea.ac.uk
††m.piai@swansea.ac.uk
‡‡davide.vadacchino@plymouth.ac.uk

## I. INTRODUCTION

The Standard Model (SM) of particle physics is an astonishing achievement, as it provides an outstanding wealth of correct predictions and (in selected cases) with uncommonly high accuracy. Yet, it is unlikely to be the complete and final description of fundamental physics, given, for example, that it does not include gravity, that many of its interactions are not asymptotically safe at short distances [the $U(1)_Y$ coupling, all the Yukawa couplings, and the scalar self-coupling have positive beta function], that it does not provide a compelling explanation for dark matter, for inflationary cosmology, and for the observed baryon asymmetry of our universe. Hence, the theoretical and experimental search for new physics extending beyond the standard model (BSM) is as active a field today as ever.

It is a remarkable fact, suggestive of promising new search directions, that both the two latest additions to the SM spectrum of particles have properties somewhat unusual for—though not inconsistent with—the low-energy effective field theory (EFT) paradigm, according to which the SM would be accurate only up to a new physics scale $\Lambda$, higher than the electroweak scale $v_W \simeq 246$ GeV. The mass of the top quark ($m_t \sim 173$ GeV) is orders of magnitude larger than that of other fermions, which in the SM context implies that its Yukawa coupling is comparatively large—so much so that its effects in radiative (quantum) corrections might be invoked as a possible cause for the vacuum instability that triggers electroweak symmetry breaking (EWSB). Conversely, naive dimensional analysis (NDA) arguments suggest the mass $m_h$ of the Higgs boson should be sensitive to $\Lambda$, which indirect and direct searches at the Large Hadron Collider (LHC) put in the multi-TeV range. But, experimentally, $m_h \simeq 125$ GeV [1,2], leading to the little hierarchy $m_h \ll \Lambda$. These two observations suggest that Higgs and top physics might be sensitive to new physics, and motivate many proposals for extensions of the standard model, including the one we will focus on in the following.

This paper is inspired by the theoretical proposal in Ref. [3], which postulates the existence of a new, strongly coupled fundamental theory with $Sp(4)$ gauge group, interprets the SM Higgs-doublet fields in terms of the composite pseudo-Nambu-Goldstone bosons (PNGBs) describing the spontaneous breaking of an approximate $SU(4)$ symmetry [acting on $N_f = 2$ Dirac fermions transforming on the fundamental representation of $Sp(4)$] to its $Sp(4)$ subgroup, and furthermore reinterprets the SM top quark as a partially composite object, resulting from the mixing with composite fermions, dubbed chimera baryons [the constituents of which are an admixture of fermions transforming in the fundamental and antisymmetric representation of $Sp(4)$]. In the rest of this introduction, we explain why this model is particularly interesting, standing out in the BSM literature. The body of the paper is devoted to reporting a set of lattice results demonstrating that our collaboration has put in place and tested successfully all the lattice field theory tools that are necessary to perform a systematic, quantitative analysis of the nonperturbative features of this strongly coupled theory.

The common feature to composite Higgs models (CHMs) is that scalar fields originate as PNGBs in the underlying dynamics [4–6]. Symmetry arguments constrain their potential, suppressing masses and couplings. Reviews can be found in Refs. [7–9], and it may be helpful to the reader to use the summary tables in Refs. [10–12]. A selection of interesting studies focusing on model-building, perturbative studies, and phenomenological applications includes Refs. [13–50]. In these studies, EFT (and perturbative) arguments and guidance from the experiment are combined to constrain the strongly coupled dynamics,

but its detailed description is accessible only with nonperturbative instruments. There is a rich literature on the topic coming from gauge-gravity dualities, in the context of bottom-up holographic models [51–53], with a recent resurgence of interest [54–57], including a first attempt at identifying a complete top-down model [58]. Alternative ways to approach the dynamics have also been proposed in Ref. [59].

Lattice field theory is the most direct, first principle way to approach nonperturbative dynamics. Detailed lattice studies of theories leading to symmetry breaking described by the $SU(4)/Sp(4) \sim SO(6)/SO(5)$ coset have focused on the simplest $SU(2)$ gauge theories coupled to fundamental fermions [60–68], but these models cannot realize top compositeness. Explorations of $SU(4)$ gauge theories with multiple representations [69–74] aim at gathering nonperturbative information about Ferretti's $SU(5)/SO(5)$ model [21], though the fermionic field contents do not match. An alternative route to studying models yielding both composite Higgs and partial top compositeness has been proposed by Vecchi in Ref. [75] (see also Refs. [76,77]), by exploiting the fact that in $SU(3)$ theories the antisymmetric representation is the conjugate of the fundamental, so that one can use the lattice information made available over the years by the LatKMI [78,79] and LSD [80–84] collaborations to test the viability of CHMs based on the $SU(N_f) \times SU(N_f)/SU(N_f)$ cosets (as done explicitly in Ref. [85]).

Our collaboration announced in 2017 the intention to carry out a systematic study of confining lattice gauge theories in the $Sp(2N)$ sequence, coupled to various types of fermion matter fields [86]. We have published results for the $Sp(4)$ gauge theory coupled to $N_f = 2$ dynamical fermions transforming in the fundamental representation of the group [87,88], and for quenched fermions in mixed (fundamental and antisymmetric) representations [89]. We have calculated the spectra of glueballs and strings in the $Sp(2N)$ Yang-Mills theories [90,91]—reaching far beyond the pioneering lattice work for $N = 2, 3$ in Ref. [92]. Besides the ambitious applications in the CHM context, an equally important physics motivation relates to models of dark matter with strong-coupling origin [93–95] (see also the more recent Refs. [96–103]). On more general grounds, we aim at putting our numerical understanding of these theories on a level comparable to that achieved for the $SU(N_c)$ theories, in reference to the approach to the large-$N_c$ limit [104–113], but also for the purposes of determining the boundaries of the conformal window [114–117], and of testing their EFT description [118]. We will deliver further publications on the topology of $Sp(2N)$ gauge theories, and their quenched meson spectra, as well as on the (partially quenched) dynamical theory with $n_f = 3$ dynamical antisymmetric fermions—preliminary results have been presented in Refs. [119,120].

Our diversified lattice strategy combines exploratory as well as precision studies, moving in different directions in the space of $Sp(2N)$ theories. Aside from the aforementioned desire to explore other applications of these theories, even when we restrict attention to the CHM context, there are still two good reasons to adopt this gradual approach. First, the CHM candidate proposed in Ref. [3] is rather unusual, and there are no reference results in the literature for comparable theories. It is hence important to build a whole portfolio of related theories, against which we can benchmark our results. The pragmatic reason why this benchmarking is needed is that lattice studies with fermions in mixed representations are technically challenging and resource intensive. Most of the existing, publicly available lattice codes developed for other purposes do not implement multiple dynamical representations—we mentioned above some very recent examples for the $SU(4)$ theories. Even after the code becomes available, and after testing the correctness of the behavior of the algorithms used in the calculations—as we shall demonstrate shortly—one still must explore the phase space of the lattice theory. In our case, this is controlled by three bare parameters (the gauge coupling and the two fermion masses), besides the lattice size, making the mapping of phase transitions quite nontrivial. Finally, the number of elementary degrees of freedom of the $Sp(4)$ theory with $N_f = 2$ and $n_f = 3$ is large, and hence, while the theory is still asymptotically free, one expects slow running of the couplings, and possibly the emergence of large anomalous dimensions, making it more challenging to characterize the theory. We will provide evidence of the fact that we can address all of these challenges, and we can start production of ensembles giving access to physically relevant regions of parameter space.

The paper is organized as follows. We start by presenting essential information about the continuum theory in Sec. II. This exercise makes the paper self-contained, and allows us to connect to potential applications, prominently to CHMs. We then describe the lattice theory in Sec. III, by providing enough details about the algorithms we use to allow reproducibility of our results. Section IV defines the main observable quantities we use to probe our lattice theory. Out numerical results for these observables are presented in Sec. V. We conclude with the summary and outlook in Sec. VI. We supplement the paper by Appendix A, detailing some of the conventions we adopted throughout the paper, Appendix B, which displays an additional technical test we performed on 2-point functions involving chimera baryon operators, and Appendix C, containing summary tables characterizing the numerical data used for the analysis.

## II. THE MODEL

The model we study has been proposed in Ref. [3]. We adapt and improve the conventions in Ref. [89], to make both the presentation in the paper self-contained and the notation precise enough to make contact with the lattice. We hence review the field content and symmetries of the continuum theory defining its short-distance dynamics, and review its low-energy EFT description. We supplement the list of interpolating operators used for the study of mesons (already published elsewhere) by presenting original material detailing the operators used for chimera baryons.

### A. Short distance dynamics

The $Sp(4)$ gauge theory has field content consisting of $N_f = 2$ Dirac fermions $Q^{i\,a}$ transforming in the fundamental, $(f)$, representation of the gauge group, and $n_f = 3$ Dirac fermions $\Psi^{k\,ab}$ transforming in the 2-index antisymmetric, $(as)$, representation. Here and in the following, $a, b = 1, \ldots, 4$ denote color indices, while $i = 1, 2$ and $k = 1, 2, 3$ denote flavor indices. The Lagrangian density is

$$\mathcal{L} = -\frac{1}{2}\mathrm{Tr}V_{\mu\nu}V^{\mu\nu} + \frac{1}{2}\sum_{i=1}^{2}(i\overline{Q^i}_a\gamma^\mu(D_\mu Q^i)^a - i\overline{D_\mu Q^i}_a\gamma^\mu Q^{ia})$$
$$- m^f\sum_{i=1}^{2}\overline{Q^i}_a Q^{ia} + \frac{1}{2}\sum_{k=1}^{3}(i\overline{\Psi^k}_{ab}\gamma^\mu(D_\mu\Psi^k)^{ab}$$
$$- i\overline{D_\mu\Psi^k}_{ab}\gamma^\mu\Psi^{kab}) - m^{as}\sum_{k=1}^{3}\overline{\Psi^k}_{ab}\Psi^{kab}, \quad (1)$$

where summations over color and Lorentz indices are understood, while spinor indices are implicit. $m^f$ and $m^{as}$ are the (degenerate) masses of $Q$ and $\Psi$, respectively. The covariant derivatives are defined by making use of the transformation properties under the action of an element $U$ of the $Sp(4)$ gauge group—$Q \to UQ$ and $\Psi \to U\Psi U^\mathrm{T}$— so that

$$V_{\mu\nu} \equiv \partial_\mu V_\nu - \partial_\nu V_\mu + ig[V_\mu, V_\nu], \quad (2)$$
$$D_\mu Q^i = \partial_\mu Q^i + igV_\mu Q^i, \quad (3)$$
$$D_\mu\Psi^k = \partial_\mu\Psi^k + igV_\mu\Psi^k + ig\Psi^k V_\mu^\mathrm{T}, \quad (4)$$

where $g$ is the gauge coupling.

Because of the pseudoreal nature of the representations of $Sp(4)$, it is convenient to split each Dirac fermion into 2-component spinors $q^{m\,a}$ and $\psi^{n\,ab}$, for the $(f)$ and $(as)$ representation, respectively. The flavor indices $m = 1, \ldots, 4$ and $n = 1, \ldots, 6$ denote the components of a fundamental representation of the global symmetry groups $SU(4)$ acting on $q^{m\,a}$ and $SU(6)$ acting on $\psi^{n\,ab}$. Here and in the following we ignore the $U(1)$ factors in the symmetry group. The field content is summarized in Table I. To make

TABLE I. Field content of the microscopic theory. $Sp(4)$ is the gauge group, and $SU(4) \times SU(6)$ (ignoring Abelian factors) the global one. The elementary fields $V_\mu$ are gauge bosons, and $q$ and $\psi$ are 2-component spinors, described in the main text.

| Fields | $Sp(4)$ | $SU(4)$ | $SU(6)$ |
|---|---|---|---|
| $V_\mu$ | 10 | 1 | 1 |
| $q$ | 4 | 4 | 1 |
| $\psi$ | 5 | 1 | 6 |

the symmetries manifest, we borrow Eqs. (5) and (6) from Ref. [89], and introduce the symplectic matrix $\Omega$ and the symmetric matrix $\omega$, that are defined by

$$\Omega = \Omega_{mn} = \Omega^{mn} \equiv \begin{pmatrix} 0 & 0 & 1 & 0 \\ 0 & 0 & 0 & 1 \\ -1 & 0 & 0 & 0 \\ 0 & -1 & 0 & 0 \end{pmatrix},$$

$$\omega = \omega_{mn} = \omega^{mn} \equiv \begin{pmatrix} 0 & 0 & 0 & 1 & 0 & 0 \\ 0 & 0 & 0 & 0 & 1 & 0 \\ 0 & 0 & 0 & 0 & 0 & 1 \\ 1 & 0 & 0 & 0 & 0 & 0 \\ 0 & 1 & 0 & 0 & 0 & 0 \\ 0 & 0 & 1 & 0 & 0 & 0 \end{pmatrix}. \tag{5}$$

The 2-component notation is related as follows to the 4-component notation:

$$Q^{i\,a} = \begin{pmatrix} q^{i\,a} \\ \Omega^{ab}(-\tilde{C}q^{i+2*})_b \end{pmatrix},$$

$$\Psi^{k\,ab} = \begin{pmatrix} \psi^{k\,ab} \\ \Omega^{ac}\Omega^{bd}(-\tilde{C}\psi^{k+3*})_{cd} \end{pmatrix}, \tag{6}$$

where $\tilde{C} = -i\tau^2$ is the charge-conjugation matrix, and $\tau^2$ the second Pauli matrix. The Lagrangian density can then be rewritten as follows:

$$\mathcal{L} = -\frac{1}{2}\mathrm{Tr}V_{\mu\nu}V^{\mu\nu} + \frac{1}{2}\sum_{m=1}^{4}(i(q^m)_a^\dagger\bar{\sigma}^\mu(D_\mu q^m)^a - i(D_\mu q^m)_a^\dagger\bar{\sigma}^\mu q^{m\,a}) - \frac{1}{2}m^f\sum_{m,n=1}^{4}\Omega_{mn}(q^{m\,a\,T}\Omega_{ab}\tilde{C}q^{n\,b} - (q^m)_a^\dagger\Omega^{ab}\tilde{C}(q^{n*})_b)$$

$$+ \frac{1}{2}\sum_{m=1}^{6}(i(\psi^m)_{ab}^\dagger\bar{\sigma}^\mu(D_\mu\psi^m)^{ab} - i(D_\mu\psi^m)_{ab}^\dagger\bar{\sigma}^\mu\psi^{m\,ab}) - \frac{1}{2}m^{as}\sum_{m,n=1}^{6}\omega_{mn}(\psi^{m\,ab\,T}\Omega_{ac}\Omega_{bd}\tilde{C}\psi^{n\,cd} - (\psi^m)_{ab}^\dagger\Omega^{ac}\Omega^{bd}\tilde{C}(\psi^{n*})_{cd}), \tag{7}$$

where the kinetic terms for the 2-component spinors are written by making use of the $2 \times 2$ matrices $\bar{\sigma}^\mu \equiv (\mathbb{1}_2, \tau^i)$.

The structure of the Dirac mass terms, rewritten in this 2-component formalism, shows that as long as $m^f \neq 0 \neq m^{as}$, the non-Abelian global symmetry groups $SU(4)$ and $SU(6)$ are explicitly broken to their $Sp(4)$ and $SO(6)$ maximal subgroups, respectively. Vacuum alignment arguments then imply that, as long as these are the only symmetry-breaking terms in the Langrangian density, if fermion bilinear condensates emerge they spontaneously break the global symmetries according to the same breaking pattern [121].

## B. Long distance dynamics

The dynamics of the underlying theory gives rise to $15 - 10 = 5$ PNGBs describing the $SU(4)/Sp(4)$ coset, and $35 - 15 = 20$ PNGBs spanning the $SU(6)/SO(6)$ coset. Following Ref. [89], we divide the 15 generators $T^A$ of the global $SU(4)$, and 35 generators $t^B$ of $SU(6)$, in two sets by denoting with $A = 1, \ldots, 5$ and with $B = 1, \ldots, 20$ the broken ones, which obey the following relations:

$$\Omega T^A - T^{A\,T}\Omega = 0, \qquad \omega t^B - t^{B\,T}\omega = 0. \tag{8}$$

The unbroken generators have adjoint indices $A = 6, \ldots, 15$ and $B = 21, \ldots, 35$. They satisfy the relations:

$$\Omega T^A + T^{A\,T}\Omega = 0, \qquad \omega t^B + t^{B\,T}\omega = 0. \tag{9}$$

As long as the masses $m^f$ and $m^{as}$ are smaller than the dynamically generated, chiral symmetry-breaking scale of the theory, one expects long-distance dynamics to be well captured by an EFT providing the description of the PNGBs as weakly coupled scalar fields. To this purpose, we introduce two nonlinear sigma-model fields. The matrix-valued $\Sigma_6$ transforms as $\Omega_{ab}q^{m\,a\,T}\tilde{C}q^{n\,b}$ in the antisymmetric representation of the global $SU(4)$. $\Sigma_{21}$ has the quantum numbers of $-\Omega_{ab}\Omega_{cd}\psi^{m\,ac\,T}\tilde{C}\psi^{n\,bd}$, and transforms in the symmetric representation of the $SU(6)$ global symmetry.

In the vacuum, the antisymmetric representation decomposes as $6 = 1 \oplus 5$ of the unbroken $Sp(4)$, and the symmetric as $21 = 1 \oplus 20$ of $SO(6)$; the nonlinear sigma-model fields can be parametrized by the PNGB fields $\pi_5$ and $\pi_{20}$ as

$$\Sigma_6 \equiv e^{\frac{2i\pi_5}{f_5}}\Omega = \Omega e^{\frac{2i\pi_5^T}{f_5}}, \qquad \Sigma_{21} \equiv e^{\frac{2i\pi_{20}}{f_{20}}}\omega = \omega e^{\frac{2i\pi_{20}^T}{f_{20}}}. \tag{10}$$

The decay constants are denoted by $f_5$ and $f_{20}$.[1] To write the EFT Lagrangian density, we further replace the mass terms with (nondynamical) spurion fields $M_6 \equiv m^f\Omega$ and

---

[1]These conventions are chosen so that, when applied to the QCD chiral Lagrangian, the decay constant is $f_\pi \simeq 93$ MeV.

$M_{21} \equiv -m^{as}\omega$. At the leading order in both the derivative expansion and the expansion in small masses, the Lagrangian density for the PNGBs of the $SU(4)/Sp(4)$ breaking takes the form

$$\mathcal{L}_6 = \frac{f_5^2}{4} \text{Tr}\{\partial_\mu \Sigma_6 (\partial^\mu \Sigma_6)^\dagger\} - \frac{v_6^3}{4} \text{Tr}\{M_6 \Sigma_6\} + \text{H.c.}$$

$$= \text{Tr}\{\partial_\mu \pi_5 \partial^\mu \pi_5\} + \frac{1}{3 f_5^2} \text{Tr}\{[\partial_\mu \pi_5, \pi_5][\partial^\mu \pi_5, \pi_5]\} + \cdots + \tag{11}$$

$$+ \frac{1}{2} m^f v_6^3 \text{Tr}(\Sigma_6 \Sigma_6^\dagger) - \frac{m^{(f)} v_6^3}{f_5^2} \text{Tr}\pi_5^2 + \frac{m^f v_6^3}{3 f_5^4} \text{Tr}\pi_5^4 + \cdots, \tag{12}$$

where $v_6$ parametrizes the condensate. The matrix of the five PNGBs in the $SU(4)/Sp(4)$ coset can be written as follows [89]:

$$\pi_5(x) = \frac{1}{2\sqrt{2}} \begin{pmatrix} \pi^3(x) & \pi^1(x) - i\pi^2(x) & 0 & -i\pi^4(x) + \pi^5(x) \\ \pi^1(x) + i\pi^2(x) & -\pi^3(x) & i\pi^4(x) - \pi^5(x) & 0 \\ 0 & -i\pi^4(x) - \pi^5(x) & \pi^3(x) & \pi^1(x) + i\pi^2(x) \\ i\pi^4(x) + \pi^5(x) & 0 & \pi^1(x) - i\pi^2(x) & -\pi^3(x) \end{pmatrix}. \tag{13}$$

The expansion for the $SU(6)/SO(6)$ PNGBs is formally identical—thanks to the opposite signs we chose in the definition of the mass matrices, ultimately deriving from the fact that $\Omega^2 = -\mathbb{1}_4$, while $\omega^2 = \mathbb{1}_6$—and one just replaces $v_6 \to v_{21}$, and analogous replacements for other quantities.[2] For instance, the matrix $\pi_{20}$ describing the PNGBs can be written as $\pi_{20}(x) = \sum_{B=1}^{20} \pi^B(x) t^B$, where $t^B$ are the aforementioned broken generators of $SU(6)$.

As explained in detail in Ref. [89], one can extend the EFT description to include the behavior of the lightest vector and axial-vector states, besides the PNGBs, by applying the principles of hidden local symmetry (HLS) [122–126] (see also [118,127–129]). There are well-known limitations to the applicability of this type of EFT treatment, and while we intend to come back to this topic in future publications, we will not explore it further in this study.

### 1. Coupling to the Standard Model

This paper studies the $Sp(4)$ gauge dynamics coupled only to ($f$) and ($as$) fermions. Nevertheless, to motivate it in terms of composite Higgs and partial top compositeness, we recall briefly how the model can be (weakly) coupled to the SM gauge fields of the $SU(3)_c \times SU(2)_L \times U(1)_Y$ gauge group—details can be found in Refs. [3,10,12,89].

The $SU(4)/Sp(4)$ coset is relevant to EWSB. The $SU(2)_L \times SU(2)_R \sim SO(4)$ symmetry of the SM Higgs potential is a subgroup of the unbroken $Sp(4)$. The unbroken subgroup $SO(4) \sim SU(2)_L \times SU(2)_R$ has the following generators:

$$T_L^1 = \frac{1}{2} \begin{pmatrix} 0 & 0 & 1 & 0 \\ 0 & 0 & 0 & 0 \\ 1 & 0 & 0 & 0 \\ 0 & 0 & 0 & 0 \end{pmatrix}, \quad T_L^2 = \frac{1}{2} \begin{pmatrix} 0 & 0 & -i & 0 \\ 0 & 0 & 0 & 0 \\ i & 0 & 0 & 0 \\ 0 & 0 & 0 & 0 \end{pmatrix},$$

$$T_L^3 = \frac{1}{2} \begin{pmatrix} 1 & 0 & 0 & 0 \\ 0 & 0 & 0 & 0 \\ 0 & 0 & -1 & 0 \\ 0 & 0 & 0 & 0 \end{pmatrix}, \tag{14}$$

$$T_R^1 = \frac{1}{2} \begin{pmatrix} 0 & 0 & 0 & 0 \\ 0 & 0 & 0 & 1 \\ 0 & 0 & 0 & 0 \\ 0 & 1 & 0 & 0 \end{pmatrix}, \quad T_R^2 = \frac{1}{2} \begin{pmatrix} 0 & 0 & 0 & 0 \\ 0 & 0 & 0 & -i \\ 0 & 0 & 0 & 0 \\ 0 & i & 0 & 0 \end{pmatrix},$$

$$T_R^3 = \frac{1}{2} \begin{pmatrix} 0 & 0 & 0 & 0 \\ 0 & 1 & 0 & 0 \\ 0 & 0 & 0 & 0 \\ 0 & 0 & 0 & -1 \end{pmatrix}. \tag{15}$$

In decomposing $Sp(4) \to SO(4)$, the PNGBs decompose as $5 = 1 \oplus 4$, where the $4 \sim 2_{\mathbb{C}}$ is the Higgs doublet. More explicitly, the real fields $\pi^1$, $\pi^2$, $\pi^4$, and $\pi^5$ combine into the 4 of $SO(4)$. The remaining $\pi^3$ is a SM singlet. The hypercharge assignments for the five PNGBs correspond to the action of the $T_R^3$ diagonal generator of $SU(2)_R$.

The $SU(6)/Sp(6)$ coset plays the important part of introducing color $SU(3)_c$, as the diagonal combination of the natural $SU(3)_L \times SU(3)_R$ subgroup of $SU(6)$. The PNGBs decompose as $20 \sim 8 \oplus 6_{\mathbb{C}}$ under $SU(3)_c$. An additional $U(1)_X$ subgroup of $SO(6)$ commutes with $SU(3)_L \times SU(3)_R$, so that the SM hypercharge $U(1)_Y$ is

---

[2]The trace of the identity matrix may introduce numerical factors that differ in the two expansions. In the $SU(4)/Sp(4)$ case $\text{Tr}\Sigma_6 \Sigma_6^\dagger = 4$, while in the $SU(6)/SO(6)$ case $\text{Tr}\Sigma_{21}\Sigma_{21}^\dagger = 6$.

a linear combination of $U(1)_X$ and the $U(1)$ group generated by the aforementioned $T_R^3$.

With these assignments of quantum numbers, composite fermion operators emerge which combine two ($f$) fermions $Q$ [to make a $SU(2)_L$ doublet] and one ($a s$) fermion $\Psi$ [a triplet of $SU(3)_c$]. The resulting chimera baryon has the same quantum numbers as a SM quark. These are massive Dirac fermions. Elementary SM fermions, in particular the top and bottom quarks, can couple to them. This can be achieved in two ways: either by coupling an SM bilinear operator to a meson of the strong coupling theory—effectively reproducing in the low-energy EFT a Yukawa coupling—or, alternatively, by coupling a (chiral) SM fermion to a chimera baryon.

The gauging of the SM gauge group introduces a new explicit source of breaking of the global symmetries (besides the mass terms). An analysis of the one-loop effective potential, along the lines of Ref. [130], yields additional contributions to the masses of the PNGBs, which are in general divergent, but controlled by the small, perturbative couplings of the SM gauge fields circulating in the loops. Furthermore, they introduce an instability in the Higgs effective potential: the negative sign of fermion loops ultimately triggers EWSB. Because of the weakness of the couplings, these effects can be arranged to be small, and yield a value for $v_W$ that is smaller than the decay constant of the PNGBs as it would emerge in isolation, from the strong dynamics sector only. In the literature, the combination of these phenomena goes under the name of vacuum misalignment.

If the strongly coupled regime of the underlying dynamics is very different from that of a QCD-like theory—in particular if the theory has enough fermions to be close to the conformal window—the emergence of large anomalous dimensions may enhance the effective couplings at low energy, hence explaining why the top quark mass is large. This is one motivation for composite Higgs models with partial top compositeness, and this model provides the simplest template. Similar ideas were put forward a long time ago, in the context of walking technicolor (see for instance Refs. [131,132]), top compositeness [133], and warped extra dimensions [134,135]. It would go beyond our scope to review the rich literature on the subject, and we refer the interested reader to the discussion in Ref. [136], in the context of dilaton-Higgs models, and to follow the references therein.

Lattice studies provide nonperturbative information that is essential for the program of phenomenological applications described in this subsection, with potentially transformative reach. As we shall demonstrate in the body of the paper, our research program has reached the stage at which we can compute the spectrum of masses and decay constants of the composite particles (mesons and chimera baryons). In the future, we will further improve our numerical studies in order to measure other quantities,

such as the size of the condensates, the scaling dimension of the operators in the nonperturbative regime, the magnitude of nontrivial matrix elements that feed into the effective potential for the PNGBs, and scattering amplitudes of mesons.

### C. Of mesons and chimera baryons

While it is easier to discuss the symmetries of the system by writing the fermions in the 2-component notation, we revert to 4-component spinors to prepare for the lattice numerical studies. In switching to the 4-component spinor notation, it is useful to explicitly write the charge-conjugated spinors as follows:

$$Q_C^{ia} \equiv \begin{pmatrix} q^{N_f+ia} \\ -\Omega^{ab}(\tilde{C}q^{i*})_b \end{pmatrix}, \tag{16}$$

$$\Psi_C^{iab} \equiv \begin{pmatrix} \psi^{n_f+iab} \\ -\Omega^{ac}\Omega^{bd}(\tilde{C}\psi^{i*})_{cd} \end{pmatrix}. \tag{17}$$

The meson operators sourcing the five PNGBs are the following:

$$\begin{aligned} \mathcal{O}_{\text{PS},1} &= (\overline{Q^{1a}}\gamma^5 Q^{2a} + \overline{Q^{2a}}\gamma^5 Q^{1a}), \\ \mathcal{O}_{\text{PS},2} &= i(-\overline{Q^{1a}}\gamma^5 Q^{2a} + \overline{Q^{2a}}\gamma^5 Q^{1a}), \\ \mathcal{O}_{\text{PS},3} &= (\overline{Q^{1a}}\gamma^5 Q^{1a} - \overline{Q^{2a}}\gamma^5 Q^{2a}), \\ \mathcal{O}_{\text{PS},4} &= -i(\overline{Q^{1a}}Q_C^{2a} + \overline{Q_C^{2a}}Q^{1a}), \\ \mathcal{O}_{\text{PS},5} &= i(-i\overline{Q^{1a}}Q_C^{2a} + i\overline{Q_C^{2a}}Q^{1a}). \end{aligned} \tag{18}$$

We expect the lightest states of the theory to appear in 2-point correlation functions of these operators.

The theory possesses also an anomalous, axial $U(1)_A$, which is both spontaneously and explicitly broken (by the mass term, as well as the anomaly). Hence, there are $U(1)_A$ partners to the meson operators, sourcing the counterparts of the $a_0$ particles of QCD, that can be obtained by replacing $\mathbb{1}_4 \to i\gamma^5$ inside the expressions in Eqs. (18), to yield:

$$\begin{aligned} \mathcal{O}'_{\text{PS},1} &= i(\overline{Q^{1a}}Q^{2a} + \overline{Q^{2a}}Q^{1a}), \\ \mathcal{O}'_{\text{PS},2} &= (\overline{Q^{1a}}Q^{2a} - \overline{Q^{2a}}Q^{1a}), \\ \mathcal{O}'_{\text{PS},3} &= i(\overline{Q^{1a}}Q^{1a} - \overline{Q^{2a}}Q^{2a}), \\ \mathcal{O}'_{\text{PS},4} &= (\overline{Q^{1a}}\gamma^5 Q_C^{2a} + \overline{Q_C^{2a}}\gamma^5 Q^{1a}), \\ \mathcal{O}'_{\text{PS},5} &= i(\overline{Q^{1a}}\gamma^5 Q_C^{2a} - \overline{Q_C^{2a}}\gamma^5 Q^{1a}). \end{aligned} \tag{19}$$

Mesons made of $\Psi^{iab}$ are built in a similar way, and we do not list them explicitly—details can be found in Ref. [89].

The chimera baryons we are interested in must have the same quantum numbers as the SM quarks, which transform

as a (2,2) of $SU(2)_L \times SU(2)_R$ in the standard model. But they also carry $SU(3)_c$ color, and hence require inserting $\Psi^{i\,ab}$, with $i = 1, 2, 3$ being identified with the QCD color index. A simple way to achieve this and build a $Sp(4)$ singlet is to rewrite, in the first line of Eqs. (18), $Q^{2\,a} = Q^{2\,b}\delta^a{}_b$ and $Q^{1\,a} = Q^{1\,b}\delta^a{}_b$, and then replace $\delta^a{}_b \rightarrow P_{L,R}\Psi^{k\,ac}\Omega_{cb}$, where

$$P_{L,R} \equiv \frac{1}{2}(\mathbb{1}_4 \pm \gamma_5). \qquad (20)$$

After performing the same substitution on all the mesons, we obtain a list of chimera baryon operators $\mathcal{O}_{\mathrm{CB}}^{L,R}$:

$$\mathcal{O}_{\mathrm{CB},1}^{L,R} = (\overline{Q^{1\,a}}\gamma^5 Q^{2\,b} + \overline{Q^{2\,a}}\gamma^5 Q^{1\,b})\Omega_{bc}P_{L,R}\Psi^{k\,ca},$$

$$\mathcal{O}_{\mathrm{CB},2}^{L,R} = i(-\overline{Q^{1\,a}}\gamma^5 Q^{2\,b} + \overline{Q^{2\,a}}\gamma^5 Q^{1\,b})\Omega_{bc}P_{L,R}\Psi^{k\,ca},$$

$$\mathcal{O}_{\mathrm{CB},3}^{L,R} = (\overline{Q^{1\,a}}\gamma^5 Q^{1\,b} - \overline{Q^{2\,a}}\gamma^5 Q^{2\,b})\Omega_{bc}P_{L,R}\Psi^{k\,ca},$$

$$\mathcal{O}_{\mathrm{CB},4}^{L,R} = -i(\overline{Q^{1\,a}}Q_C^{2\,b} + \overline{Q_C^{2\,a}}Q^{1\,b})\Omega_{bc}P_{L,R}\Psi^{k\,ca},$$

$$\mathcal{O}_{\mathrm{CB},5}^{L,R} = i(-i\overline{Q^{1\,a}}Q_C^{2\,b} + i\overline{Q_C^{2\,a}}Q^{1\,b})\Omega_{bc}P_{L,R}\Psi^{k\,ca}. \qquad (21)$$

Analogously, the $U(1)_A$ partners of the chimera baryons are the following:

$$\mathcal{O}_{\mathrm{CB},1}^{\prime L,R} = i(\overline{Q^{1\,a}}Q^{2\,b} + \overline{Q^{2\,a}}Q^{1\,b})\Omega_{bc}P_{L,R}\Psi^{k\,ca},$$

$$\mathcal{O}_{\mathrm{CB},2}^{\prime L,R} = (\overline{Q^{1\,a}}Q^{2\,b} - \overline{Q^{2\,a}}Q^{1\,b})\Omega_{bc}P_{L,R}\Psi^{k\,ca},$$

$$\mathcal{O}_{\mathrm{CB},3}^{\prime L,R} = i(\overline{Q^{1\,a}}Q^{1\,b} - \overline{Q^{2\,a}}Q^{2\,b})\Omega_{bc}P_{L,R}\Psi^{k\,ca},$$

$$\mathcal{O}_{\mathrm{CB},4}^{\prime L,R} = (\overline{Q^{1\,a}}\gamma^5 Q_C^{2\,b} + \overline{Q_C^{2\,a}}\gamma^5 Q^{1\,b})\Omega_{bc}P_{L,R}\Psi^{k\,ca},$$

$$\mathcal{O}_{\mathrm{CB},5}^{\prime L,R} = i(\overline{Q^{1\,a}}\gamma^5 Q_C^{2\,b} - \overline{Q_C^{2\,a}}\gamma^5 Q^{1\,b})\Omega_{bc}P_{L,R}\Psi^{k\,ca}. \qquad (22)$$

The $\mathcal{O}_{\mathrm{CB}}^{\prime L,R}$ operators are expected to source heavier particles, in respect to the $\mathcal{O}_{\mathrm{CB}}^{L,R}$.

## III. THE LATTICE THEORY

In this section, we describe in detail the lattice gauge theory of interest, and the implementation of the numerical algorithms we adopt. Our software is based upon the HiRep code, originally developed in the BSM context and presented in Ref. [137]. In earlier studies of $Sp(2N)$ lattice gauge theories [86,91], we both generalized the Cabibbo-Marinari prescription [138], and implemented an efficient resymplecticization projection. For the purpose of this study, we further wrote original code to implement dynamical calculations in the presence of matter in multiple representations. It is worth reminding the reader that most lattice code publicly available has been optimized for QCD and QCD-like theories, and only a handful of codes allowing to treat multiple representations exist (see for instance [69,70,73], for $SU(4)$ gauge theories). Hence, we describe our algorithm in some detail, and we provide a

number of tests, both in this as well as in the subsequent sections, to demonstrate that our implementation reproduces the expected results, in the appropriate limits.

### A. Lattice action

We write the Euclidean action, discretized in four dimensions, of non-Abelian $Sp(2N)$ gauge theories coupled to fermionic matter as the sum of the gauge $S_g$ and fermion $S_f$ actions,

$$S = S_g + S_f. \qquad (23)$$

The generic lattice site is denoted by $x$, while $\hat{\mu}, \hat{\nu}$ are unit displacements in the space-time directions $\mu$, $\nu$, so that the first term of Eq. (23), the Wilson plaquette action, is

$$S_g \equiv \beta \sum_x \sum_{\mu < \nu} \left( 1 - \frac{1}{2N}\mathrm{ReTr}U_\mu(x)U_\nu(x+\hat{\mu}) \right.$$
$$\left. \times U_\mu^\dagger(x+\hat{\nu})U_\nu^\dagger(x) \right), \qquad (24)$$

where $U_\mu(x) \in Sp(2N)$ is the group variable living on the link $(x, \mu)$, and $\beta \equiv \frac{4N}{g_0^2}$, with $g_0$ the gauge coupling.

The second term of Eq. (23) is the massive Wilson-Dirac action:

$$S_f \equiv a^4 \sum_{j=1}^{N_f} \sum_x \bar{Q}^j(x) D_m^{(f)} Q^j(x)$$
$$+ a^4 \sum_{j=1}^{n_f} \sum_x \bar{\Psi}^j(x) D_m^{(as)} \Psi^j(x), \qquad (25)$$

where $a$ is the lattice spacing, $Q^j$ and $\Psi^j$ the fermions (flavor indices are explicitly shown, while color and spinor indices are understood), and the Dirac operators $D_m^{(f)}$ for the fundamental and $D_m^{(as)}$ for the 2-index antisymmetric representation will be defined shortly. Here and in the following, we restrict the number of colors to $N_c = 4$ (or $N = 2$), and the number of Dirac flavors to $N_f = 2$ and $n_f = 3$ for the fundamental and antisymmetric representations, respectively. Nevertheless, where possible we leave explicit the dependence on arbitrary $N \geq 2$, as our construction can be applied to all $Sp(2N)$ gauge theories.

For the $(f)$ fermions, the link variable appearing in the Dirac operator coincides with $U_\mu(x)$ in Eq. (24):

$$U_\mu^{(f)}(x) = U_\mu(x) \in Sp(2N). \qquad (26)$$

In the case of the $(as)$ fermions, we construct link variable $U_\mu^{(as)}(x)$, and thus the Dirac operator $D_m^{(as)}$, by following the prescription in Ref. [137]. We first define an

orthonormal basis $e_{(as)}^{(ab)}$ [the multi-index $(ab)$ runs over ordered pairs with $1 \le a < b \le 2N$] for the appropriate vector space of $2N \times 2N$ antisymmetric (and $\Omega$-traceless) matrices. There are $N(2N-1)-1$ such matrices. For $b = N+a$ and $2 \le a \le N$, they have the following nonvanishing entries:

$$(e_{(as)}^{(ab)})_{c,N+c} \equiv -(e_{(as)}^{(ab)})_{N+c,c} \equiv \begin{cases} \frac{1}{\sqrt{2a(a-1)}}, & \text{for } c < a, \\ \frac{-(a-1)}{\sqrt{2a(a-1)}}, & \text{for } c = a, \end{cases} \quad (27)$$

and for $b \ne N+a$

$$(e_{(as)}^{(ab)})_{cd} \equiv \frac{1}{\sqrt{2}}(\delta_{ad}\delta_{bc} - \delta_{ac}\delta_{bd}). \quad (28)$$

The $\Omega$-traceless condition can be rewritten explicitly as $\Omega^{dc}(e_{(as)}^{(ab)})_{cd} = 0$. Specializing to the $Sp(4)$ case, the matrix $e_{(as)}^{(13)}$ vanishes by construction, and one can verify that the remaining five nonvanishing matrices satisfy the orthonormalization condition $\text{Tr} e_{(as)}^{(ab)} e_{(as)}^{(cd)} = -\delta^{(ab)(cd)}$. The ordering of pairs $(ab)$ in our convention is (12), (23), (14), (24), and (34). We show their explicit forms in Appendix A 3. The link variables $U_\mu^{(as)}(x)$ descend from the fundamental link variables $U_\mu(x)$ and take the form of

$$(U_\mu^{(as)})_{(ab)(cd)}(x)$$
$$\equiv \text{Tr}[(e_{(as)}^{(ab)})^\dagger U_\mu(x) e_{(as)}^{(cd)} U_\mu^\text{T}(x)], \text{ with } a < b, c < d. \quad (29)$$

With all of the above, the massive Wilson-Dirac operators are defined by

$$D_m^{(f)} Q_j(x) \equiv (4/a + m_0^f) Q_j(x)$$
$$- \frac{1}{2a} \sum_\mu \{(1-\gamma_\mu) U_\mu^{(f)}(x) Q_j(x+\hat\mu)$$
$$+ (1+\gamma_\mu) U_\mu^{(f),\dagger}(x-\hat\mu) Q_j(x-\hat\mu)\}$$

for the fundamental representation, and

$$D_m^{(as)} \Psi_k(x) \equiv (4/a + m_0^{as}) \Psi_k(x)$$
$$- \frac{1}{2a} \sum_\mu \{(1-\gamma_\mu) U_\mu^{(as)}(x) \Psi_k(x+\hat\mu)$$
$$+ (1+\gamma_\mu) U_\mu^{(as),\dagger}(x-\hat\mu) \Psi_k(x-\hat\mu)\}, \quad (30)$$

for the 2-index antisymmetric representation. $m_0^f$ and $m_0^{as}$ are the (degenerate) bare masses of $Q$ and $\Psi$, respectively.

## B. Numerical implementation

We have extended the HiRep code [137][3] to adapt it to treat $Sp(2N)$ [rather than $SU(N_c)$] gauge theories and couple them to fermions in multiple representations of the group. Ensembles with dynamical fermions can be produced by combining the hybrid Monte Carlo (HMC) algorithm, and its extension with rational approximations for the Dirac matrix with fractional powers—the rational hybrid Monte Carlo (RHMC). The standard (R)HMC algorithm consists of the following three main steps.

(i) Generation of new pseudofermion fields from a heat-bath distribution.
(ii) Molecular dynamics (MD) evolution—dynamical evolution of the gauge field configuration with a fictitious Hamiltonian.
(iii) Metropolis test at the end of each MD trajectory to correct for errors in the numerical integration of the equations of motion.

Let us provide some more technical details about these three steps.

As anticipated, the implementation of HMC/RHMC algorithms for fermions in arbitrary representations of $SU(N_c)$ gauge groups is extensively discussed in Ref. [137], and its generalization to the fundamental representation of $Sp(2N)$ in Ref. [89]. We pause here to discuss in further depth the case of multiple representations, given the limited extent of the literature on the subject [69,70,73]. In the rest of this subsection, we follow closely the discussion in Ref. [137], and refer the reader to this publication for details, while we highlight the differences required in our implementation.

The fermion action in Eq. (25) is quadratic in the fermion fields. It can be explicitly integrated when we compute the partition function of the theory, a process that results in the fermion determinant $\det(D_m)$. If we suppress spin and color indices, for convenience, and consider a generic number of flavors $n$, we can replace this determinant by introducing complex bosonic fields $\phi$ and $\phi^\dagger$, called pseudofermions, with the generic definition:

$$(\det(D_m))^n \equiv (\det(Q_m))^n$$
$$= \int \mathcal{D}\phi \mathcal{D}\phi^\dagger e^{-a^4 \sum_x \phi^\dagger(x)(Q_m^2)^{-n/2}\phi(x)}. \quad (31)$$

The Dirac operator $Q_m \equiv \gamma_5 D_m$ is Hermitian. The square of $Q_m$ is positive definite. In the rest of this section, we set the lattice spacing $a = 1$, for notational convenience.

As explained in Ref. [137], one defines the MD evolution in fictitious time $\tau$ to be governed by a Hamiltonian which receives contributions $H_g$ from gauge fields, and $H_f^R$ from

---

[3]The code is publicly available, and can be accessed at https://github.com/claudiopica/HiRep for the main $SU(N_c)$ version, and at https://github.com/sa2c/HiRep for the $Sp(2N)$ fork.

each species of fermions in representation $R$ of the group—see Eqs. (15)–(18) in Ref. [137]. If we want to describe $n^R$ degenerate (Dirac) fermions in a given representation $R$, we need to be more precise in the definition of the pseudo-fermions and how they enter the exponent in Eq. (31), and the Hamiltonian $H_f^R$. We introduce $N_{\rm pf}$ pseudofermions $\phi_k^R$ and $\phi_k^{R\dagger}$, and their Hamiltonian is determined by the Dirac operator in the representation $R$:

$$H_f^R = \sum_{k=1}^{N_{\rm pf}} \sum_x \phi_k^{R,\dagger}(x)((Q_m^R)^2)^{-l_k} \phi_k^R(x), \qquad (32)$$

subject to the constraint $\sum_{k=1}^{N_{\rm pf}} l_k = n^R/2$. If the number $n^R$ of species of type $R$ is even, then we can set $l_k = 1$ for all $k$ and $N_{\rm pf} = n^R/2$, because the inverse of $(Q_m^R)^2$ can be computed, $Q_m$ being Hermitian.

In the case of odd $n^R$, on the other hand, it is possible to set $N_{\rm pf} = n$, and $l_k = 1/2$, by applying the rational approximation [139] to $H_f^R$—see Sec. III B of Ref. [137], also for the definition of the numerical coefficients appearing in the RHMC approximation.

In the calculation we perform for this paper, we use an admixture of the above. For the $N_f = 2 = n^{(f)}$ Dirac fermions in the fundamental representation, we set $N_{\rm pf} = 1$, and adopt the HMC evolution. As for the $n_f = 3 = n^{(as)}$ Dirac fermions in the antisymmetric representation, we further split them into $n^{(as)} - 1 = 2$, which requires $N_{\rm pf} = 1$ pseudofermions in the HMC evolution, and a third degenerate $(as)$ fermion, which we describe by one additional pseudofermion, for which the evolution is ruled by the RHMC algorithm—$l_1 = 1/2$ in its Hamiltonian in Eq. (32).[4]

We hence have four contributions to the MD evolution: the gauge contribution is supplemented by those coming from the HMC treatment of the $(f)$ pseudofermion, from the HMC treatment of one $(as)$ pseudofermion, and from the RHMC application to the third, $(as)$ pseudofermion. We illustrate the size of each, by showing in Fig. 1 their contribution to the force as it enters the Hamiltonian evolution—see the Hamilton equations governing the MD evolution, in Eqs. (19) and (20) of Ref. [137]—averaged over one of the ensembles. The acceptance rate is in the range of 75%–85%. To accelerate the (computationally demanding) inversion of the Dirac operator $Q_m^2$, we use the second-order Omelyan integrator [140] in the MD evolution and the even-odd preconditioning of the fermion matrix [141], applied to the (R)HMC algorithm as discussed in Ref. [137].

---

[4]We made this choice so that the rational approximation is applied only to one of the pseudofermions. We checked numerically that, for the range of masses relevant to this paper, had we treated all three $(as)$ fermions with the RHMC algorithm, with $l_k = 1/2$ for $k = 1, 2, 3$, we would have obtained consistent results.
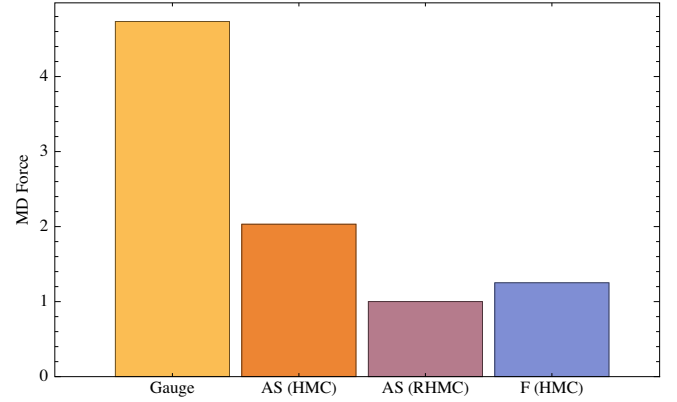


FIG. 1. The relative contribution of gauge and fermion fields to the molecular dynamics force, averaged over the ensemble with $\beta = 6.5$, $am_0^f = -0.7$, and $am_0^{as} = -0.9$, on lattice of size $8^4$, chosen for illustration purposes. The fermion force receives three separate contributions, one for each of the pseudofermion fields: one HMC pseudofermion for two fundamental flavors, denoted F (HMC), and one each for the antisymmetric AS (HMC) and AS (RHMC) pseudofermions making up the three antisymmetric flavors. The forces are normalized to the one due to the antisymmetric fermion with the RHMC implementation.

## C. Symmetry properties of the Dirac operator

The Wilson-Dirac formulation for mass-degenerate Dirac fermions in Eq. (25) explicitly breaks the global $SU(4) \times SU(6)$ symmetry to its $Sp(4) \times SO(6)$ subgroup, as in the continuum theory discussed in Sec. II. This is accompanied by the formation of a nonzero fermion condensate, which in the massless limit would result in the spontaneous breaking of the symmetry. This is reflected in the spectrum of the Dirac operator [142]: universal features in this spectrum can be modeled by chiral random matrix theory (chRMT) [143]—see Ref. [144] for a comprehensive review. In this subsection, following the discussion in Ref. [73], we summarize the chRMT analytical predictions. In subsequent sections we will present our numerical results, obtained by computing explicitly the spectrum of Dirac eigenvalues, and compare them to chRMT predictions, hence providing a nontrivial test of the accuracy of the numerical algorithms.

An antiunitary transformation is an antilinear map between two complex Hilbert spaces $\mathcal{H}_1$ and $\mathcal{H}_2$

$$\mathcal{A}: \mathcal{H}_1 \to \mathcal{H}_2, \qquad (33)$$

with $\mathcal{A}(ax + by) = a^* \mathcal{A}(x) + b^* \mathcal{A}(y)$ such that

$$\langle \mathcal{A}(x), \mathcal{A}(y) \rangle = \langle x, y \rangle^*, \qquad (34)$$

where $\langle \cdot, \cdot \rangle$ denotes the inner products in the two spaces. $x, y$ are elements of $\mathcal{H}_1$, while $a, b$ are complex numbers. If $\mathcal{H}_1 = \mathcal{H}_2$ or, equivalently, the map is invertible, we call $\mathcal{A}$

an antiunitary operator. Any antiunitary operator can be written as

$$\mathcal{A} = \mathcal{V}K, \tag{35}$$

where $\mathcal{V}$ is a unitary operator and $K$ is the complex-conjugation operator.

Let us now consider the discretized Dirac operator $D_m^R$—generalizing Eq. (30) to arbitrary representations $R$. If we find an antiunitary operator $\mathcal{A}^R$ that obeys the relation

$$[\mathcal{A}^R, \gamma^5 D_m^R] = 0, \tag{36}$$

then we can use this property to characterize the degeneracies in the spectrum of the Dirac operator. There are actually three possibilities [144], precisely related to the Dyson index as follows:

(i) $(\mathcal{A}^R)^2 = \mathbb{1}$, in which case the Dyson index is $\bar{\beta} = 1$, and there exists a basis in which the Dirac operator is real,

(ii) there exists no such $\mathcal{A}^R$, in which case the Dyson index is $\bar{\beta} = 2$, and the Dirac operator is complex,

(iii) $(\mathcal{A}^R)^2 = -\mathbb{1}$, in which case the Dyson index is $\bar{\beta} = 4$, and there exists a basis in which the Dirac operator is real quaternionic (pseudoreal).

In the context of chRMT, this classification parallels that of the ensembles, itself reflected in the chiral symmetry-breaking pattern for the $N_f$ Dirac fermions of the theory, as follows.

(i) $\bar{\beta} = 1$: the chRMT ensemble is called chiral Gaussian orthogonal ensemble (chGOE), because of the real matrix elements, and the breaking pattern is $SU(2N_f) \rightarrow Sp(2N_f)$.

(ii) $\bar{\beta} = 2$: the chRMT ensemble is called chiral Gaussian unitary ensemble (chGUE), because of the complex elements, and the breaking pattern is $SU(N_f) \times SU(N_f) \rightarrow SU(N_f)$.

(iii) $\bar{\beta} = 4$: the chRMT ensemble is called chiral Gaussian symplectic ensemble (chGSE), because of the quaternionic elements, and the breaking pattern is $SU(2N_f) \rightarrow SO(2N_f)$.

Let us first consider the case of fermions in the fundamental representation of $Sp(4)$. As implied by Eqs. (35) and (36), and using the facts that $\Omega^{-1} T_{(f)}^A \Omega = -T_{(f)}^{A\,T} = -T_{(f)}^{A*}$, that $C$ commutes with $\gamma_5$ and that $C^2 = -\mathbb{1} = -\gamma_5^2$, we see that

$$\mathcal{A}^{(f)} = \Omega C \gamma^5 K \tag{37}$$

commutes with $\gamma_5 D_m^{(f)}$, and that $(\mathcal{A}^{(f)})^2 = \mathbb{1}$ and thus belongs to the class of $\bar{\beta} = 1$. Indeed, the $SU(4)$ global symmetry acting on the $(f)$ fermions breaks to its $Sp(4)$ subgroup.

In the case of fermions in the antisymmetric representation of $Sp(4)$, the construction of the antiunitary operator requires first to generalize the generators to this representation. We first recall that the color indices of the link variables $(U_\mu^{(as)})_{(ab)(cd)}(x)$ in Eq. (29) are denoted by the multi-indices (12), (23), (14), (24), and (34). Using this ordering convention, we find the following $5 \times 5$ matrix:

$$W = \begin{pmatrix} 0 & 0 & 0 & 0 & 1 \\ 0 & 0 & 1 & 0 & 0 \\ 0 & 1 & 0 & 0 & 0 \\ 0 & 0 & 0 & 1 & 0 \\ 1 & 0 & 0 & 0 & 0 \end{pmatrix}, \tag{38}$$

which is real, symmetric, and unitary, and satisfies

$$W^{-1} T_{(as)}^A W = -T_{(as)}^{A*}, \tag{39}$$

where a basis of $T_{(as)}$ is shown explicitly in Appendix A 3. In analogy with Eq. (37), we find the antiunitary operator

$$\mathcal{A}^{(as)} = WC\gamma^5 K \tag{40}$$

to commute with $\gamma_5 D_m^{(as)}$. The square of $W$ is the identity matrix, hence we conclude that $(\mathcal{A}^{(as)})^2 = -\mathbb{1}$, and $\bar{\beta} = 4$. The $SU(6)$ symmetry acting on the $(as)$ fermions is broken to its $SO(6)$ subgroup.

A noticeable consequence of the fact that $(\mathcal{A}^{(as)})^2 = -\mathbb{1}$ is that the determinant of $D_m^{(as)}$ is real and positive (see, e.g., [145]). Therefore, numerical simulations of Sp(4) gauge theories involving an odd number of antisymmetric Dirac flavors are not plagued by the sign problem. This enables us to have controlled numerical results for our systems using standard Monte Carlo methods.

One of the interesting predictions of chRMT is that the distribution of the unfolded density of spacings $s$ between subsequent eigenvalues of $\gamma_5 D_m^R$ assumes the following functional dependence (the Wigner surmise):

$$P(s) = N_{\bar{\beta}} s^{\bar{\beta}} e^{-c_{\bar{\beta}} s^2}, \quad \text{with} \quad N_{\bar{\beta}} = 2 \frac{\Gamma^{\bar{\beta}+1}(\frac{\bar{\beta}}{2}+1)}{\Gamma^{\bar{\beta}+2}(\frac{\bar{\beta}+1}{2})},$$

$$c_{\bar{\beta}} = \frac{\Gamma^2(\frac{\bar{\beta}}{2}+1)}{\Gamma^2(\frac{\bar{\beta}+1}{2})}, \tag{41}$$

where $\Gamma$ is the Euler gamma function. This prediction can be tested numerically, as we shall see later in the paper (see also Ref. [73]).

## IV. LATTICE OBSERVABLES

This section is devoted to defining and discussing the lattice observables of interest in the numerical study. We start from the spectrum of the Dirac operator, which as explained in Sec. III C is closely related to the breaking of the global symmetry. We then provide details about the lattice implementation of meson and (chimera) baryon operators, and refresh for the reader some standard material about the extraction of masses and (renormalized) decay constants from the appropriate 2-point functions.

Before proceeding, we pause to make two comments of a technical nature. In what follows, we express the masses and decay constants of composite states in units of the lattice spacing $a$. The reader might, with some reason, think that it would be best practice to introduce a nonperturbative scale-setting procedure that allows one to take the continuum $a \to 0$ limit without ambiguities. And indeed, in previous publications our collaboration elected to adopt to this purpose the Wilson flow [146,147]. Yet, as in this work we do not attempt the continuum limit extrapolation, but rather only extract lattice measurements in a small number of ensembles, this is not necessary. Furthermore, in this theory the fermions have non-negligible dynamical effects—see for example Fig. 1—and hence the Wilson flow observables are expected to be quite sensitive to the choice of fermion mass, making a future, dedicated study necessary. We plan to do so when we will have enough numerical ensembles to perform the continuum and chiral limit extrapolations.

The second comment is even more dreary. Throughout this work we use $Z_2 \times Z_2$ single time slice stochastic sources [149] in the studies of 2-point correlation functions for mesons, while we use simple point sources for the chimera baryon. However, it is a well-known fact among lattice practitioners that extracting the masses of heavy composite states, particularly in the case of fermionic operators such as the chimera baryon, is complicated by heavy state contamination and numerical noise [148]. And it is a known fact that such shortfalls can be addressed by combining (Wuppertal) smeared source and sink operators [150], by (APE) smearing of the gauge links [151] and by adopting variational methods in treating the eigenvalue problems [152,153]. Again, applying these techniques to our current ensembles would bring us unnecessarily beyond the scopes of this paper. And yet, as anticipated in Ref. [120], at the time of editing this manuscript we have developed most of the necessary processes for our model, and some of us have been extensively testing them on a simpler theory: the partially quenched model in which only the $(as)$ fermions are included in the MD evolution, while the $(f)$ fermions are treated as external probes. We will report on this process elsewhere [154], and apply such techniques to the multirepresentation theory of interest in future precision studies.

TABLE II. The numerical error in the calculation of $\text{Tr}Q_m^2$ on a lattice of dimensions $4^4$, for the values of lattice parameters indicated, and for five different combinations of quenched theory and fermion representation.

| Gauge group | Representation | $\beta$ | $am_0$ | $\text{Tr}Q_m^2$ from Eq. (43) | $\Delta\text{Tr}Q_m^2$ |
|---|---|---|---|---|---|
| $SU(2)$ | $(f)$ | 1.8 | $-1.0$ | 26624 | $8.7 \times 10^{-11}$ |
| $SU(4)$ | $(f)$ | 10.0 | $-0.2$ | 75530.24 | $5.8 \times 10^{-10}$ |
| $SU(4)$ | $(as)$ | 10.0 | $-0.2$ | 113295.36 | $1.5 \times 10^{-9}$ |
| $Sp(4)$ | $(f)$ | 8.0 | $-0.2$ | 75530.24 | $1.9 \times 10^{-9}$ |
| $Sp(4)$ | $(as)$ | 8.0 | $-0.2$ | 94412.8 | $3.5 \times 10^{-9}$ |

### A. Eigenvalues of the lattice Dirac operator

For the tests described in this subsection, we use ensembles obtained in the quenched approximation. We denote as $\lambda$ each eigenvalue of the Hermitian Dirac operator $Q_m$, defined after Eq. (31). We compute such eigenvalues via matrix diagonalization, using the Jacobi algorithm, which is accurate enough to yield all the eigenvalues of the Dirac matrix with dimension up to $\sim 5000$.[5] We then sum the eigenvalues of $Q_m^2$, and find

$$\text{Tr}Q_m^2 \equiv \sum_{\lambda=\lambda_{\min}}^{\lambda_{\max}} \lambda^2, \tag{42}$$

which we can compare to the analytical expression

$$\text{Tr}Q_m^2 = 4 \times d_R \times N_T \times N_S^3 \times (4 + (a\,m_0 + 4)^2), \tag{43}$$

where the trace is over color and spinor indices, while $d_R$ is the dimension of the representation $R$, and $N_T$ and $N_S$ are the extents of the lattice in the temporal and spactial directions, respectively. As a first test of the numerical processes, we calculate the difference between Eqs. (42) and (43), denoted as $\Delta\text{Tr}Q_m^2$, in Table II. In the table we report the result of our exercise, for several gauge groups and matter representations. As can be seen $\Delta\text{Tr}Q_m^2/\text{Tr}Q_m^2 \sim O(10^{-14})$ for all the cases we considered.

In order to make a comparison with the chRMT prediction in Eq. (41), we need to implement an unfolding procedure which consists of rescaling of the spacing between adjacent eigenvalues by the local spectral density. Because the functional form of the density is not known *a priori*, in practice we replace it by the density over many lattice configurations. To do so, following the prescription of Ref. [73], we first compute the eigenvalues of $Q_m$ for a set of $N_{\text{conf}}$ different configurations. Each such calculation,

---

[5]If we restrict ourselves to the computation of the low-lying eigenvalues, we can use several techniques for acceleration, such as the subspace iteration with Chebyshev acceleration and eigenvalue locking (e.g., see the appendix of Ref. [155]), as implemented in the HiRep code.

for $c = 1, ..., N_{\text{conf}}$, yields eigenvalues $\lambda_i^{(c)}$, which we list in increasing order, discarding degeneracies. We then combine all the eigenvalues thus computed in one, increasingly ordered long list. And for each $c = 1, ..., N_{\text{conf}}$ we produce a new list, in which instead of $\lambda_i^{(c)}$ we include $n_i^{(c)}$, defined as the positive integer position of the eigenvalue $\lambda_i^{(c)}$ in the long list. The density of spacing, $s$, is then replaced by the sequence of $s_i^{(c)}$ given by

$$s_i^{(c)} \equiv \frac{n_{i+1}^{(c)} - n_i^{(c)}}{\mathcal{N}}. \tag{44}$$

The constant $\mathcal{N}$ is defined in such a way that $\langle s \rangle = 1$, after averaging $s_i^{(c)}$ over the whole ensemble. We then define the unfolded density of spacings $P(s)$ as the limiting case of the normalized (and discretized) distribution function obtained by binning our numerical results for $s_i^{(c)}$. We will return in Sec. V to the explicit comparison of the numerical results with the analytical predictions of chRMT.

### B. Of mesons on the lattice

We have already discussed how the interpolating operators sourcing mesons are defined in the (Minkowski) continuum theory, in particular for pseudoscalars, in Sec. II C. We come now to the (Euclidean) lattice formulation. Gauge-invariant operators associated with mesonic states are generically denoted by

$$\mathcal{O}_M^R(x) = \bar{\chi}(x)\Gamma_M\chi'(x), \tag{45}$$

where $\chi, \chi' = Q$ or $\chi, \chi' = \Psi$, for fermions in representation $R = (f)$ or $R = (as)$, respectively. We suppress here color, flavor, and spinor indexes, for notational simplicity, but we will make them manifest when useful. Adopting Euclidean signature, and specializing to rest-frame (zero-momentum) observables, the Dirac structures of interest are[6]

$$\Gamma_M = \gamma^5, \mathbb{1}, \gamma^\mu, \gamma^5\gamma^\mu, \gamma^0\gamma^\mu, \gamma^5\gamma^0\gamma^\mu \tag{46}$$

which we label by PS, S, V, AV, T, and AT, corresponding to the pseudoscalar, scalar, vector, axial-vector, tensor, and axial-tensor mesons.[7] We restrict our attention to flavored meson states with $\chi \neq \chi'$, so that contributions from disconnected diagrams to 2-point functions are absent.

---

[6]As on the lattice one measures correlation functions for zero momentum, it is convenient to use $\gamma^0\gamma^\mu$ and $\gamma^5\gamma^0\gamma^\mu$, instead of $\sigma^{\mu\nu}$ and $\gamma^5\sigma^{\mu\nu}$, respectively.

[7]In the continuum limit, after chiral symmetry breaking, correlation functions involving tensor operator $T$ and vector operator $V$ mix. Also, we anticipate here that will face numerical difficulties in extracting masses for the axial-tensor states—for comparison, these states are called $b_1$ in two-flavor QCD.

As explicitly shown in Eq. (18), mesons and diquarks combine together to form irreducible representations of $Sp(4)$. For example, masses and decay constants of the five PNGBs are degenerate (see also Ref. [88]).

The 2-point correlation function for mesons can be written as follows:

$$\begin{aligned} \langle O_M^R(x)O_{M'}^{R\dagger}(y)\rangle &= \langle\bar{\chi}(x)\Gamma_M\chi'(x)\overline{\chi'}(y)\bar{\Gamma}_{M'}\chi(y)\rangle \\ &= -\text{Tr}[\Gamma_M S^{R'}(x,y)\bar{\Gamma}_{M'}S^R(y,x)] \\ &= -\text{Tr}[\gamma^5\Gamma_M S^{R'}(x,y)\bar{\Gamma}_{M'}\gamma^5 S^{R\dagger}(x,y)], \end{aligned} \tag{47}$$

where $\bar{\Gamma} = \gamma^0\Gamma^\dagger\gamma^0$. The fermion propagators are defined by

$$\begin{aligned} S_{Q\,b\,\alpha\beta}^{i\,a}(x,y) &= \langle Q^{i\,a}{}_\alpha(x)\overline{Q^{i\,b}}{}_\beta(y)\rangle \quad \text{and} \\ S_{\Psi\,cd\,\alpha\beta}^{k\,ab}(x,y) &= \langle\Psi^{k\,ab}{}_\alpha(x)\overline{\Psi^{k\,cd}}{}_\beta(y)\rangle, \end{aligned} \tag{48}$$

where $a$, $b$, $c$, $d$ are color indices, $i$, $k$ are flavor indices, and $\alpha$, $\beta$ are spinor indices. We also use the $\gamma^5$-Hermiticity property, $S_R(x,y)^\dagger = \gamma^5 S_R(y,x)\gamma^5$ (see Appendix A 2), in the last line of Eq. (47). With the notation $x \equiv (t,\vec{x})$ and $y \equiv (t_0,\vec{y})$, the zero-momentum correlation function is

$$C_{\mathcal{O}_{MM'}^R}(t-t_0) = \sum_{\vec{x}\vec{y}}\langle O_M^R(x)O_{M'}^{R\dagger}(y)\rangle \tag{49}$$

$$= -\sum_{\vec{x}\vec{y}}\text{Tr}[\gamma^5\Gamma_M S^{R'}(x,y)\bar{\Gamma}_{M'}\gamma^5 S_R^\dagger(x,y)]. \tag{50}$$

At large Euclidean time $t$, the correlation function in Eq. (49) for $M = M'$ has the following asymptotic form:

$$C_{\mathcal{O}_{MM}^R}(t) \to |\langle 0|\mathcal{O}_M^R|M\rangle|^2 \frac{1}{2m_M^R}[e^{-m_M^R t} + e^{-m_M^R(T-t)}], \tag{51}$$

where $T$ is the temporal extent of the lattice and $m_M^R$ is the mass of the ground state meson $|M\rangle$ of type $M$, composed of fermions in representation $R$. The overlap of the interpolating operator $\mathcal{O}_M$ with the $|\text{PS}\rangle$, $|\text{V}\rangle$, and $|\text{AV}\rangle$ states can be parametrized by

$$\langle 0|\mathcal{O}_{\text{AV}}^R|\text{PS}\rangle = \sqrt{2}f_{\text{PS}}^R p^\mu, \quad \langle 0|\mathcal{O}_{\text{V}}^R|\text{V}\rangle = \sqrt{2}f_{\text{V}}^R m_{\text{V}}\epsilon^\mu, \quad \text{and}$$

$$\langle 0|\mathcal{O}_{\text{AV}}^R|\text{AV}\rangle = \sqrt{2}f_{\text{AV}}^R m_{\text{AV}}\epsilon^\mu, \tag{52}$$

where $f_M^R$ are the decay constants of the corresponding three (ground-state) mesons.[8] The polarization four-vector $\epsilon^\mu$ obeys the two defining relations $p_\mu\epsilon^\mu = 0$ and $\epsilon_\mu^*\epsilon^\mu = 1$. To extract the pseudoscalar decay constant, besides

---

[8]The normalizations of the matrix elements are consistent with those that for 2-flavor QCD yield the pion decay constant $f_\pi \simeq 93$ MeV.

$C_{\mathcal{O}^R_{\mathrm{PSPS}}}(t)$, we need to extract the additional correlation function with $M = \mathrm{AV}$ and $M' = \mathrm{PS}$:

$$C_{\mathcal{O}^R_{\mathrm{AVPS}}}(t) \rightarrow \frac{1}{\sqrt{2}} f^R_{\mathrm{PS}} \langle 0 | \mathcal{O}^R_{\mathrm{PS}} | \mathrm{PS} \rangle^* [e^{-m^R_{\mathrm{PS}} t} - e^{-m^R_{\mathrm{PS}}(T-t)}]. \quad (53)$$

The decay constants receive multiplicative renormalization. We computed the renormalization factors in lattice perturbation theory for Wilson fermions at the one-loop level, with tadpole improvement, following the prescriptions dictated by Refs. [156,157]. The tadpole-improved gauge coupling is defined as $\tilde{g}^2 = g^2/\langle P \rangle$, with $\langle P \rangle$ the average plaquette. With the definitions

$$f^{Rren}_{\mathrm{PS}} \equiv Z_A f^R_{\mathrm{PS}}, \quad f^{Rren}_{\mathrm{V}} \equiv Z_{\mathrm{V}} f^R_{\mathrm{V}}, \quad f^{Rren}_{\mathrm{AV}} \equiv Z_A f^R_{\mathrm{AV}}, \quad (54)$$

and

$$Z_{A,V} = 1 + C^R (\Delta_{\Sigma_1} + \Delta_{\Gamma}) \frac{\tilde{g}^2}{16\pi^2}, \quad (55)$$

one finds the numerical coefficients required by replacing $C^{(f)} = 5/4$, $C^{(as)} = 2$, $\Delta_{\Sigma_1} = -12.82$, $\Delta_{\mathrm{V}} = -7.75$, and $\Delta_{\mathrm{AV}} = -3.0$ [89].

### C. Of chimera baryons on the lattice

As discussed in Sec. II, chimera baryons are composed of two fermions in the fundamental ($f$) and one in the antisymmetric ($as$) representations of $Sp(4)$. The operators which interpolate the would-be top partners [and their $U(1)_A$ counterparts] in a phenomenologically realistic model are displayed in Eqs. (21) and (22)—for the purposes of this paper, we can ignore the chiral projection with $P_{L,R}$ in Eqs. (21) and (22). The operators in Eq. (21) are similar to the nonflavor singlet spin-1/2 $\Lambda$ baryon operators considered in lattice QCD calculations. In general the interpolating operators of the chimera baryon are

$$\mathcal{O}^\alpha_{\mathrm{CB(CC)}}(x) = D^{\alpha\beta\gamma\delta} \Omega_{ac} \Omega_{bd} Q^{ia}_{(C)\beta}(x) Q^{jb}_{(C)\gamma}(x) \Psi^{kcd}_\delta(x), \quad (56)$$

where $a$, $b$, $c$, $d$ are color indices, $i$, $j$, $k$ are flavor indices, and $\alpha$, $\beta$, $\gamma$, $\delta$ are spinor indices.[9] The tensor (in spinor space) $D^{\alpha\beta\gamma\delta}$ can be written as a combination of gamma matrices, which projects onto the desired spin state.

We restrict our attention to spin-0 combinations of the two ($f$) fermions, introduce the notation $(\Gamma^1, \Gamma^2) \equiv (C\gamma^5, \mathbb{1})$,

and restrict $D^{\alpha\beta\gamma\delta}$ in Eq. (56) to be made of combinations of $\Gamma^1$ and $\Gamma^2$.[10] For instance, the linear combination $\frac{1}{2}(i\mathcal{O}_{\mathrm{CB},4} - \mathcal{O}_{\mathrm{CB},5})$ can be written as follows:

$$\overline{Q^{2a}_C} Q^{1b} \Omega_{bc} \Psi^{kca} = -\Omega_{da} \Omega_{bc} (Q^{2dT} \Gamma^1 Q^{1b}) \Gamma^2 \Psi^{kca}, \quad (57)$$

where the Dirac adjoint of $Q$ and its charge conjugate $Q_C$ are given by

$$\overline{Q^a} = (Q^a)^\dagger \gamma^0 = -Q^{bT}_C \Omega_{ba}(C\gamma^5), \quad (58)$$

$$\overline{Q^a_C} = -(Q^a_C)^\dagger \gamma^0 = -Q^{bT} \Omega_{ba}(C\gamma^5). \quad (59)$$

In our numerical studies for the spin-1/2 chimera baryon, we find it convenient to use the operator in Eq. (57), rewritten as follows:

$$\mathcal{O}^{k\gamma}_{\mathrm{CB}}(x) = (\Gamma^1)^{\alpha\beta}(\Gamma^2)^{\gamma\delta} \Omega_{da} \Omega_{bc} Q^{2\,a}{}_\alpha(x) Q^{1\,b}{}_\beta(x) \Psi^{kcd}{}_\delta(x). \quad (60)$$

Its Dirac conjugate operator is

$$\overline{\mathcal{O}^k_{\mathrm{CB}}}{}^\gamma(x) = (\Gamma^1)^{\alpha\beta}(\Gamma^2)^{\delta\gamma} \Omega^{da} \Omega^{bc} \overline{\Psi^{kcd}}{}_\delta(x) \overline{Q^{2a}}{}_\alpha(x) \overline{Q^{1b}}{}_\beta(x). \quad (61)$$

After Wick contractions, the propagator for the chimera baryon with flavor $k$ reads

$$\langle \mathcal{O}^k_{\mathrm{CB}}{}^\gamma(x) \overline{\mathcal{O}^k_{\mathrm{CB}}}{}^{\gamma'}(y) \rangle$$
$$= \Omega_{da} \Omega_{bc} \Omega^{d'a'} \Omega^{b'c'} (\Gamma^1)^{\alpha\beta}(\Gamma^1)^{\alpha'\beta'}(\Gamma^2)^{\gamma\delta}(\Gamma^2)^{\delta'\gamma'}$$
$$\times S^{kcd}_{\Psi c'd'\delta\delta'}(x,y) S^{2a}_{Qa'\alpha\alpha'}(x,y) S^{1b}_{Qb'\beta\beta'}(x,y), \quad (62)$$

with the fermion propagators in Eq. (48).

If we define, for convenience,

$$\tilde{S}^k_\Psi \equiv \Gamma^2 S^k_\Psi \Gamma^{2T}, \quad S^U \equiv \Omega S^2_Q \Omega^T \text{ and } \tilde{S}^D \equiv \Gamma^1 (\Omega^T S^1_Q \Omega) \Gamma^{1T}, \quad (63)$$

with $k$ the flavor index, and color indexes understood (but notice that $S^U$ and $S^D$ have lower first and upper second color index, thanks to the action of $\Omega_{ab}$ on the left and $\Omega^{ab}$ on the right), then the correlation function in Eq. (62), evaluated at positive Euclidean time $t - t_0 > 0$ and zero momentum $\vec{p} = 0$, for $\gamma = \gamma'$, takes the more compact form

---

[9] The subscript $Q_C$ denotes the charge conjugate of the 4-component spinor $Q$: because of the pseudoreal nature of the two ($f$) fermions, the global symmetry acting of them is enhanced from $SU(2)_L \times SU(2)_R \times U(1)_A \times U(1)_B$ to $SU(4) \times U(1)_A$, and hence the irreducible representations of the global symmetry contain what one would naively associate with states with different $U(1)_B$.

[10] Extending the basis to include other gamma structures goes beyond our current purposes. Nevertheless, allowing for redundancies in defining the variational basis might improve the numerical signal in a precision study.

$$C_{CB}^k(t-t_0)$$
$$= \sum_{\vec{x}\vec{y}} \text{Tr}_s \tilde{S}_{\Psi}^{kcd}{}_{c'd'}(x,y) \text{Tr}_s [S^U{}_d{}^{d'}(x,y)(\tilde{S}^D{}_c{}^{c'}(x,y))^{\text{T}}], \quad (64)$$

with $\text{Tr}_s$ the trace over spinor indexes, and the transposition only acts on the spinorial indexes. Because of the anti-symmetric properties of the $\tilde{S}_{\Psi}$ indexes, we can rewrite the color contractions by antisymmetrizing over the color indices of the fundamental propagators $S^U$ and $S^D$, by defining a new object:

$$S_{DQA}{}^B(x,y) \equiv \text{Tr}_c[(e_{AS}^A)^\dagger S^U(x,y)(e_{AS}^B)(S^D(x,y))^{\text{T}}], \quad (65)$$

where $\text{Tr}_c$ is a trace over color, while $A, B = 1, \ldots, 5$ denote the ordered pairs of color indices $(ab)$, with the convention introduced in Sec. III A—see Eqs. (27) and (28). Using $S_{DQ}$ in Eq. (65), we arrive at

$$C_{CB}^k(t-t_0) = \sum_{\vec{x}\vec{y}} \text{Tr}_s S_{\Psi}^{kA}{}_B(x,y) \text{Tr}_s S_{DQA}{}^B(x,y). \quad (66)$$

While we have considered the chimera baryon propagators built out of $\mathcal{O}_{CB,4(5)}$ in the above discussion, in Appendix B we explicitly show that those built out of $\mathcal{O}_{CB,1(2)}$ are identical to $C_{CB}(t-t_0)$ in Eq. (66).

As in the case of mesons, at large Euclidean time the (zero-momentum) 2-point correlation functions involving chimera baryon are dominated by the contributions of the lowest states in the given channel. Without loss of generality, we localize the source at the origin $\vec{y} = \vec{0}$. As $t \to \infty$, the asymptotic behavior of the correlator is a textbook example [158]:

$$C_{CB}(t) \equiv \sum_{\vec{x}} \langle \mathcal{O}_{CB}(x)\bar{\mathcal{O}}_{CB}(0)\rangle$$
$$\to \mathcal{P}_+[c_{CB}^+ e^{-m_{CB}^+ t} + c_{CB}^- e^{-m_{CB}^-(T-t)}]$$
$$- \mathcal{P}_-[c_{CB}^- e^{-m_{CB}^- t} + c_{CB}^+ e^{-m_{CB}^+(T-t)}], \quad (67)$$

where the prefactor $\mathcal{P}_\pm \equiv (1 \pm \gamma^0)/2$ arises from the sum over spin at zero momentum, which is nothing but the parity projector in the nonrelativistic limit. (Note that we impose an antisymmetric boundary condition for fermions in the temporal extent.) The coefficients $c_{CB}^\pm$ denote the overlap of the interpolating operator $\mathcal{O}_{CB}$ with positive and negative parity states. Indeed, in the infinite volume lattice $(T \to \infty)$, the second terms in the brackets in Eq. (67)—the backward propagators—vanish.

In order to extract the masses of both parity even and odd chimera baryon states we isolate those states as yielded by Eq. (67). In the nonrelativistic limit, the operator which interpolates the chimera baryon with definite spin and parity $\frac{1}{2}^\pm$ is defined by

$$\mathcal{O}_{CB}^\pm(x) \equiv \mathcal{P}_\pm \mathcal{O}_{CB}(x), \quad (68)$$

where the interpolating operator $\mathcal{O}_{CB}$ is defined in Eq. (60). Accordingly, we define the 2-point correlation function for $\mathcal{O}_{CB}^\pm$ at zero momentum as

$$C_{CB}^\pm(t) \equiv \sum_{\vec{x}} \langle \mathcal{O}_{CB}^\pm(x)\bar{\mathcal{O}}_{CB}^\pm(0)\rangle,$$
$$= \sum_{\vec{x}} \text{Tr}_s[\Gamma^2 \mathcal{P}_\pm \Gamma^2 S_{\Psi}^{A,B}(x,0)]\text{Tr}_s S_{DQ}^{A,B}(x,0), \quad (69)$$

where $S_{DQ}$ is defined in Eq. (65). At large Euclidean time, the asymptotic behavior of $C_{CB}^\pm$ can be written by

$$C_{CB}^\pm(t) \to c_{CB}^\pm e^{-m_{CB}^\pm t} + c_{CB}^\mp e^{-m_{CB}^\mp(T-t)}. \quad (70)$$

The forward and backward propagators for the parity even state decay with the masses of $m_{CB}^+$ and $m_{CB}^-$, and conversely for the parity odd state.

Without parity projection, and at finite $T$ but for $t$ large enough to see the asymptotic behaviors of $C_{CB}(t)$, the correlation function in Eq. (67) is eventually dominated by the lightest state, and the forward and backward contributions have the same coefficients up to opposite sign. As will be discussed in the next section, it turns out that the lightest state is parity-even. After taking the trace over the spin, hence, we find $C_{CB}(t)$ at large Euclidean time as

$$C_{CB}(t) \to c_{CB}^+(e^{-m_{CB}^+ t} - e^{-m_{CB}^+(T-t)}). \quad (71)$$

## V. NUMERICAL RESULTS

In this section we present our main numerical results for the $Sp(4)$ theory of interest. We study the phase space of the lattice theory, the spectrum of the Dirac operator (quenched), the spectrum of mesons, and some important features of the chimera baryon correlation functions. We also assess the size of finite-volume effects. Our results are available in machine-readable form in Ref. [159]. The software workflow used to analyze the data and prepare the plots and tables are made available in Ref. [160].

### A. Phase structure of the lattice theory

In the limit of infinite volume, the lattice action in Eq. (23) has three tunable parameters: the lattice coupling $\beta$ and the two bare masses $am_0^f$ and $am_0^{as}$ of the $(f)$ and $(as)$ (Wilson-Dirac) fermions, respectively. The continuum theory is expected to be recovered at the quantum critical point of the lattice theory, which is connected to the (appropriately defined) limit of large $\beta$ and small lattice spacing. In practical numerical studies, we work with finite lattice parameters, and therefore it is important to choose the lattice parameters in a way that can be smoothly connected and extrapolated to the desired continuum

theory. To do so, in this subsection we explore the parameter space of the lattice theory, identify the phase boundary between its strong- and weak-coupling regimes, and investigate the properties of the phase transitions.

Firstly, we recall that the bulk phase structures of $Sp(4)$ with and without (Wilson) fermions, either in the fundamental or the antisymmetric representations, have already been studied numerically on the lattice. In the Yang-Mills case, the study of the standard plaquette action shows that there is no bulk phase transition [92]. In the presence of fermionic matter, first-order bulk phase transitions have been found, for both choices of ($f$) and ($as$) (Wilson-Dirac) fermions [86,87]. Interestingly, by comparing the results for the theory with $N_f = 2$ fundamental fermions, against the theory with $n_f = 3$ antisymmetric fermions, one finds that the weak-coupling regime extends to different values of $\beta$, reaching to smaller values in the case of ($as$) fermions —the critical values of $\beta$, demarcating strong and weak coupling regimes, are $\beta_{\mathrm{cr}}^f \sim 6.7$ [86] and $\beta_{\mathrm{cr}}^{as} \sim 6.5$ [87].

Starting from these observations, we sketch in Fig. 2 the putative bulk phase diagram of the $Sp(4)$ gauge theory coupled to mixed representation fermions. The black-dotted surface represents a surface with boundary of first-order bulk phase transitions. For illustrative purposes, we also display three colored lines indicating the first-order phase transitions for fixed choices of $\beta = 6.2$ (red), 6.4 (blue), and 6.6 (green). The red line illustrates how, for small values of $\beta$, we expect that a first-order phase transition always occurs when we perform a mass scan in the two-dimensional space of $am_0^f$ and $am_0^{as}$. With moderate $\beta$, exemplified by the blue line, the first-order lines disappear in some central region of parameter space, in which both species of fermions have small masses. We expect the first-order surface to be asymmetric with respect to the exchange of $am_0^{as}$ and $am_0^f$, as suggested by the different critical values of $\beta$. If we further increase $\beta$, one of the two lines disappears, and the line of first-order transitions only exists for heavy ($as$) fermions, regardless of the treatment of the ($f$) fermions. Eventually, we expect even this line to disappear at larger values of $\beta$.

To provide numerical support for the conjectured phase diagram in Fig. 2, we start by performing mass scans for several representative sections of the parameter space at fixed $\beta = 6.4$, chosen to cut across the phase boundary— the blue line in the figure. Figure 3 depicts the regions of parameter space of interest. Numerical results in the five segments of parameter space denoted by A, B, C, D, and E are shown in some detail in Fig. 4. We compute the average plaquette values using ensembles generated on lattice of size $8^4$, with an initial configuration of either unit (cold) or random (hot) link variables.

We find strong evidence of hysteresis in cases A, B, and E, indicating the existence of a first-order phase transition, in correspondence to the thick blue lines in Fig. 3. By comparing the behavior in the segments A and B, the wider
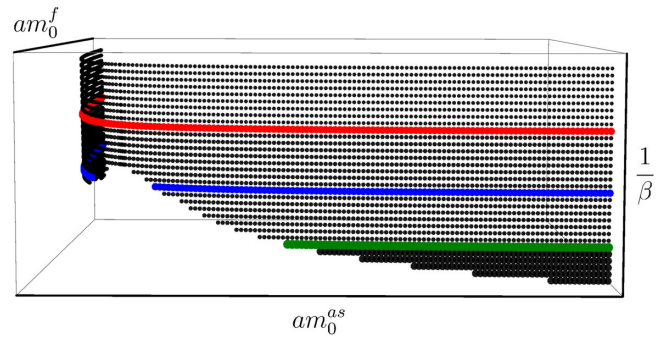


FIG. 2. A schematic representation of the phase diagram in the space of bare parameters of the $Sp(4)$ gauge theory coupled to $N_f = 2$ fundamental and $n_f = 3$ two-index antisymmetric Wilson-Dirac fermions. The three bare parameters are the lattice gauge coupling, $\beta$, and the bare fermions masses, $am_0^f$ and $am_0^{as}$, for the fundamental and antisymmetric representations, respectively. The black-dotted surface denotes the location of first-order bulk phase transitions. On this surface with boundary, we identify three lines of phase transitions at fixed coupling $\beta$: red, blue, and green denote choices of decreasing coupling. The red line is continuous, while the blue and green lines are interrupted, as they cross the boundary of the surface. A critical line of second-order phase transitions is met at the end of first-order lines, followed by intervals in the numerical values of the masses for which a smooth crossover takes place.

mass range over which hysteresis exists in the former case seems to indicate that the strength of the phase transition grows as $am_0^f$ increases, so that we expect that the first-order lines persist all the way to the infinite mass case, for which either the fundamental or antisymmetric fermions
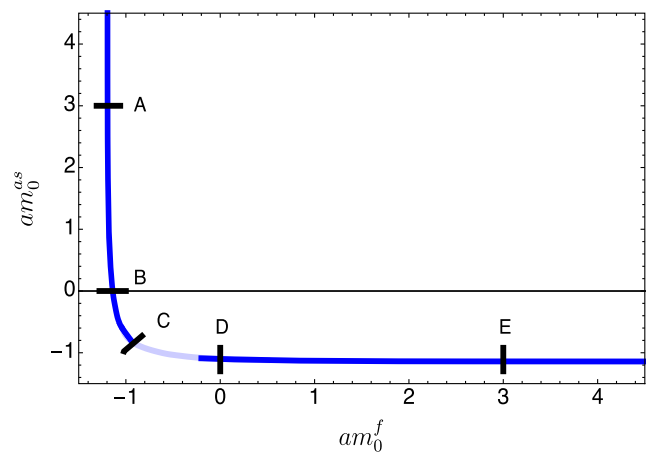


FIG. 3. A schematic representation of the phase structure in the $Sp(4)$ gauge theory with $\beta = 6.4$, concomitantly coupled to $N_f = 2$ fundamental and $n_f = 3$ two-index antisymmetric fermions, as a function of the two bare masses $am_0^f$ and $am_0^{as}$. The blue solid line is the same what appears in Fig. 2, and it consists of first-order bulk phase transitions, while along the light blue a smooth crossover takes place.
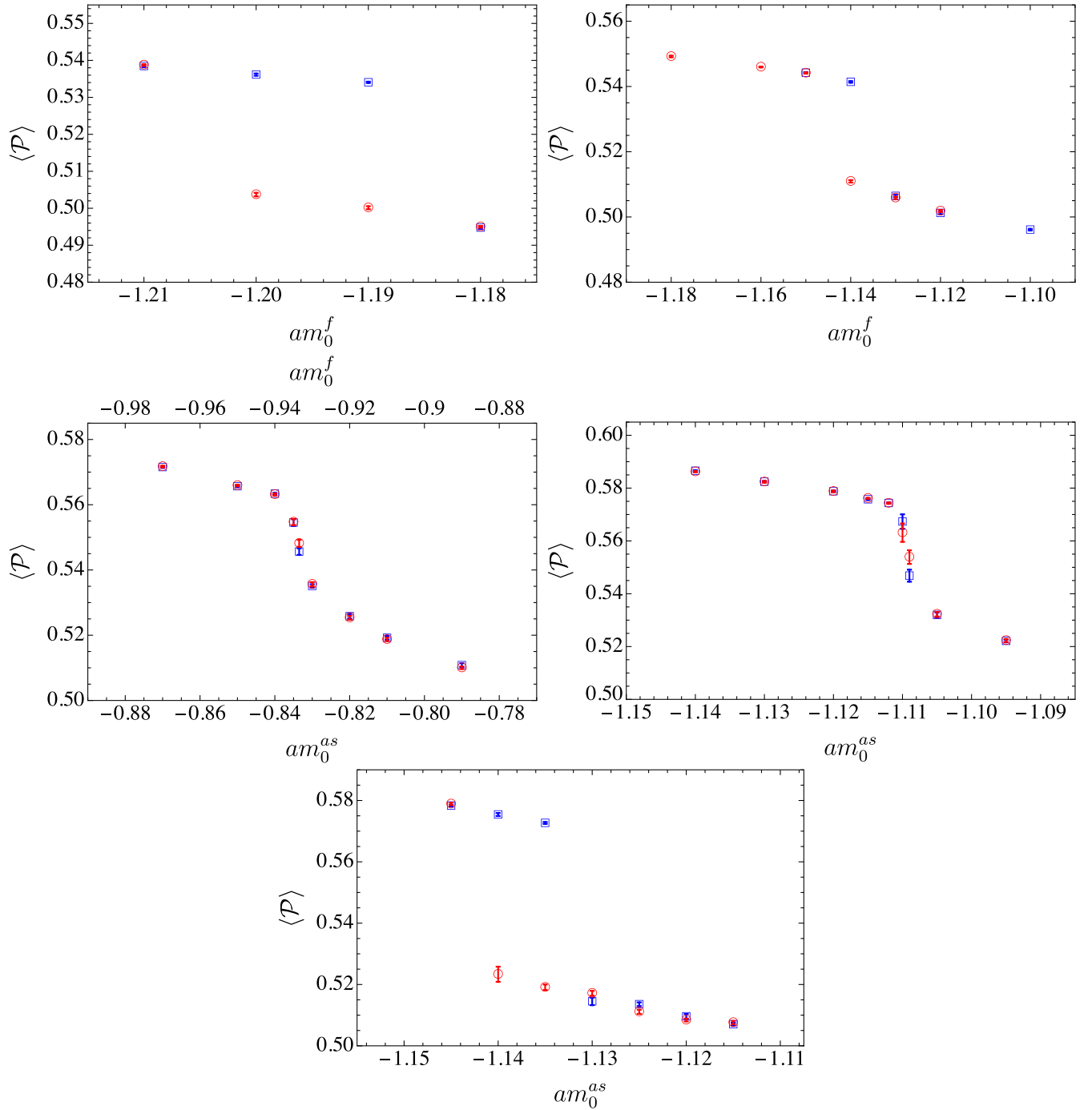
FIG. 4.    Average value $\langle \mathcal{P} \rangle$ of the plaquette, computed with ensembles that start even from cold (unit, blue squares) and hot (random, red circles) configurations, for lattice with dimension $8^4$. From top-left to bottom panel, the lattice parameters correspond to the segments denoted by A, B, C, D, E in Fig. 3.

are nondynamical (quenched). In the heavy mass limits, this is consistent with recovering earlier results in the literature [86,87].

In cases C and D, Fig. 4 no longer shows clear evidence of strong hysteresis. Yet, in proximity of the points with steepest slope, we find that the fluctuations between two preferred plaquette values in the Monte Carlo trajectories display long autocorrelation time. Illustrative examples for the two cases are shown in Fig. 5. The combination of weaker transition and longer correlation length are typical behaviors expected in proximity to the end of first-order lines, that reach critical points, before giving way to a crossover region. We illustrate this behavior with the light blue line in Fig. 3.
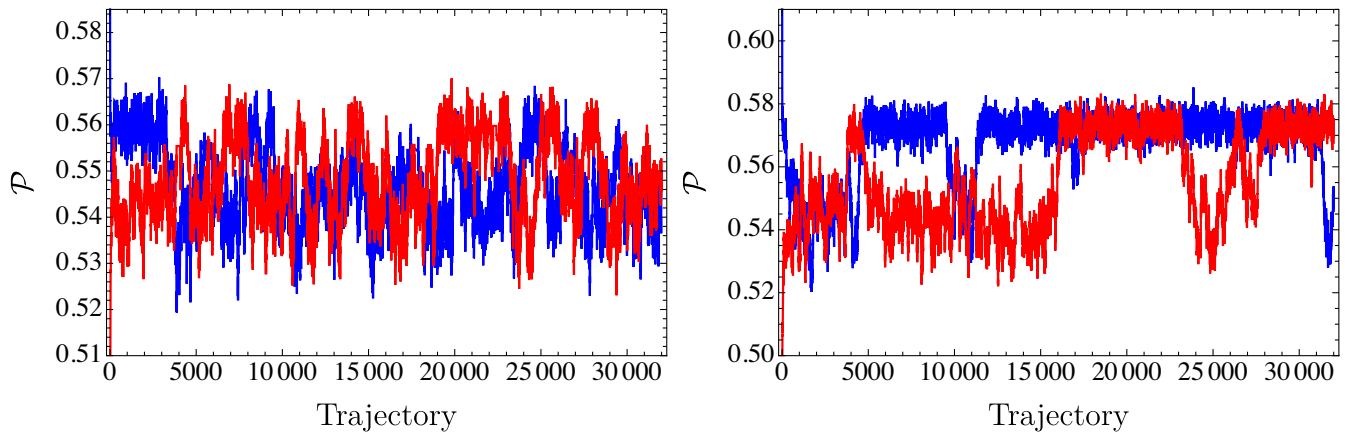
FIG. 5. Illustrative examples of Monte Carlo trajectories of the plaquette $\mathcal{P}$. The lattice parameters are $(\beta, am_0^f, am_0^{as}) = (6.4, -0.8335, -0.9335)$ (left panel) and $(6.4, 0.0, -1.11)$ (right panel). These correspond to two sets of parameters belonging to segments C and D, respectively, in Fig. 3. We use the lattice with size $8^4$. The diagrams are obtained with ensembles generated from hot (red) and cold (blue) start. Small but persistent hysteresis effects are clearly visible, with long self-correlation appearing.

To further substantiate these claims, we carry out a finite-volume analysis of the plaquette susceptibilities at a fixed value of $\beta$ and of the mass of the fundamental fermions $am_0^f = -0.6$. These choices identify a region lying between C and D in Fig. 3. The results of this analysis are shown in Fig. 6: in the upper and lower panels we plot the average value of the plaquette $\langle \mathcal{P} \rangle$ and the susceptibilities $\chi_{\text{plaq}}$, respectively, measured in three different volumes and for various choices of the mass of the antisymmetric fermions. The value of the plaquette interpolates between two values typical of the two phases of the theory. But we find that the height of the peak of $\chi_{\text{plaq}}$ is independent of the volume, which is a typical signature of a smooth crossover.

We next would like to measure the critical coupling $\beta_{\text{cr}}^{mr}$, at the boundary of the surface of first-order phase transitions. We are particularly interested to determine the values of $\beta$ that are large enough that there is no phase transition, for finite masses for the both types of fermions. To exemplify the process, we start by fixing the fundamental fermion mass $am_0^f = -0.6$. We consider a range of values of $\beta$ smaller than 6.4, adjust the value of $am_0^{as}$ in proximity of the phase transition, and calculate $\delta_{\langle \mathcal{P} \rangle} = |\langle \mathcal{P} \rangle_{\text{cold}} - \langle \mathcal{P} \rangle_{\text{hot}}|$, the difference between the average plaquette value measured in ensembles with cold and hot initial configurations. The results are shown in Fig. 7. The strong- and weak-coupling regimes are separated by the existence of a first-order phase transition for $\beta$ smaller than the critical coupling $\beta_{\text{cr}}^{mr} \simeq 6.3$. Conversely, for larger values there are regions of parameter space with $\delta_{\langle \mathcal{P} \rangle} = 0$, signaling a crossover. The final result of this analysis is that as long as our lattice calculations are performed with values of $\beta \gtrsim 6.3$, for appropriate choices of fermion masses the theory is in the weak-coupling phase, and

the results extrapolate smoothly to the continuum theory. We notice that this numerical result is smaller than the aforementioned cases where one of the fermion species is infinitely heavy.
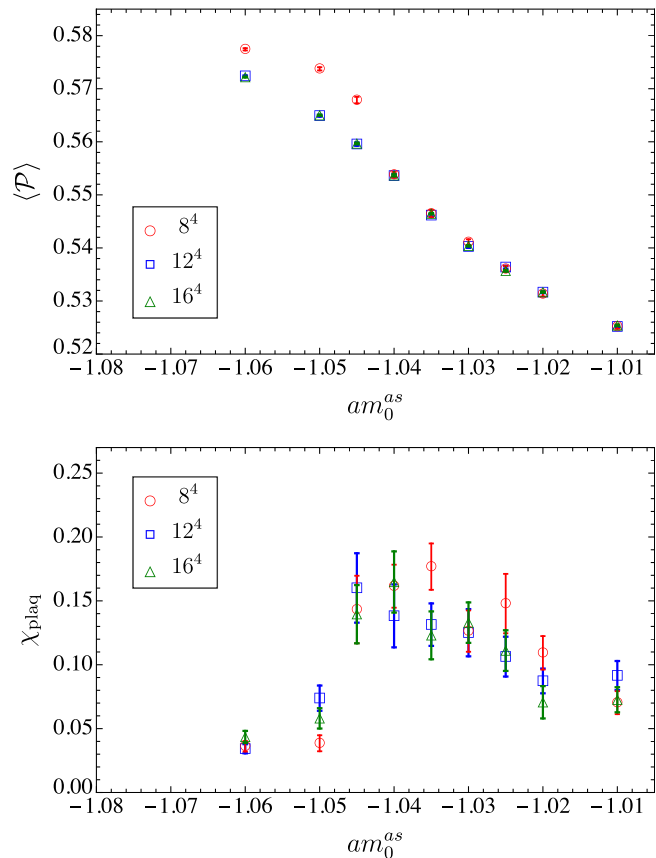


FIG. 6. Average plaquette $\langle \mathcal{P} \rangle$ (top panel) and its susceptibility $\chi_{\text{plaq}}$ (bottom panel), for three choices of lattice volume, as indicated in the legends. The lattice parameters $\beta = 6.4$ and $am_0^f = -0.6$ are fixed, and display the dependence on $am_0^{as}$.
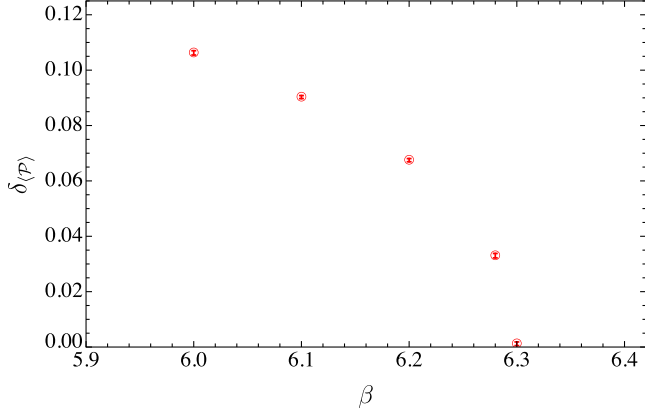
FIG. 7.   Illustrative example of the difference $\delta_{\langle \mathcal{P} \rangle}$ between the average plaquette values obtained from ensembles generated with cold (unit) and hot (random) initial configurations. The mass of the fundamental fermions $am_0^f = -0.6$ is held fixed, and for each value of $\beta$ we vary the bare mass of the antisymmetric fermions $am_0^{as}$, until reaching the proximity of the transition—at which $\delta_{\langle \mathcal{P} \rangle}$ is maximized. The lattice size is $8^4$ for the three small $\beta$ values and $12^4$ for the rest.

The useful fixed point of our lattice theory, bringing it in contact with the desired continuum theory, is reached in proximity of $am_0^f = am_0^{as} = \beta^{-1} = 0$. Our investigation of the phase structure revealed the existence of a boundary to the surface of first-order phase transitions, as shown in Fig. 2. Along this boundary, we collected indications compatible with the phase transition being of second order. Although these are bulk properties of the lattice theory, it is worth analyzing the physical features associated with such second-order transitions, as these fixed points might be used to define the continuum limit to alternative theories. We want to understand whether such theories might be interesting in themselves.

To this purpose, we carry out an exploratory study in proximity of the second-order phase transitions. We fix the

lattice coupling slightly above its critical value, $\beta = 6.35$, such that the theory displays a crossover region. We hold fixed also the mass of the fundamental fermions $am_0^f = -0.6$. We then perform a scan over values of $am_0^{as}$ to identify the crossover region. In Fig. 8, we show the results of the average plaquette $\langle \mathcal{P} \rangle$, and its susceptibility $\chi_{\text{plaq}}$, adopting a lattice with size $24 \times 12^3$. The critical mass is $am_{0,\text{cr}}^{as} \simeq -1.068$.

With the same ensembles, we then measure the masses of pseudoscalar, vector, and scalar mesons, as well as the decay constant of the pseudoscalar meson, focusing on bound states with constituents $(as)$ fermions. As shown in Fig. 9, we find no nontrivial behaviors in these quantities. In Fig. 10, we also present the masses in units of $f_{\text{PS}}^{as}$, and the mass ratio between vector and pseudoscalar mesons. Again, we do not find any interesting features associated with the fixed points in the meson spectrum. Our findings are compatible with interpreting the theories living at the second-order fixed points along the critical boundary in terms of a noninteracting scalar field theory. A dedicated, systematic, high-precision study of the theory in proximity of the critical values of the lattice parameters would be needed to ascertain whether this is the case, but we do not find any alluring evidence to the contrary, at the level of precision of this study.

### B. Spectrum of the Dirac operator

As discussed in Sec. III C, the $SU(4) \times SU(6)$ global symmetry is expected to break to its $Sp(4) \times SO(6)$ subgroup. The symmetry-breaking pattern can be tested through a comparison with the chRMT predictions, as was done for example in Ref. [73] for a $SU(4)$ theory with mixed fermion representations. As a preliminary exercise, which we do not report here, we checked that we could produce the expected results for the $SU(2)$ and $SU(4)$ theories with (quenched) fundamental fermions. We
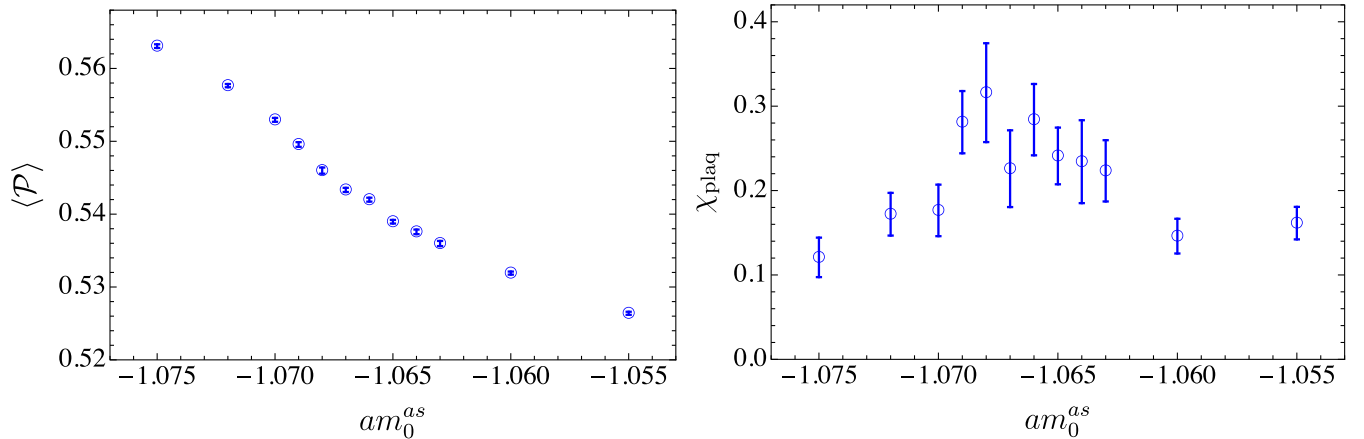


FIG. 8.   Average plaquette value $\langle \mathcal{P} \rangle$ (left panel) and its susceptibility $\chi_{\text{plaq}}$ (right panel), as a function of the mass $am_0^{as}$, having fixed the other lattice parameter to be $\beta = 6.35$ and $am_0^f = -0.6$. The lattice volume is $24 \times 12^3$.
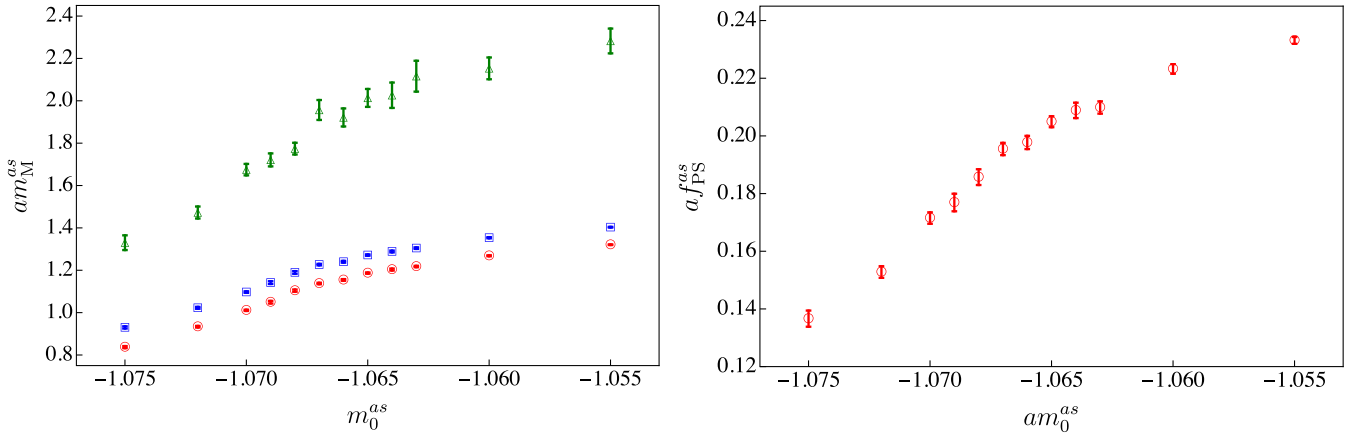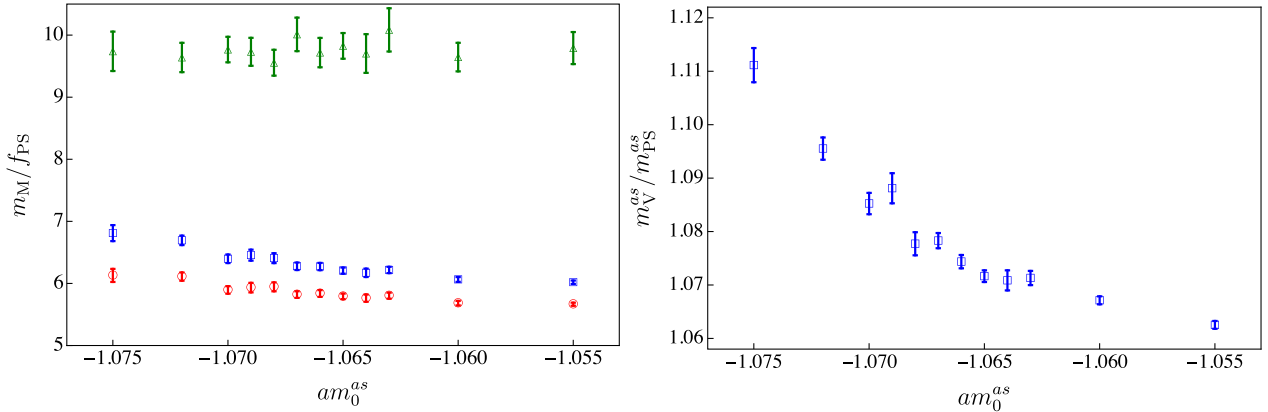
FIG. 9. Left: masses, in lattice units, of the pseudoscalar (red circles), vector (blue squares), and scalar (green triangles) flavored mesons composed of fermions in the antisymmetric representation, as a function of $am_0^{as}$. Right: decay constant, in lattice units, of the pseudoscalar meson composed of $(as)$ fermions, as a function of the bare mass $am_0^{as}$. The other lattice parameters are fixed by $\beta = 6.35$ and $am_0^f = -0.6$. The lattice volume is $24 \times 12^3$.



FIG. 10. Left: masses, in units of the pseudoscalar decay constant, of the pseudoscalar (red circles), vector (blue squares), and scalar (green triangles) flavored mesons composed of fermions in the antisymmetric representation, as a function of $am_0^{as}$. Right: ratio of the masses of the vector and pseudoscalar meson composed of $(as)$ fermions. The other lattice parameters are fixed by $\beta = 6.35$ and $am_0^f = -0.6$. The lattice volume is $24 \times 12^3$.

discuss in the following the tests we carried out for the $Sp(4)$ gauge theory of interest to this paper.

Following the procedure illustrated in Sec. IV A, we compute the eigenvalues of the Hermitian Wilson-Dirac operators, which are real regardless of the fermion representation, for fermions in the fundamental and antisymmetric representations. We then extract the distribution $P(s)$ of the unfolded density of spacings of the eigenvalues, with the discretized definition of $s$ in Eq. (44). For this exercise, we use quenched ensembles with coupling $\beta = 8.0$ and lattice size $4^4$. We fix the masses of the fermions to be $am_0^f = am_0^{as} = -0.2$. We recall that, in the case of $(as)$ fermions, the eigenvalues of the Hermitian Wilson-Dirac operator are expected to have degeneracy 2. This property follows from the fact that the fermionic determinant is positive definite, as discussed in Sec. III C. As an illustration, we show in Fig. 11 the sequence of the smallest
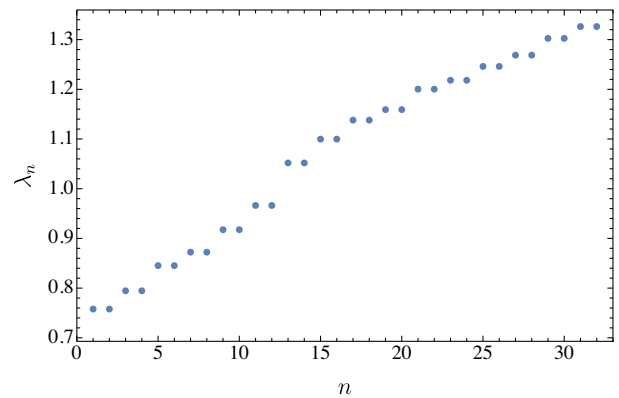


FIG. 11. Numerical results for the smallest (positive) eigenvalues of the Dirac operators for $(as)$ fermions, measured in the quenched $Sp(4)$ ensemble with $\beta = 8.0$ and the lattice size of $4^4$. The mass of the fermion in the antisymmetric representation is $am_0^{as} = -0.2$.
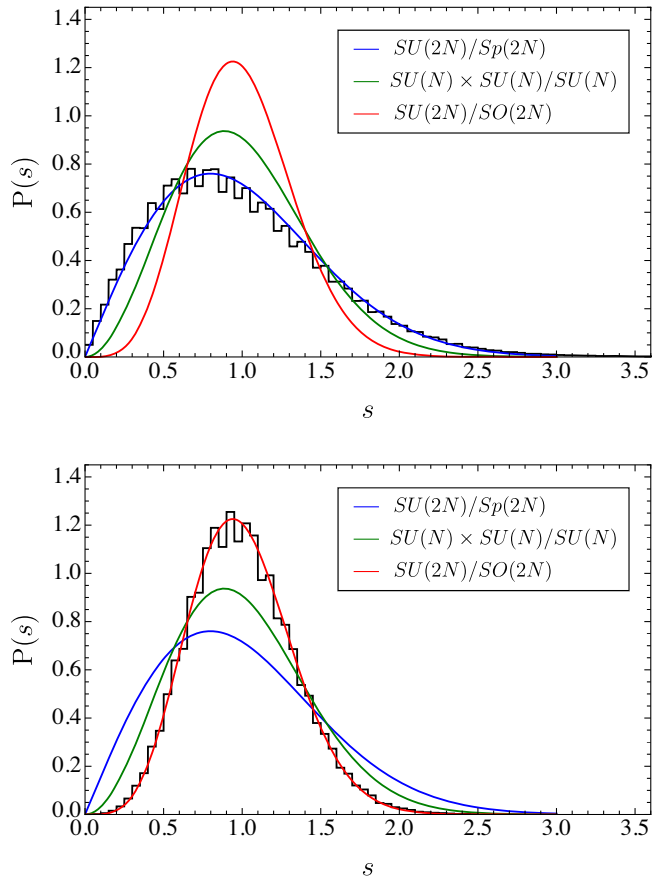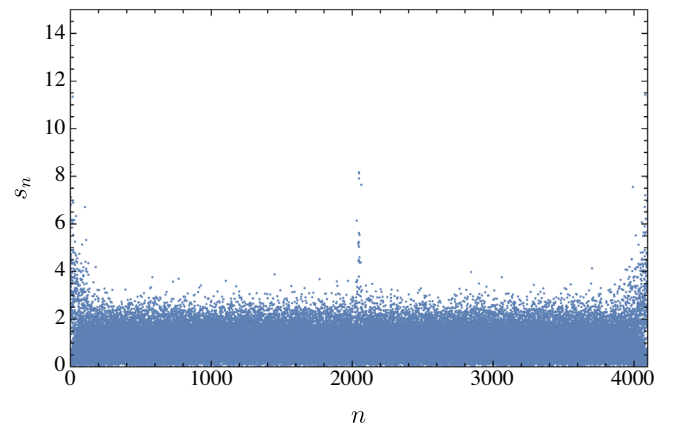
FIG. 13. The unfolded density of spacing between subsequent Dirac eigenvalues $s_n$, as defined in Eq. (44), at the position of the $n$th eigenvalue for the $Sp(4)$ gauge theory in the quenched approximation, with $\beta = 8.0$, for fermions in the fundamental representation. with bare mass of $am_0^f = -0.2$. For this illustrative plot, we randomly chose 20 out of the 192 configurations.

FIG. 12. Histogram (black solid lines) of the distribution of unfolded density of spacing $P(s)$ between subsequent Dirac eigenvalues in the $Sp(4)$ lattice gauge theory in the quenched approximation, with coupling $\beta = 8.0$, fermion masses $am_0^f = am_0^{as} = -0.2$, and lattice of size $4^4$. The number of configurations is 192, while the number of eigenvalues in each configuration used for the $(f)$ fermions (top panel) is 4096, while for the $(as)$ fermions (bottom panel) it is 5120. The curves depict, for different symmetry-breaking patterns, the predictions from matrix theory, Eq. (41).

positive eigenvalues of this operator for $(as)$ fermions for our choice of lattice parameters, which provides support for the expected double degeneracy. The presence of a largish mass gap below the lowest eigenvalue in our measurements is due to the comparatively large value of the fermion mass.

In the upper and lower panels of Fig. 12, we show histograms of the unfolded density of the eigenvalue spacings for fermions in the fundamental and antisymmetric representations, respectively. The numerical results are compared to the chiral RMT predictions for chGOE, chGUE, and chGSE ensembles, defined in Eq. (41) with $\bar{\beta} = 1, 2, 4$—for convenience, in the legend we label the predictions by the associated symmetry-breaking pattern. As shown in the figures, we find that the distributions are in good agreement with the chRMT predictions.

While the agreement is very convincing for $(as)$ fermions (bottom panel), one can detect a slight mismatch between the chRMT prediction and the numerical results in the case of $(f)$ fermions (top panel). By inspecting the details provided in Fig. 13, one sees that such a discrepancy is associated with some abnormally large spacings for the smallest and largest eigenvalues. We interpret this as an artifact due to the finiteness of the size of the matrices. We hence expect the distortion of the distribution to becomes less pronounced as the size of Dirac matrix increases, i.e., by going towards larger $N$, larger lattices, and higher representations $R$. For instance, the results of the same calculations for the $(f)$ fermions, but on a smaller lattice volume of $3^4$, is shown in Fig. 14. The deviations with the chRMT predictions are larger, compared to the $4^4$ lattice. Notice in particular that the total numbers of eigenvalues are 4096 and 5120 for the fundamental and antisymmetric representations of $Sp(4)$ with the $4^4$ lattice, respectively, while for the $(f)$ fermions with lattice volume of $3^4$ such number is 1296.

To further support this interpretation, we recalculate the unfolded density for the same theories, but excluding small and large eigenvalues. By doing so we aim at demonstrating that our action and algorithms yield a theory that reproduces the expected symmetry-breaking patterns.

We find that, to do so, it suffices to exclude a few hundred eigenvalues at the extrema of the spectrum. The resulting density distributions for fermions in the fundamental representation measured on lattices of sizes $4^4$ and $3^4$ are shown in the upper and lower panels of Fig. 15, respectively. As expected, in this case the difference between the numerical results and chRMT predictions is no longer visible to the naked eye. We remind the reader that these are quite small lattices, compared to what one
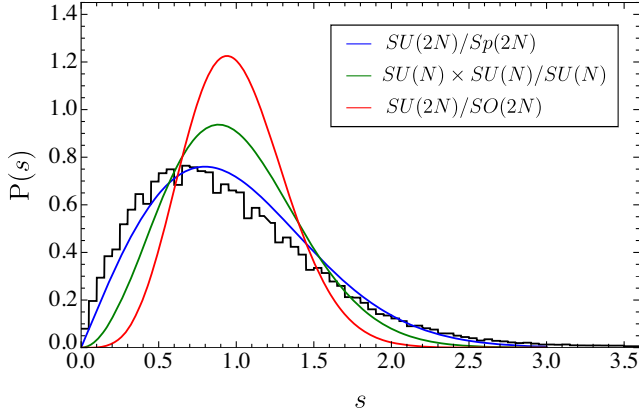
FIG. 14. Histogram of the distribution of unfolded density of the spacing between subsequent Dirac eigenvalues for fermions transforming in the fundamental representation of $Sp(4)$, in the quenched approximation, with $\beta = 8.0$, mass of the $(f)$ fermion $am_0^f = -0.2$, and on a lattice with size $3^4$. The number of configurations is 196, while the number of eigenvalues in each configuration is 1296.
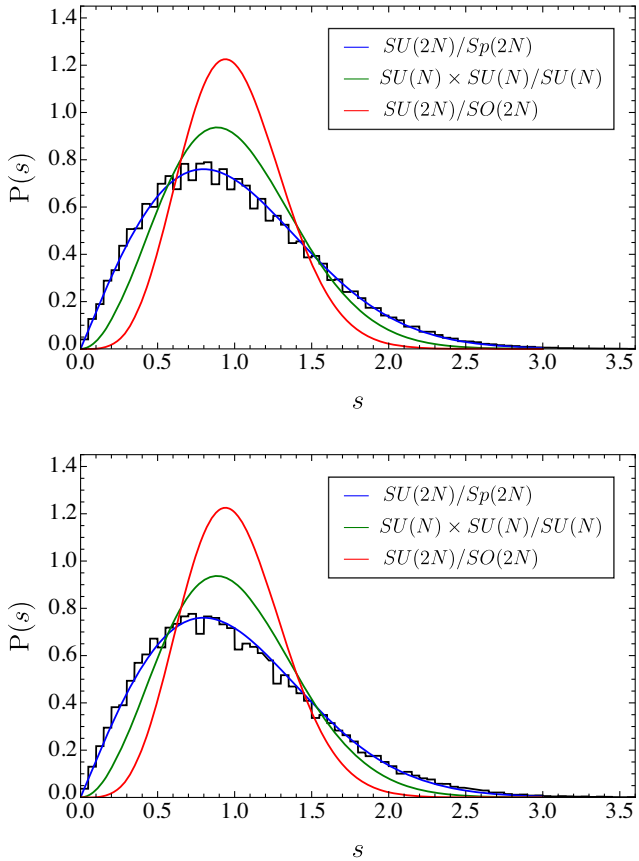




FIG. 15. Histograms of the unfolded density of spacing between subsequent Dirac eigenvalues for the $Sp(4)$ gauge theory in the quenched approximation, with coupling $\beta = 8.0$ and with $(f)$ fermions with mass $am_0^f = -0.2$, on lattices of size $4^4$ (top panel) and $3^4$ (bottom panel). The calculated eigenvaluesl are the same used in Figs. 12 and 14 with the notable exception that a few hundred spacings at the smallest and largest eigenvalues have been discarded.

normally considers for dynamical lattice calculations. We can hence conclude that the HiRep code correctly implements also Dirac fermions transforming in the fundamental and antisymmetric representations of the $Sp(4)$ gauge group.

## C. Finite volume effects

In this section, we show the results of our numerical investigations of finite-volume effects in our measurements. Following lattice QCD lore, we start by studying the volume dependence of the mass of pseudoscalar mesons, the lightest states in the spectrum of composite objects. In the upper and lower panels of Fig. 16 we show our results for the masses (in lattice units) of pseudoscalar mesons with $(f)$ and $(as)$ fermion
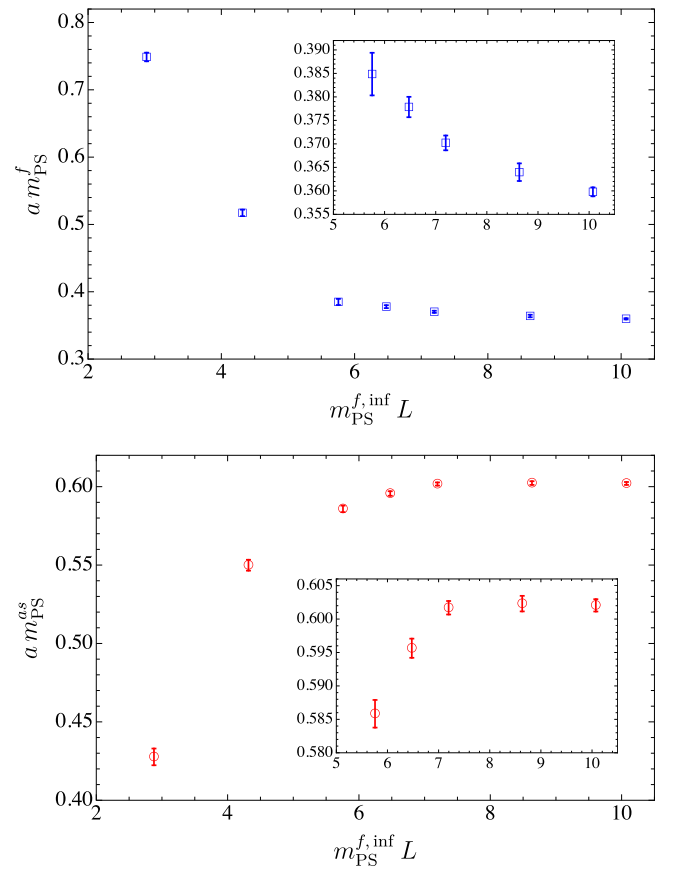


FIG. 16. Masses (in lattice units) of pseudoscalar mesons composed of constituent fermions transforming in the fundamental (top panel) and antisymmetric (bottom panel) representations, as a function of the combination $m_{\mathrm{PS}}^{f,\mathrm{inf}} L$. We denote by $m_{\mathrm{PS}}^{f,\mathrm{inf}} a$ the mass of the pseudoscalar extracted from the largest available lattice, with lattice of volume $54 \times 28^3$. The lattice parameters $\beta = 6.5$, $am_0^f = -0.71$, $am_0^{as} = -1.01$ are held fixed, and repeat the measurement of the mass of the pseudoscalar while we vary the size of the lattice. The smaller inset plots display a detail of the enclosing figures, with the range on the vertical axis restricted to highlight the plateaux in the rightmost points.
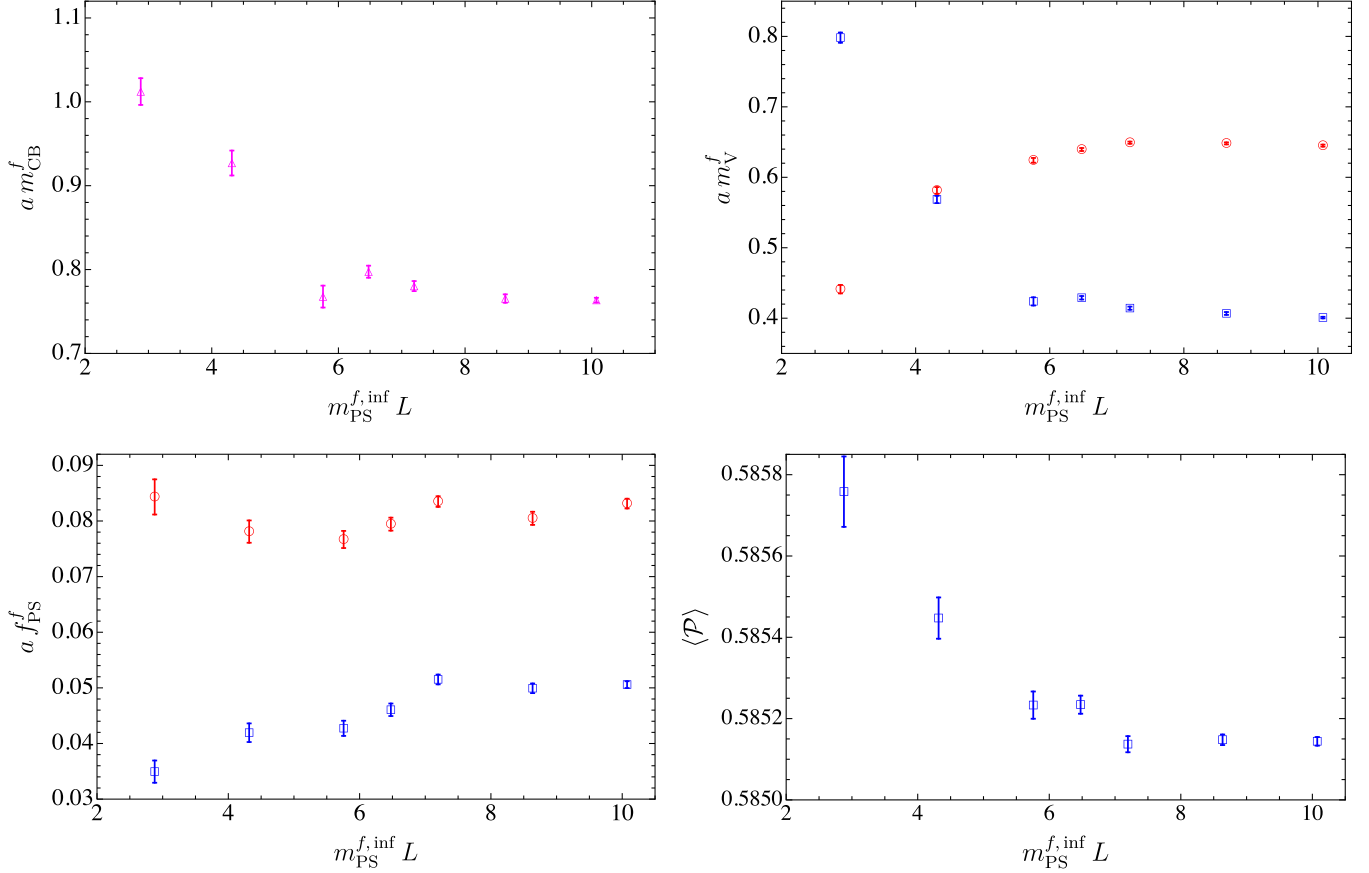
FIG. 17. Volume dependence of numerical observables: the mass of the Chimera baryon (top left), the vector meson masses (top right), the decay constants of pseudoscalar mesons (bottom left), and the average value of plaquettes for the fundamental gauge links (top right). In the cases of meson masses, red and blue colors denote the mesons composed of constituent fermions in the antisymmetric and fundamental representations, respectively. We denote by $m_{\mathrm{PS}}^{f,\mathrm{inf}} a$ the mass of the pseudoscalar extracted from the largest available lattice, with the lattice volume $54 \times 28^3$, as in Fig. 16. The lattice parameters are $\beta = 6.5$, $am_0^f = -0.71$, $am_0^{as} = -1.01$.

constituents, respectively, for varying $m_{\mathrm{PS}}^{f,\mathrm{inf}} L$. We use seven different lattice sizes, six of them have timelike extent $N_t = T/a = 48$ and spacelike extent $N_s = L/a = 8$, 12, 16, 18, 20, 24; the largest lattice has size $54 \times 28^3$. Details and numerical results are displayed in Appendix C, and are also available in machine-readable form in Ref. [159]. The mass measured from the largest lattice has been identified with $m_{\mathrm{PS}}^{f,\mathrm{inf}}$. We fix the lattice coupling to $\beta = 6.5$, so that the data points are well inside the weak coupling regime. The bare masses are $am_0^f = -0.71$ and $am_0^{as} = -1.01$. The pseudoscalar composed of $(f)$ fermions are lighter than those composed of $(as)$ fermions. As shown in the lower panel of Fig. 16, we find that finite-volume corrections to the mass of the pseudoscalar mesons composed of $(as)$ fermions can be neglected, compared to statistical fluctuations, for $m_{\mathrm{PS}}^{f,\mathrm{inf}} L \gtrsim 7$. In the case of fundamental fermion constituents, the convergence is rather slow, and the size of finite-volume effects becomes less than one percent and compatible with the statistical errors only when

$m_{\mathrm{PS}}^{f,\mathrm{inf}} L \gtrsim 8.5$. Achieving higher precision would require one to restrict the analysis to even larger values $m_{\mathrm{PS}}^{f,\mathrm{inf}} L$, yet, given the precision goals of this paper, this is a sufficient threshold to allow us to safely ignore finite-volume effects.

We repeat the same exercise for the following observables: the masses of the chimera baryons, the vector meson masses, the decay constants of the pseudoscalar mesons, and the average plaquette values for the fundamental gauge links. We display the results in Fig. 17. For all of these observables we find that finite-volume corrections can be safely neglected, if we constrain the lattice size by imposing the constraint $m_{\mathrm{PS}}^{f,\mathrm{inf}} L \gtrsim 7$. We could therefore conclude that our conservative estimate of the minimum size of the lattice, such that the finite-volume effects are well under control, corresponds to $m_{\mathrm{PS}}^{f,\mathrm{inf}} L \simeq 8.5$.

For pseudoscalar and vector meson masses, we observe that the finite-volume corrections have opposite signs, depending on the constituent fermions: the difference $am_M^{\mathrm{FV}} - am_M^{\mathrm{inf}}$ between finite- and infinite-volume measurements is positive with $(f)$ fermion constituents and negative with $(as)$ fermion constituents. This behavior can

be explained in the context of chiral perturbation theory ($\chi$PT), as the finite-volume corrections arise from pseudo-scalar states wrapping around each spatial extent of the lattice. In particular, the next-to-leading order (NLO) expression of the pseudoscalar mass at finite volume is given by

$$m_{PS}^2 = M^2 \left(1 + a_M \frac{A(M) + A_{FV}(M)}{F^2} + b_M(\mu)\frac{M^2}{F^2} + \mathcal{O}(M^4)\right),$$
(72)

where $M$ and $F$ are the mass and decay constant of the pseudoscalar meson in the massless limit, obtained by replacing the one-loop integrals with finite sums. $A(M)$ is the one-loop contribution at infinite volume, known as the chiral logarithm, $A(M) = -\frac{M^2}{16\pi^2}\log\frac{M^2}{\mu^2}$ with $\mu$ the renormalization scale. The finite-volume contribution $A_{FV}(M)$ arises from a finite sum on a cubic box of size $L$ with periodic boundary condition (see, e.g., the Appendix of Ref. [161]). At the leading order, the difference between the sums and the integrals is

$$A_{FV}(M) \overset{ML\gg1}{\to} -\frac{3}{4\pi^2}\left(\frac{M\pi}{2L^3}\right)^{1/2}\exp[-ML].$$
(73)

The coefficients $A(M)$ and $A_{FV}(M)$ in Eq. (72) are independent of the details of the theory, which are solely encoded in their coefficient $a_M$ [162]:

$$a_M = \begin{cases} -\frac{1}{2} - \frac{1}{N_f}, & \text{for } SU(2N_f) \to Sp(2N_f), \\ -\frac{1}{N_f}, & \text{for } SU(N_f) \times SU(N_f) \to SU(N_f), \\ \frac{1}{2} - \frac{1}{2N_f}, & \text{for } SU(2N_f) \to SO(2N_f). \end{cases}$$
(74)

The first and third classes are particularly relevant to our study: the coefficients $a_M$ for two fundamental and three antisymmetric Dirac flavors are $-1$ and $+1/3$, respectively. Together with the fact that $A_{FV}(M)$ is negative, on the basis of these analytical expressions we expect the pseudoscalar mass to receive positive (negative) finite-volume corrections for constituents in the fundamental (antisymmetric) representation, respectively. This is consistent with our
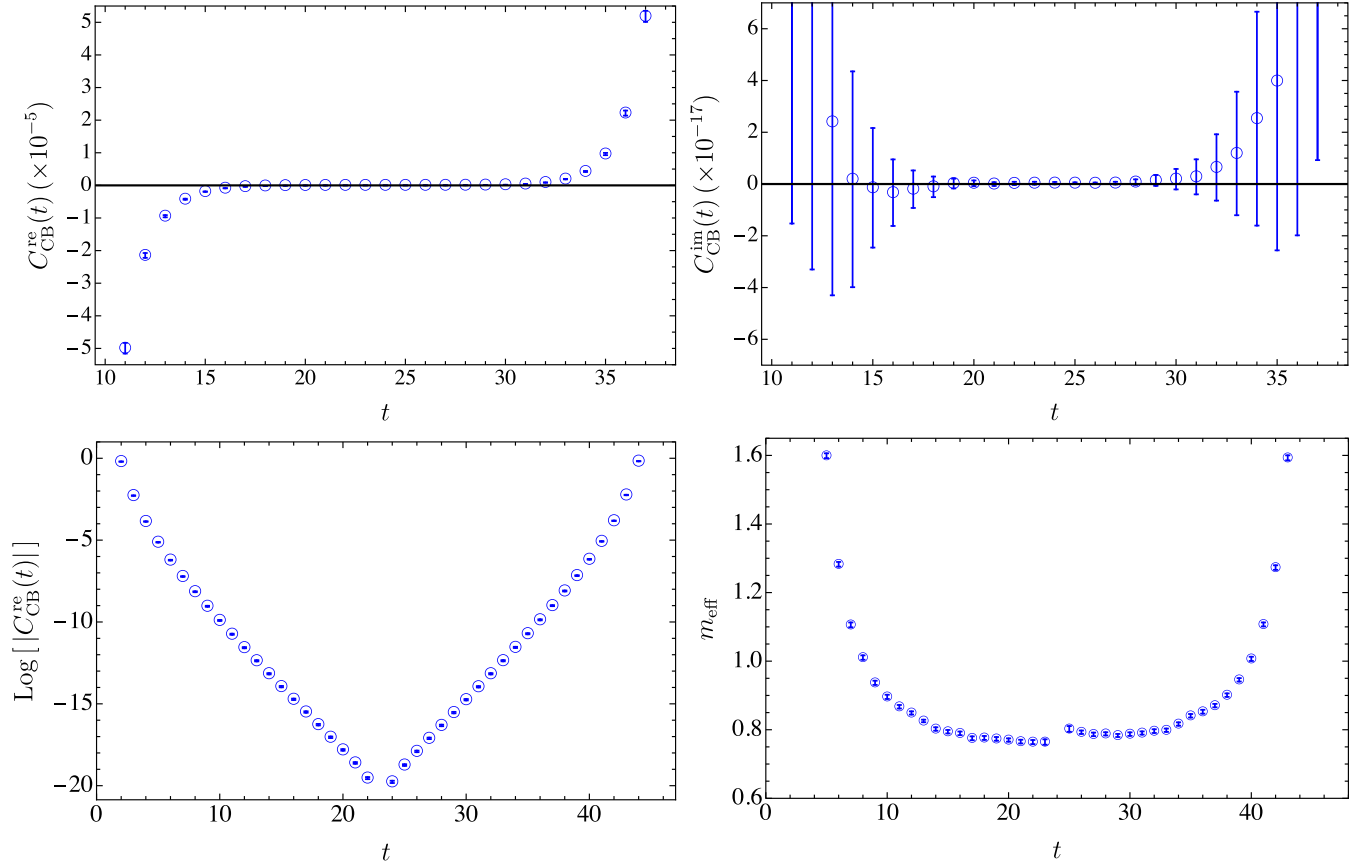


FIG. 18. Top panels: real (top left) and imaginary (top right) parts of the 2-point correlation function of chimera baryons. Bottom left panel: logarithm of the absolute value of the real part of the same correlator. Bottom-right panel: the corresponding effective mass plot. The errors denote for $1\sigma$ deviation estimated by using 200 bootstrap samples. The gauge configurations used for the computation are generated by using the lattice parameters $\beta = 6.5$, $am_0^{as} = -1.01$ and $am_0^f = -0.71$ on a lattice with size $48 \times 24^3$.
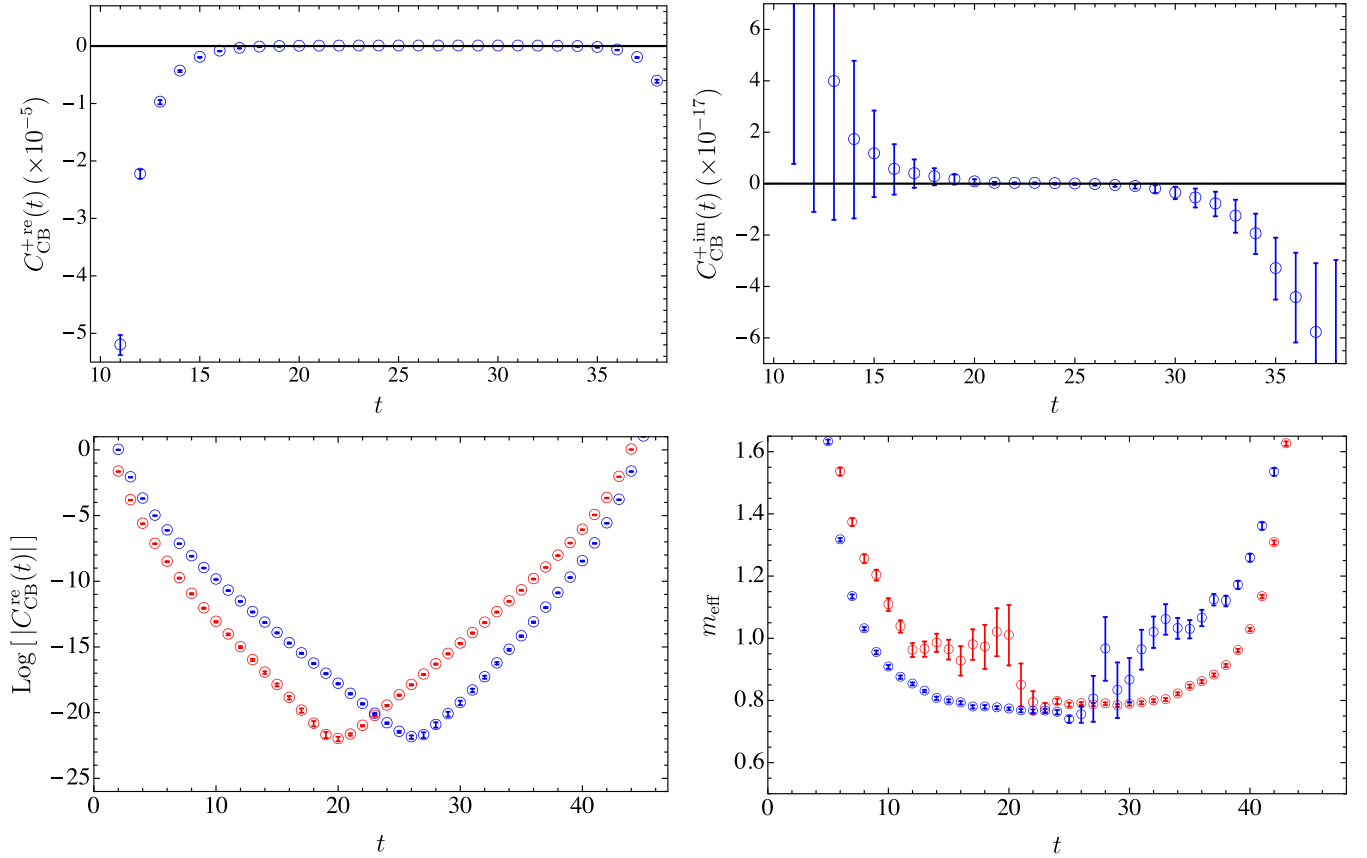
FIG. 19.    Top panels: real (top left) and imaginary (top right) parts of the 2-point correlation function of chimera baryon after positive-parity projection. Bottom-left panel: logarithm of the absolute value of the real part of the same correlator. Bottom-right panel: the corresponding effective mass plot. In the bottom panels, blue empty circles denote the results with positive-parity projection, while red empty circles are obtained with odd-parity projection. The errors denote for $1\sigma$ deviation estimated by using 200 bootstrap samples. The gauge configurations used for the computation are generated by using the lattice parameters $\beta = 6.5$, $am_0^{as} = -1.01$, and $am_0^f = -0.71$ on a lattice with size $48 \times 24^3$.

numerical findings as displayed in Fig. 16, though, in the light of the comparatively large mass of the fermions, one should take a conservative view towards this interpretation.

### D. Correlation functions of chimera baryon

We perform the first numerical calculation of the mass spectrum of chimera baryons in the $Sp(4)$ gauge theory with two ($f$) and three ($as$) Dirac fermions in the sea. Since this type of calculation has never been done before for $Sp(2N)$ gauge theories, we carry out several nontrivial tests using interpolating operators with and without parity projection, as in Eqs. (60) and (68). We notice from the outset the comparatively large values of the ratios $m_{PS}^f/m_V^f \simeq 0.9$ and $m_{PS}^{as}/m_V^{as} \simeq 0.93$.

We first present the numerical results without projection in Fig. 18. We focus on one of the gauge ensembles already used for the study of finite-volume effects in Sec. V C. We find that the real part of the correlation function shows a clear signal of exponential decay, while the imaginary part shows large statistical fluctuations, being of the order of the

machine numerical precision and consistent with zero at every Euclidean time $t$. A symmetry is visible, in the top-left and bottom-left panels, between forward and backward propagation, that differs by having opposite sign at late Euclidean times. This is consistent with our expectations for the asymptotic behavior of the 2-point correlation function in Eq. (71). As is customary, we also define the effective mass as

$$m_{\text{eff}} = \operatorname{arcosh}\left(\frac{C_{\text{CB}}(t+1) + C_{\text{CB}}(t-1)}{2C_{\text{CB}}(t)}\right). \quad (75)$$

An example of the resulting effective mass plot is shown in the bottom-right panel of Fig. 18. The plateau over several time slices centered in the middle of the temporal extent, whose average value is smaller than the effective mass at earlier time, indicates that the exponential decay of the correlator is dominated by the ground state, as expected.

We present in Fig. 19 the numerical results for chimera baryon correlators defined with even and odd parity

projections. In the top-left and top-right panels, we show the real and imaginary parts of the correlation function obtained from the interpolating operator projected onto its positive parity component. Again, the former shows a clear signal of exponential decay, while the latter is dominated by statistical noise, and is consistent with zero. In contrast with the results without the parity projection, however, we find that the real part is negative and asymmetric in time, which is further evidenced by the logarithmic plot in the bottom-left panel.

This result is consistent with the analytical expression for the asymptotic behavior in Eq. (70): the forward and backward propagators at late time result in a single exponential decay whose decay rates are the masses of the lightest parity even and odd states, respectively. Also, when we apply the negative parity projection, which yields the results denoted by red empty circles in the bottom-left and bottom-right panels, we find that the forward and backward propagators exchange their roles, again as expected. Up to half of the temporal extent, furthermore, we find that the signal is stable even at later time for the positive parity case, while we lose it at relatively earlier time, after a faster decay, in the negative parity case.

When looking at the effective mass plots, we cannot identify a clear plateau for the negative parity case. Yet, the combination of all of these results indicates unambiguously that the positive parity state is lighter than the negative one. We conclude that the ground state found in the case without parity projection corresponds to the chimera baryon with positive parity, as we find that the masses associated with the plateaux in the effective mass plots in Figs. 18 and 19 agree with each other. For the purposes of this paper, the discussion of the chimera baryon stops here, yet we will follow up with more thorough investigations of the spectrum in forthcoming publications.

### E. Spectrum of composite states

In Fig. 20, we finally present the mass spectrum of composite states, for an illustrative choice of parameters, in the fully dynamical $Sp(4)$ lattice gauge theory with $N_f = 2$ fundamental and $n_f = 3$ antisymmetric Dirac fermions, which improves a similar, preliminary plot, in Refs. [119,120]. The lattice parameters are the same adopted earlier on, for the study of finite-volume effects, restricted to the available largest volume. Following the discussions in Secs. IV B and IV C, we compute the masses of flavored spin-0 and spin-1 mesons with fermion constituents in the fundamental and antisymmetric representation, as well as the mass of the chimera baryon with positive parity. The numerical values of the results displayed in Fig. 20 can be found in Appendix C.

We observe that, at least for these choices of parameters, the overall behavior of the masses of the lightest states
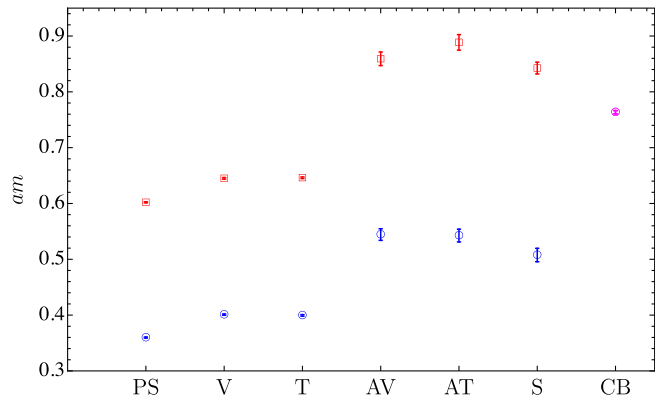


FIG. 20. Masses $am$, in lattice units, of the lightest composite states in the $Sp(4)$ gauge theory coupled to $N_f = 2$ fundamental and $n_f = 3$ antisymmetric fermions. The blue and red colors denote the mesons for which the fermion constituents are in the fundamental and antisymmetric representations, respectively. The magenta color denotes the chimera baryon (CB), for which the constituents are two fermions in the fundamental and one in the antisymmetric representation. The lattice parameters used are $\beta = 6.5$, $am_0^{as} = -1.01$, $am_0^f = -0.71$, while the lattice volume is $N_t \times N_s^3 = 54 \times 28^3$.

sourced by meson operators with different quantum numbers (PS, V, T, AV, AT) is quite similar, when comparing mesons composed of $(f)$ and $(as)$ fermions. Yet, at least in this region of parameter space, the masses of the latter are much heavier than those in the former. The lightest chimera baryon is not light, yet its mass is slightly smaller than that of the scalar meson composed of constituent fermions in the antisymmetric representation, which is encouraging, in view of future extensions of this study and possible phenomenological applications.

### VI. DISCUSSION AND OUTLOOK

This paper reports on a major step in the development of the extensive program of exploration of the dynamics of $Sp(2N)$ gauge theories on the lattice [86,88–91,154]. We considered the lattice field theory with gauge group $Sp(4)$, with matter field content consisting of two Wilson-Dirac fermions transforming in the fundamental representation, together with three transforming in the 2-index antisymmetric representation. Due to the odd number of fermions, the contribution of matter fields to the nonperturbative dynamics is included by implementing a combination of HMC and RHMC algorithms, both of which are supported by the HiRep code [137], which we adapted to the treatment of $Sp(2N)$ groups and to the simultaneous handling of fermions in multiple representations. The continuum limit is the minimal theory—amenable to lattice numerical studies [3]—that provides a UV completion for the strongly coupled sector of extensions of the standard model which combine composite Higgs and partial top compositeness.

We performed the first scan of the three-dimensional parameter space of the lattice theory, finding evidence of the existence of a surface with boundaries separating the strong and weak phases. The theory admits first- as well as second-order (bulk) phase transitions, and we identified values of the lattice parameter space (the coupling $\beta$ and the masses of the two species of fermions $am_0^f$ and $am_0^{as}$) that safely ensure that the lattice theory is connected to the correct continuum one. We tested our algorithms, verifying explicitly that the spectrum of the Dirac operator reproduces the expectations for the chiral symmetry-breaking pattern predicted by (chiral) random matrix theory, as done in Ref. [73] for a $SU(4)$ theory. We assessed the size of finite-volume effects in low-lying composite state masses, and identified criteria that can be imposed to ensure that such lattice artifacts are negligibly small, in comparison with statistical uncertainties. For one choice of lattice parameters, we computed the mass spectra of the lightest mesons with different quantum numbers, as well as those of chimera baryons—see Fig. 20.

The combination of all of the above demonstrates that our lattice program is now ready to start an intensive process of numerical studies focused on the spectra of mesons and chimera baryons in this theory, making contact with the model-building literature. While for the purposes of this publication we used pointlike and stochastic $Z_2$ wall sources for the measurements of the 2-point correlation functions, to improve the signal to noise ratio in the numerical studies we will use smearing techniques, both for the sources and for the dynamical configurations, and both of which have been tested successfully on this model [119,120]. By further combining these techniques with the implementation of an appropriate basis for the variational problem, and of a scale-setting process based on the Wilson flow, such studies will provide access also to some of the excited states in the theory, and we will be able, by varying the lattice parameters, to extrapolate our spectroscopy results towards the continuum limit, in the large region of parameter space with intermediate fermion masses that is of direct interest for models of composite Higgs and partial top compositeness.

The supporting data for this article are openly available from Zenodo [159].

## ACKNOWLEDGMENTS

## APPENDIX A: NOTATION AND CONVENTIONS

In this appendix, we summarize some of the conventions adopted in the construction of the continuum and lattice theories. We display some technical relations which are used in the main text. In particular, we present the chiral representation of the gamma matrices, both in Minkowski and Euclidean space-time, and a choice of generators for the fundamental and antisymmetric representations of $Sp(4)$, which are required to compute the MD forces in the HMC/RHMC algorithms.

### 1. Gamma matrices in Minkowski space

In Sec. II, the continuum model relevant for phenomenological applications is presented in Minkowski space-time. The metric $\eta^{\mu\nu}$ is given by

$$\eta = \begin{pmatrix} 1 & 0 & 0 & 0 \\ 0 & -1 & 0 & 0 \\ 0 & 0 & -1 & 0 \\ 0 & 0 & 0 & -1 \end{pmatrix}, \qquad (A1)$$

where $\mu, \nu = 0, \ldots, 3$ are space-time indexes. The Dirac gamma matrices satisfy the anticommutation relations,[11]

$$\{\gamma_M^\mu, \gamma_M^\nu\} = 2\eta^{\mu\nu}\mathbb{1}_4, \qquad (A2)$$

where $\mathbb{1}_4$ is the unit matrix $\delta^{\alpha\beta}$ in spinor space, with $\alpha, \beta = 1, \ldots, 4$. Hence, $\gamma_M^0 = \gamma_M^{0\dagger}$, while $\gamma_M^i = -\gamma_M^{i\dagger}$ for $i = 1, 2, 3$, and the Hermiticity condition $\gamma_M^{\mu\dagger} = \gamma_M^0 \gamma_M^\mu \gamma_M^0$ holds. We adopt the chiral basis, and write explicitly the matrices as follows:

$$\gamma_M^0 = \begin{pmatrix} \mathbb{0}_2 & \mathbb{1}_2 \\ \mathbb{1}_2 & \mathbb{0}_2 \end{pmatrix}, \qquad \gamma_M^i = \begin{pmatrix} \mathbb{0}_2 & -\tau^i \\ \tau^i & \mathbb{0}_2 \end{pmatrix}, \qquad (A3)$$

with the Pauli matrices $\tau^i$ read as

$$\tau^1 = \begin{pmatrix} 0 & 1 \\ 1 & 0 \end{pmatrix}, \qquad \tau^2 = \begin{pmatrix} 0 & -i \\ i & 0 \end{pmatrix}, \qquad \tau^3 = \begin{pmatrix} 1 & 0 \\ 0 & -1 \end{pmatrix}. \qquad (A4)$$

With this choice, the $\gamma_M^5$ matrix and the charge-conjugation matrix $C_M$ are defined as

$$\gamma_M^5 = i\gamma_M^0 \gamma_M^1 \gamma_M^2 \gamma_M^3 = \begin{pmatrix} \mathbb{1}_2 & \mathbb{0}_2 \\ \mathbb{0}_2 & -\mathbb{1}_2 \end{pmatrix},$$

$$C_M = i\gamma_M^2 \gamma_M^0 = \begin{pmatrix} -i\tau^2 & \mathbb{0}_2 \\ \mathbb{0}_2 & i\tau^2 \end{pmatrix}, \qquad (A5)$$

where the former defines the chirality as in Eq. (20) and satisfies $\{\gamma_M^\mu, \gamma_M^5\} = 0$, while the latter obeys the defining relations $C\gamma_M^\mu C^{-1} = -\gamma_M^{\mu T}$ and $CC^\dagger = \mathbb{1}_4 = -C^2$.

### 2. Gamma matrices in Euclidean space

$Sp(2N)$ lattice gauge theories are defined in four-dimensional Euclidean space-time. The anticommutators of the (Hermitian) Euclidean gamma matrices satisfy the relations

$$\{\gamma_E^\mu, \gamma_E^\nu\} = 2\delta^{\mu\nu}\mathbb{1}_4. \qquad (A6)$$

The chiral representation of the gamma matrices has the following explicit form[12]:

$$\gamma_E^0 = \begin{pmatrix} \mathbb{0}_2 & -\mathbb{1}_2 \\ -\mathbb{1}_2 & \mathbb{0}_2 \end{pmatrix}, \qquad \gamma_E^i = \begin{pmatrix} \mathbb{0}_2 & -i\tau^i \\ i\tau^i & \mathbb{0}_2 \end{pmatrix}. \qquad (A7)$$

In this basis, the $\gamma_E^5$ and the charge-conjugation $C_E$ matrices are

$$\gamma_E^5 = \gamma_E^0 \gamma_E^1 \gamma_E^2 \gamma_E^3 = \begin{pmatrix} \mathbb{1}_2 & \mathbb{0}_2 \\ \mathbb{0}_2 & -\mathbb{1}_2 \end{pmatrix},$$

$$C_E = \gamma_E^0 \gamma_E^2 = \begin{pmatrix} i\tau^2 & \mathbb{0}_2 \\ \mathbb{0}_2 & -i\tau^2 \end{pmatrix}. \qquad (A8)$$

The following relations are used in the algebraic manipulations of Secs. III and IV:

$$\{\gamma_E^\mu, \gamma_E^5\} = 0, \qquad (A9)$$

$$\gamma_E^{5\dagger} = \gamma_E^5, \qquad (A10)$$

$$C_E^\dagger = C_E^{-1} = C_E^T = -C_E, \qquad (A11)$$

$$\gamma_E^0 C_E^\dagger \gamma_E^0 = C_E, \qquad (A12)$$

$$\gamma_E^5 \gamma_E^{\mu\dagger} \gamma_E^5 = -\gamma_E^\mu, \qquad (A13)$$

$$C_E^{-1} \gamma_E^\mu C_E = -\gamma_E^{\mu*} = -\gamma_E^{\mu T}, \qquad (A14)$$

$$(\gamma_E^5)^2 = -C_E^2 = 1 \qquad (A15)$$

In particular, by using Eq. (A13) and Eq. (30)—or Eq. (B5)—one can prove the $\gamma^5$ Hermiticity of the Wilson-Dirac operator $D$, or equivalently the $\gamma^5$ Hermiticity of the fermion propagator $S(x, y)$, as follows:

$$\gamma_E^5 D_{xy}^{R,\dagger} \gamma_E^5 = \gamma_E^5 (S_R(x,y)^{-1})^\dagger \gamma_E^5$$
$$= (4 + am_0^R)\delta_{xy} - \frac{1}{2}\sum_\mu ((1 + \gamma_{E\mu})U_\mu^{(R),\dagger}(x)\delta_{x+\mu,y}$$
$$+ (1 - \gamma_{E\mu})U_\mu^{(R)}(y)\delta_{x,y+\mu})$$
$$= S_R(y,x)^{-1} = D_{y,x}^R. \qquad (A16)$$

For the combinations of gamma matrices $(\Gamma^1, \Gamma^2) = (C\gamma^5, \mathbb{1}_4)$, that appear in Sec. IV, the following useful relation, which enters the derivation of Eq. (61), holds:

$$(\gamma_E^0 \Gamma^{1*} \gamma_E^0)^{\alpha\beta} (\gamma_E^0 \Gamma^{2\dagger} \gamma_E^0)^{\gamma\delta} = (\Gamma^1)^{\alpha\beta}(\Gamma^2)^{\gamma\delta}, \qquad (A17)$$

which descends from the fact that $\gamma_E^0$, $\gamma_E^2$, and $\gamma_E^5$ are real and Hermitian.

### 3. A basis of generators for ($f$) and ($as$) representations of $Sp(4)$

In the HMC/RHMC algorithms it is necessary to have an explicit expression for the generators for a given representation $R$ of $Sp(4)$ in order to compute the MD forces

---

[11]In this appendix, we denote with a subscript $M$ or $E$ the gamma matrices in Minkowski or Euclidean space, respectively. We suppress this subscript in the main body of the paper, hence, in Sec. II, we write $\gamma^\mu \equiv \gamma_M^\mu$. Similarly, in Sec. II we denote $\gamma^5 \equiv \gamma_M^5$ and $C \equiv C_M$.

[12]In Secs. III and IV, we omit the subscription $E$, and denote $\gamma^\mu \equiv \gamma_E^\mu$, $\gamma^5 \equiv \gamma_E^5$, and $C \equiv C_E$.

associated with the HMC/RHMC Hamiltonian. We make an explicit choice of basis, and report it here, for completeness. For the fundamental representation $T^A_{(f)}$, with $A = 1, 2, \ldots, 10$, our choice is the following:

$$T^1_{(f)} = \frac{1}{2}\begin{pmatrix} 1 & 0 & 0 & 0 \\ 0 & 0 & 0 & 0 \\ 0 & 0 & -1 & 0 \\ 0 & 0 & 0 & 0 \end{pmatrix}, \quad T^2_{(f)} = \frac{1}{2}\begin{pmatrix} 0 & 0 & 0 & 0 \\ 0 & 1 & 0 & 0 \\ 0 & 0 & 0 & 0 \\ 0 & 0 & 0 & -1 \end{pmatrix},$$

$$T^3_{(f)} = \frac{1}{2\sqrt{2}}\begin{pmatrix} 0 & i & 0 & 0 \\ -i & 0 & 0 & 0 \\ 0 & 0 & 0 & i \\ 0 & 0 & -i & 0 \end{pmatrix}, \quad T^4_{(f)} = \frac{1}{2\sqrt{2}}\begin{pmatrix} 0 & 1 & 0 & 0 \\ 1 & 0 & 0 & 0 \\ 0 & 0 & 0 & -1 \\ 0 & 0 & -1 & 0 \end{pmatrix},$$

$$T^5_{(f)} = \frac{1}{2}\begin{pmatrix} 0 & 0 & 1 & 0 \\ 0 & 0 & 0 & 0 \\ 1 & 0 & 0 & 0 \\ 0 & 0 & 0 & 0 \end{pmatrix}, \quad T^6_{(f)} = \frac{1}{2}\begin{pmatrix} 0 & 0 & i & 0 \\ 0 & 0 & 0 & 0 \\ -i & 0 & 0 & 0 \\ 0 & 0 & 0 & 0 \end{pmatrix},$$

$$T^7_{(f)} = \frac{1}{2}\begin{pmatrix} 0 & 0 & 0 & 0 \\ 0 & 0 & 0 & 1 \\ 0 & 0 & 0 & 0 \\ 0 & 1 & 0 & 0 \end{pmatrix}, \quad T^8_{(f)} = \frac{1}{2}\begin{pmatrix} 0 & 0 & 0 & 0 \\ 0 & 0 & 0 & i \\ 0 & 0 & 0 & 0 \\ 0 & -i & 0 & 0 \end{pmatrix},$$

$$T^9_{(f)} = \frac{1}{2\sqrt{2}}\begin{pmatrix} 0 & 0 & 0 & i \\ 0 & 0 & i & 0 \\ 0 & -i & 0 & 0 \\ -i & 0 & 0 & 0 \end{pmatrix}, \quad T^{10}_{(f)} = \frac{1}{2\sqrt{2}}\begin{pmatrix} 0 & 0 & 0 & 1 \\ 0 & 0 & 1 & 0 \\ 0 & 1 & 0 & 0 \\ 1 & 0 & 0 & 0 \end{pmatrix}. \tag{A18}$$

As discussed in Sec. III A, the generators for the antisymmetric representation of $Sp(4)$ appear in the infinitesimal transformation of the antisymmetric link variable in Eq. (29). We adopt the conventional basis of matrices $e_{(as)}$ given by

$$e^{(12)}_{(as)} = \frac{1}{\sqrt{2}}\begin{pmatrix} 0 & -1 & 0 & 0 \\ 1 & 0 & 0 & 0 \\ 0 & 0 & 0 & 0 \\ 0 & 0 & 0 & 0 \end{pmatrix}, \quad e^{(23)}_{(as)} = \frac{1}{\sqrt{2}}\begin{pmatrix} 0 & 0 & 0 & 0 \\ 0 & 0 & -1 & 0 \\ 0 & 1 & 0 & 0 \\ 0 & 0 & 0 & 0 \end{pmatrix},$$

$$e^{(14)}_{(as)} = \frac{1}{\sqrt{2}}\begin{pmatrix} 0 & 0 & 0 & -1 \\ 0 & 0 & 0 & 0 \\ 0 & 0 & 0 & 0 \\ 1 & 0 & 0 & 0 \end{pmatrix}, \quad e^{(24)}_{(as)} = \frac{1}{2}\begin{pmatrix} 0 & 0 & 1 & 0 \\ 0 & 0 & 0 & -1 \\ -1 & 0 & 0 & 0 \\ 0 & 1 & 0 & 0 \end{pmatrix},$$

$$e^{(34)}_{(as)} = \frac{1}{\sqrt{2}}\begin{pmatrix} 0 & 0 & 0 & 0 \\ 0 & 0 & 0 & 0 \\ 0 & 0 & 0 & -1 \\ 0 & 0 & 1 & 0 \end{pmatrix}, \tag{A19}$$

With this convention we find the following expressions of the generators for the antisymmetric representation of $Sp(4)$:

$$T^1_{(as)} = \frac{1}{2}\begin{pmatrix} 1 & 0 & 0 & 0 & 0 \\ 0 & -1 & 0 & 0 & 0 \\ 0 & 0 & 1 & 0 & 0 \\ 0 & 0 & 0 & 0 & 0 \\ 0 & 0 & 0 & 0 & -1 \end{pmatrix}, \quad T^2_{(as)} = \frac{1}{2}\begin{pmatrix} 1 & 0 & 0 & 0 & 0 \\ 0 & 1 & 0 & 0 & 0 \\ 0 & 0 & -1 & 0 & 0 \\ 0 & 0 & 0 & 0 & 0 \\ 0 & 0 & 0 & 0 & -1 \end{pmatrix},$$

$$T^3_{(as)} = \frac{-i}{2}\begin{pmatrix} 0 & 0 & 0 & 0 & 0 \\ 0 & 0 & 0 & -1 & 0 \\ 0 & 0 & 0 & -1 & 0 \\ 0 & 1 & 1 & 0 & 0 \\ 0 & 0 & 0 & 0 & 0 \end{pmatrix}, \quad T^4_{(as)} = \frac{1}{2}\begin{pmatrix} 0 & 0 & 0 & 0 & 0 \\ 0 & 0 & 0 & -1 & 0 \\ 0 & 0 & 0 & 1 & 0 \\ 0 & -1 & 1 & 0 & 0 \\ 0 & 0 & 0 & 0 & 0 \end{pmatrix},$$

$$T^5_{(as)} = \frac{1}{2}\begin{pmatrix} 0 & -1 & 0 & 0 & 0 \\ -1 & 0 & 0 & 0 & 0 \\ 0 & 0 & 0 & 0 & 1 \\ 0 & 0 & 0 & 0 & 0 \\ 0 & 0 & 1 & 0 & 0 \end{pmatrix}, \quad T^6_{(as)} = \frac{-i}{2}\begin{pmatrix} 0 & 1 & 0 & 0 & 0 \\ -1 & 0 & 0 & 0 & 0 \\ 0 & 0 & 0 & 0 & -1 \\ 0 & 0 & 0 & 0 & 0 \\ 0 & 0 & 1 & 0 & 0 \end{pmatrix},$$

$$T^7_{(as)} = \frac{1}{2}\begin{pmatrix} 0 & 0 & 1 & 0 & 0 \\ 0 & 0 & 0 & 0 & -1 \\ 1 & 0 & 0 & 0 & 0 \\ 0 & 0 & 0 & 0 & 0 \\ 0 & -1 & 0 & 0 & 0 \end{pmatrix}, \quad T^8_{(as)} = \frac{-i}{2}\begin{pmatrix} 0 & 0 & -1 & 0 & 0 \\ 0 & 0 & 0 & 0 & 1 \\ 1 & 0 & 0 & 0 & 0 \\ 0 & 0 & 0 & 0 & 0 \\ 0 & -1 & 0 & 0 & 0 \end{pmatrix},$$

$$T^9_{(as)} = \frac{-i}{2}\begin{pmatrix} 0 & 0 & 0 & 1 & 0 \\ 0 & 0 & 0 & 0 & 0 \\ 0 & 0 & 0 & 0 & 0 \\ -1 & 0 & 0 & 0 & -1 \\ 0 & 0 & 0 & 1 & 0 \end{pmatrix}, \quad T^{10}_{(as)} = \frac{1}{2}\begin{pmatrix} 0 & 0 & 0 & -1 & 0 \\ 0 & 0 & 0 & 0 & 0 \\ 0 & 0 & 0 & 0 & 0 \\ -1 & 0 & 0 & 0 & 1 \\ 0 & 0 & 0 & 1 & 0 \end{pmatrix}. \tag{A20}$$

## APPENDIX B: MORE ABOUT CHIMERA BARYONS ON THE LATTICE

In the discussion in the main text, we wrote the correlation function $C_{\mathrm{CB}}(t - t_0)$ involving the chimera baryon operator appearing in $\mathcal{O}_{\mathrm{CB},4}$ and $\mathcal{O}_{\mathrm{CB},5}$ in Eq. (21). It is worth checking that $C_{\mathrm{CB}}(t - t_0)$ built from a different choice of element of $\mathcal{O}_{\mathrm{CB}} \sim 4$ of the global $Sp(4)$ symmetry gives rise to the same results. To this purpose, let us consider the combination of the interpolating operators $\frac{1}{2}(\mathcal{O}_{\mathrm{CB},1} + i\mathcal{O}_{\mathrm{CB},2})$:

$$\mathcal{O}^{k\gamma}_{\mathrm{CB}}(x) = (\overline{Q^{1\,a}}(x)\gamma^5 Q^{2\,b}(x))\Omega_{bc}\delta^{\gamma\delta}\Psi^{k\,ca}_\delta(x), \tag{B1}$$

and its Dirac conjugate

$$\overline{\mathcal{O}_{\text{CB}}^{k}}^{\gamma}(x) = \delta^{\gamma\delta}\overline{\Psi^{kca}}_{\delta}(x)\Omega^{cb}(\overline{Q^{2b}}(x)\gamma^5 Q^{1a}(x)). \quad \text{(B2)}$$

Then, the corresponding 2-point correlation function is

$$\langle\mathcal{O}_{\text{CB}}^{k\gamma}(x)\overline{\mathcal{O}_{\text{CB}}^{k}}^{\gamma'}(y)\rangle$$
$$= -\Omega_{bc}\Omega^{c'b'}\delta^{\gamma\delta}\delta^{\gamma'\delta'}S_{\Psi c'\,d'\,\delta\delta'}^{k\,ca}(x,y)S_{Qb'\,\beta\beta'}^{2b}(x,y)\gamma^{5\beta'\alpha'}$$
$$\times S_{Qa\,\alpha'\alpha}^{1\,a'}(y,x)\gamma^{5\alpha\beta}. \quad \text{(B3)}$$

To see the equivalence between Eqs. (B3) and (62) with the choice of $(\Gamma^1,\Gamma^2) = (C\gamma^5,\mathbb{1})$, we will use the following properties. First of all, for a symplectic unitary matrix $\mathcal{U}\in Sp(4)$:

$$\Omega^{-1}\mathcal{U}\Omega = \mathcal{U}^*. \quad \text{(B4)}$$

We next consider the inverse of the fermion propagator in the Wilson-Dirac formalism

$$S_Q(x,y)^{-1} = \langle Q(x)\bar{Q}(y)\rangle^{-1}$$
$$= (4 + am_0^f)\delta_{xy} - \frac{1}{2}\sum_\mu((1-\gamma_\mu)U_\mu^{(f)}(x)\delta_{x+\mu,y}$$
$$+ (1+\gamma_\mu)U_\mu^{(f),\dagger}(y)\delta_{x,y+\mu}). \quad \text{(B5)}$$

By applying the transpose and the charge conjugation operator to $S_Q^{-1}$, we have

$$C^T(S_Q(x,y)^{-1})^T C$$
$$= (4 + am_0^f)\delta_{xy} - \frac{1}{2}\sum_\mu((1+\gamma_\mu)U_\mu^{(f),T}(x)\delta_{x+\mu,y}$$
$$+ (1-\gamma_\mu)U_\mu^{(f),*}(y)\delta_{x,y+\mu}). \quad \text{(B6)}$$

Using Eq. (B4), we arrive at

$$\Omega^{-1}C^T(S_Q(x,y)^{-1})^T C\Omega$$
$$= (4 + am_0^f)\delta_{xy} - \frac{1}{2}\sum_\mu((1+\gamma_\mu)U_\mu^{(f),\dagger}(x)\delta_{x+\mu,y}$$
$$+ (1-\gamma_\mu)U_\mu^{(f)}(y)\delta_{x,y+\mu})$$
$$= S_Q(y,x)^{-1}, \quad \text{(B7)}$$

which in turn implies that

$$\Omega^{-1}C^T S_Q^T(x,y)C\Omega = S_Q(y,x). \quad \text{(B8)}$$

Using this result, with $\Gamma^1 = C\gamma^5$ and $\Gamma^2 = \mathbb{1}$, we can rewrite Eq. (62) as

$$\langle\mathcal{O}_{\text{CB}}^{k}{}^{\gamma}(x)\overline{\mathcal{O}_{\text{CB}}^{k}}^{\gamma'}(y)\rangle$$
$$= \Omega_{da}\Omega^{d'a'}\delta^{\gamma\delta}\delta^{\gamma'\delta'}S_{\Psi c'd'\,\delta\delta'}^{k\,cd}(x,y)$$
$$\times \text{Tr}_s[S_{Qa'}^{2\,a}(x,y)\gamma^5(\Omega^{-1}C^T(S_Q^1(x,y))^T C\Omega)^{c'}{}_c\gamma^5]$$
$$= \Omega_{da}\Omega^{d'a'}\delta^{\gamma\delta}\delta^{\gamma'\delta'}S_{\Psi c'd'\,\delta\delta'}^{k\,cd}(x,y)$$
$$\times \text{Tr}_s[S_{Qa'}^{2\,a}(x,y)\gamma^5 S_{Qc}^{1\,c'}(y,x)\gamma^5]. \quad \text{(B9)}$$

Comparing Eqs. (B3) and (B9), we conclude that the chimera propagators built out of $\mathcal{O}_{\text{CB},1(2)}$ and $\mathcal{O}_{\text{CB},4(5)}$ are identical to one another.

## APPENDIX C: TABLES OF NUMERICAL RESULTS

In this appendix, we tabulate some numerical information relevant to the discussions in Secs. V C–V E. The parameters of the lattice theory are $\beta = 6.5$, $am_0^{as} = -1.01$ and $am_0^f = -0.71$. The baryonic and mesonic observables are measured using point and stochastic wall sources, respectively. The numerical results are presented in lattice units.

TABLE III. Ensembles generated for the numerical study of finite-volume effects reported in Sec. V C. $N_t$ and $N_s$ are the temporal and spatial extents of the lattice, while $N_{\text{conf}}$ and $\delta_{\text{traj}}$ denote the number of configurations and the length of the Monte Carlo trajectory between adjacent configurations. In the last column, we show the average plaquette value $\langle\mathcal{P}\rangle$.

| Ensemble | $N_t \times N_s^3$ | $N_{\text{conf}}$ | $\delta_{\text{traj}}$ | $\langle\mathcal{P}\rangle$ |
|---|---|---|---|---|
| E1 | $36 \times 8^3$ | 160 | 24 | 0.585758(87) |
| E2 | $48 \times 12^3$ | 130 | 24 | 0.585447(51) |
| E3 | $48 \times 16^3$ | 140 | 20 | 0.585233(34) |
| E4 | $48 \times 18^3$ | 180 | 12 | 0.585234(22) |
| E5 | $48 \times 20^3$ | 130 | 12 | 0.585137(20) |
| E6 | $48 \times 24^3$ | 165 | 8 | 0.585148(13) |
| E7 | $54 \times 28^3$ | 180 | 12 | 0.585144(11) |

TABLE IV. Numerical results for the masses and decay constants of pseudoscalar mesons (PS), and the masses of vector mesons (V), used to investigate finite-volume effects in Sec. V C. The constituent fermions are in the fundamental representation. The pseudoscalar mass at infinite volume, $am_{\text{PS}}^{f,\text{inf}}$, is the one extracted from the ensemble with the largest volume, $54 \times 28^3$.

| Ensemble | $am_{\text{PS}}^f$ | $am_{\text{V}}^f$ | $af_{\text{PS}}^f$ | $m_{\text{PS}}^{f,\text{inf}}L$ |
|---|---|---|---|---|
| E1 | 0.7488(64) | 0.7982(72) | 0.0349(20) | 2.8783(76) |
| E2 | 0.5171(48) | 0.5685(51) | 0.0419(17) | 4.317(11) |
| E3 | 0.3849(45) | 0.4238(58) | 0.0427(14) | 5.757(15) |
| E4 | 0.3778(22) | 0.4290(24) | 0.0461(11) | 6.476(17) |
| E5 | 0.3702(16) | 0.4142(22) | 0.05151(88) | 7.196(19) |
| E6 | 0.3640(19) | 0.4067(20) | 0.04992(87) | 8.635(23) |
| E7 | 0.35979(95) | 0.4009(11) | 0.05058(61) | 10.074(27) |

TABLE V.   Numerical results for the masses and decay constants of pseudoscalar mesons (PS), and the masses of vector mesons (V), used to investigate finite-volume effects in Sec. V C. The constituent fermions are in the antisymmetric representation. We also list, in the last column, the mass of chimera baryons with positive parity.

| Ensemble | $am_{\mathrm{PS}}^{as}$ | $am_{\mathrm{V}}^{as}$ | $af_{\mathrm{PS}}^{as}$ | $am_{\mathrm{CB}}^{+}$ |
|---|---|---|---|---|
| E1 | 0.4277(53) | 0.4411(60) | 0.0843(32) | 1.012(16) |
| E2 | 0.5499(35) | 0.5814(47) | 0.0781(20) | 0.927(15) |
| E3 | 0.5858(21) | 0.6241(33) | 0.0767(15) | 0.768(13) |
| E4 | 0.5956(14) | 0.6395(21) | 0.0794(12) | 0.7974(72) |
| E5 | 0.6017(10) | 0.6491(15) | 0.08349(96) | 0.7803(60) |
| E6 | 0.6023(12) | 0.6481(14) | 0.0805(12) | 0.7654(50) |
| E7 | 0.60205(92) | 0.6450(15) | 0.08313(88) | 0.7636(28) |

TABLE VI.   Numerical results for the masses of mesons in additional spin-0 and spin-1 channels, sourced by the interpolating operators in Eq. (46). The representation of the constituent fermions are denoted by superscripts *f* and *as*. The measurements are performed on the ensemble with the largest volume, E7.

| Ensemble | $am_{\mathrm{T}}^{f}$ | $am_{\mathrm{AV}}^{f}$ | $am_{\mathrm{AT}}^{f}$ | $am_{\mathrm{S}}^{f}$ | $am_{\mathrm{T}}^{as}$ | $am_{\mathrm{AV}}^{as}$ | $am_{\mathrm{AT}}^{as}$ | $am_{\mathrm{S}}^{f}$ |
|---|---|---|---|---|---|---|---|---|
| E7 | 0.3995(13) | 0.544(10) | 0.543(11) | 0.508(12) | 0.6461(14) | 0.859(12) | 0.889(14) | 0.843(11) |

In Table III, we list the details characterizing the ensembles used for our investigations of finite-volume effects. The ensembles denoted by E6 and E7 are also used for numerical studies of the chimera baryon and the combined spectrum, respectively. We save configurations separated by $\delta_{\mathrm{traj}}$ trajectories, after discarding a sufficiently large number of initial trajectories to allow for the thermalization, so that those are independent to each other. We determine $\delta_{\mathrm{traj}}$ by monitoring the average plaquette values $\langle \mathcal{P} \rangle$, and chose it to be comparable to one autocorrelation length.

In Tables IV and V, we present the results of the measurements of the masses of the pseudoscalar (PS) and vector (V) mesons composed of fermionic constituents in the fundamental and antisymmetric representations, and the decay constant of the pseudoscalar meson. We also show the mass of the chimera baryon (CB) with positive parity, and $m_{\mathrm{PS}}^{f,\mathrm{inf}} L$—$am_{\mathrm{PS}}^{f,\mathrm{inf}}$ is extracted from the measurement on the ensemble with the largest available lattice.

In Table VI, we present the numerical results for the masses of the other mesons in the spin-0 and spin-1 channels, besides the ones we have already presented in Tables IV and V. These are sourced by the tensor (T), axial-vector (AV), axial-tensor (AT), and scalar (S) interpolating operators defined with the gamma structures in Eq. (46). These measurements have been carried out by using ensemble E7, the one that has the largest volume.

[1] G. Aad *et al.* (ATLAS Collaboration), Observation of a new particle in the search for the Standard Model Higgs boson with the ATLAS detector at the LHC, Phys. Lett. B **716**, 1 (2012).

[2] S. Chatrchyan *et al.* (CMS Collaboration), Observation of a new boson at a mass of 125 GeV with the CMS experiment at the LHC, Phys. Lett. B **716**, 30 (2012).

[3] J. Barnard, T. Gherghetta, and T. S. Ray, UV descriptions of composite Higgs models without elementary scalars, J. High Energy Phys. 02 (**2014**) 002.

[4] D. B. Kaplan and H. Georgi, SU(2) × U(1) breaking by vacuum misalignment, Phys. Lett. **136B**, 183 (1984).

[5] H. Georgi and D. B. Kaplan, Composite Higgs and custodial SU(2), Phys. Lett. **145B**, 216 (1984).

[6] M. J. Dugan, H. Georgi, and D. B. Kaplan, Anatomy of a composite Higgs model, Nucl. Phys. **B254**, 299 (1985).

[7] G. Panico and A. Wulzer, The composite Nambu-Goldstone Higgs, Lect. Notes Phys. **913**, 1 (2016).

[8] O. Witzel, Review on composite Higgs models, Proc. Sci., LATTICE2018 (**2019**) 006.

[9] G. Cacciapaglia, C. Pica, and F. Sannino, Fundamental composite dynamics: A review, Phys. Rep. **877**, 1 (2020).

[10] G. Ferretti and D. Karateev, Fermionic UV completions of composite Higgs models, J. High Energy Phys. 03 (**2014**) 077.

[11] G. Ferretti, Gauge theories of partial compositeness: Scenarios for Run-II of the LHC, J. High Energy Phys. 06 (**2016**) 107.

[12] G. Cacciapaglia, G. Ferretti, T. Flacke, and H. Serôdio, Light scalars in composite Higgs models, Front. Phys. **7,** 22 (2019).

[13] E. Katz, A. E. Nelson, and D. G. E. Walker, The intermediate Higgs, J. High Energy Phys. 08 (2005) 074.

[14] R. Barbieri, B. Bellazzini, V. S. Rychkov, and A. Varagnolo, The Higgs boson from an extended symmetry, Phys. Rev. D **76,** 115008 (2007).

[15] P. Lodone, Vector-like quarks in a composite Higgs model, J. High Energy Phys. 12 (2008) 029.

[16] B. Gripaios, A. Pomarol, F. Riva, and J. Serra, Beyond the minimal composite Higgs model, J. High Energy Phys. 04 (2009) 070.

[17] J. Mrazek, A. Pomarol, R. Rattazzi, M. Redi, J. Serra, and A. Wulzer, The other natural two Higgs doublet model, Nucl. Phys. **B853,** 1 (2011).

[18] D. Marzocca, M. Serone, and J. Shu, General composite Higgs models, J. High Energy Phys. 08 (2012) 013.

[19] C. Grojean, O. Matsedonskyi, and G. Panico, Light top partners and precision physics, J. High Energy Phys. 10 (2013) 160.

[20] G. Cacciapaglia and F. Sannino, Fundamental composite (Goldstone) Higgs dynamics, J. High Energy Phys. 04 (2014) 111.

[21] G. Ferretti, UV completions of partial compositeness: The case for a SU(4) gauge group, J. High Energy Phys. 06 (2014) 142.

[22] A. Arbey, G. Cacciapaglia, H. Cai, A. Deandrea, S. Le Corre, and F. Sannino, Fundamental composite electroweak dynamics: Status at the LHC, Phys. Rev. D **95,** 015028 (2017).

[23] G. Cacciapaglia, H. Cai, A. Deandrea, T. Flacke, S. J. Lee, and A. Parolini, Composite scalars at the LHC: The Higgs, the sextet and the octet, J. High Energy Phys. 11 (2015) 201.

[24] F. Feruglio, B. Gavela, K. Kanshin, P. A. N. Machado, S. Rigolin, and S. Saa, The minimal linear sigma model for the Goldstone Higgs, J. High Energy Phys. 06 (2016) 038.

[25] T. DeGrand, M. Golterman, E. T. Neil, and Y. Shamir, One-loop chiral perturbation theory with two fermion representations, Phys. Rev. D **94,** 025020 (2016).

[26] S. Fichet, G. von Gersdorff, E. Pontòn, and R. Rosenfeld, The excitation of the global symmetry-breaking vacuum in composite Higgs models, J. High Energy Phys. 09 (2016) 158.

[27] J. Galloway, A. L. Kagan, and A. Martin, A UV complete partially composite-pNGB Higgs, Phys. Rev. D **95,** 035038 (2017).

[28] A. Agugliaro, O. Antipin, D. Becciolini, S. De Curtis, and M. Redi, UV complete composite Higgs models, Phys. Rev. D **95,** 035019 (2017).

[29] A. Belyaev, G. Cacciapaglia, H. Cai, G. Ferretti, T. Flacke, A. Parolini, and H. Serodio, Di-boson signatures as standard candles for partial compositeness, J. High Energy Phys. 01 (2017) 094.

[30] C. Csaki, T. Ma, and J. Shu, Maximally Symmetric Composite Higgs Models, Phys. Rev. Lett. **119,** 131803 (2017).

[31] M. Chala, G. Durieux, C. Grojean, L. de Lima, and O. Matsedonskyi, Minimally extended SILH, J. High Energy Phys. 06 (2017) 088.

[32] M. Golterman and Y. Shamir, Effective potential in ultraviolet completions for composite Higgs models, Phys. Rev. D **97,** 095005 (2018).

[33] C. Csaki, T. Ma, and J. Shu, Trigonometric Parity for Composite Higgs Models, Phys. Rev. Lett. **121,** 231801 (2018).

[34] T. Alanne, D. B. Franzosi, and M. T. Frandsen, A partially composite Goldstone Higgs, Phys. Rev. D **96,** 095012 (2017).

[35] T. Alanne, D. Buarque Franzosi, M. T. Frandsen, M. L. A. Kristensen, A. Meroni, and M. Rosenlyst, Partially composite Higgs models: Phenomenology and RG analysis, J. High Energy Phys. 01 (2018) 051.

[36] F. Sannino, P. Stangl, D. M. Straub, and A. E. Thomsen, Flavor physics and flavor anomalies in minimal fundamental partial compositeness, Phys. Rev. D **97,** 115046 (2018).

[37] T. Alanne, N. Bizot, G. Cacciapaglia, and F. Sannino, Classification of NLO operators for composite Higgs models, Phys. Rev. D **97,** 075028 (2018).

[38] N. Bizot, G. Cacciapaglia, and T. Flacke, Common exotic decays of top partners, J. High Energy Phys. 06 (2018) 065.

[39] C. Cai, G. Cacciapaglia, and H. H. Zhang, Vacuum alignment in a composite 2HDM, J. High Energy Phys. 01 (2019) 130.

[40] A. Agugliaro, G. Cacciapaglia, A. Deandrea, and S. De Curtis, Vacuum misalignment and pattern of scalar masses in the SU(5)/SO(5) composite Higgs model, J. High Energy Phys. 02 (**2019**) 089.

[41] G. Cacciapaglia, T. Ma, S. Vatani, and Y. Wu, Towards a fundamental safe theory of composite Higgs and dark matter, Eur. Phys. J. C **80,** 1088 (2020).

[42] H. Gertov, A. E. Nelson, A. Perko, and D. G. E. Walker, Lattice-friendly gauge completion of a composite Higgs with top partners, J. High Energy Phys. 02 (2019) 181.

[43] V. Ayyar, M. Golterman, D. C. Hackett, W. Jay, E. T. Neil, Y. Shamir, and B. Svetitsky, Radiative contribution to the composite-Higgs potential in a two-representation lattice model, Phys. Rev. D **99,** 094504 (2019).

[44] G. Cacciapaglia, H. Cai, A. Deandrea, and A. Kushwaha, Composite Higgs and Dark Matter Model in SU(6)/SO(6), J. High Energy Phys. 10 (2019) 035.

[45] D. Buarque Franzosi and G. Ferretti, Anomalous dimensions of potential top-partners, SciPost Phys. **7,** 027 (2019).

[46] G. Cacciapaglia, S. Vatani, and C. Zhang, Composite Higgs meets Planck scale: Partial compositeness from partial unification, Phys. Lett. B **815,** 136177 (2021).

[47] G. Cacciapaglia, A. Deandrea, T. Flacke, and A. M. Iyer, Gluon-Photon signatures for color octet at the LHC (and beyond), J. High Energy Phys. 05 (2020) 027.

[48] Z. Y. Dong, C. S. Guan, T. Ma, J. Shu, and X. Xue, UV completed composite Higgs model with heavy composite partners, Phys. Rev. D **104,** 035013 (2021).

[49] G. Cacciapaglia, T. Flacke, M. Kunkel, and W. Porod, Phenomenology of unusual top partners in composite Higgs models, J. High Energy Phys. 02 (2022) 208.

[50] A. Banerjee, D. B. Franzosi, and G. Ferretti, Modelling vector-like quarks in partial compositeness framework, J. High Energy Phys. 03 (**2022**) 200.

[51] K. Agashe, R. Contino, and A. Pomarol, The minimal composite Higgs model, Nucl. Phys. **B719,** 165 (2005).

[52] R. Contino, L. Da Rold, and A. Pomarol, Light custodians in natural composite Higgs models, Phys. Rev. D **75,** 055014 (2007).

[53] A. Falkowski and M. Perez-Victoria, Electroweak breaking on a soft wall, J. High Energy Phys. 12 (2008) 107.

[54] J. Erdmenger, N. Evans, W. Porod, and K. S. Rigatos, Gauge/Gravity Dynamics for Composite Higgs Models and the Top Mass, Phys. Rev. Lett. **126,** 071602 (2021).

[55] J. Erdmenger, N. Evans, W. Porod, and K. S. Rigatos, Gauge/gravity dual dynamics for the strongly coupled sector of composite Higgs models, J. High Energy Phys. 02 (2021) 058.

[56] D. Elander, M. Frigerio, M. Knecht, and J. L. Kneur, Holographic models of composite Higgs in the Veneziano limit. Part I. Bosonic sector, J. High Energy Phys. 03 (2021) 182.

[57] D. Elander, M. Frigerio, M. Knecht, and J. L. Kneur, Holographic models of composite Higgs in the Veneziano limit. Part II. Fermionic sector, J. High Energy Phys. 05 (2022) 066.

[58] D. Elander and M. Piai, Towards top-down holographic composite Higgs: Minimal coset from maximal supergravity, J. High Energy Phys. 03 (2022) 049.

[59] N. Bizot, M. Frigerio, M. Knecht, and J. L. Kneur, Nonperturbative analysis of the spectrum of meson resonances in an ultraviolet-complete composite-Higgs model, Phys. Rev. D **95,** 075006 (2017).

[60] A. Hietanen, R. Lewis, C. Pica, and F. Sannino, Fundamental composite Higgs dynamics on the lattice: SU(2) with two flavors, J. High Energy Phys. 07 (2014) 116.

[61] W. Detmold, M. McCullough, and A. Pochinsky, Dark nuclei. II. Nuclear spectroscopy in two-color QCD, Phys. Rev. D **90,** 114506 (2014).

[62] R. Arthur, V. Drach, M. Hansen, A. Hietanen, C. Pica, and F. Sannino, SU(2) gauge theory with two fundamental flavors: A minimal template for model building, Phys. Rev. D **94,** 094507 (2016).

[63] R. Arthur, V. Drach, A. Hietanen, C. Pica, and F. Sannino, $SU(2)$ gauge theory with two fundamental flavours: Scalar and pseudoscalar spectrum, arXiv:1607.06654.

[64] C. Pica, V. Drach, M. Hansen, and F. Sannino, Composite Higgs dynamics on the lattice, EPJ Web Conf. **137,** 10005 (2017).

[65] J. W. Lee, B. Lucini, and M. Piai, Symmetry restoration at high-temperature in two-color and two-flavor lattice gauge theories, J. High Energy Phys. 04 (2017) 036.

[66] V. Drach, T. Janowski, and C. Pica, Update on SU(2) gauge theory with NF = 2 fundamental flavours, EPJ Web Conf. **175,** 08020 (2018).

[67] V. Drach, T. Janowski, C. Pica, and S. Prelovsek, Scattering of Goldstone bosons and resonance production in a composite Higgs model on the lattice, J. High Energy Phys. 04 (2021) 117.

[68] V. Drach, P. Fritzsch, A. Rago, and F. Romero-López, Singlet channel scattering in a composite Higgs model on the lattice, Eur. Phys. J. C **82,** 47 (2022).

[69] V. Ayyar, T. DeGrand, M. Golterman, D. C. Hackett, W. I. Jay, E. T. Neil, Y. Shamir, and B. Svetitsky, Spectroscopy of SU(4) composite Higgs theory with two distinct fermion representations, Phys. Rev. D **97,** 074505 (2018).

[70] V. Ayyar, T. DeGrand, D. C. Hackett, W. I. Jay, E. T. Neil, Y. Shamir, and B. Svetitsky, Baryon spectrum of SU(4) composite Higgs theory with two distinct fermion representations, Phys. Rev. D **97,** 114505 (2018).

[71] V. Ayyar, T. DeGrand, D. C. Hackett, W. I. Jay, E. T. Neil, Y. Shamir, and B. Svetitsky, Finite-temperature phase structure of SU(4) gauge theory with multiple fermion representations, Phys. Rev. D **97,** 114502 (2018).

[72] V. Ayyar, T. DeGrand, D. C. Hackett, W. I. Jay, E. T. Neil, Y. Shamir, and B. Svetitsky, Partial compositeness and baryon matrix elements on the lattice, Phys. Rev. D **99,** 094502 (2019).

[73] G. Cossu, L. Del Debbio, M. Panero, and D. Preti, Strong dynamics with matter in multiple representations: SU(4) gauge theory with fundamental and sextet fermions, Eur. Phys. J. C **79,** 638 (2019).

[74] Y. Shamir, M. Golterman, W. I. Jay, E. T. Neil, and B. Svetitsky, S parameter from a prototype composite-Higgs model, arXiv:2110.05198.

[75] L. Vecchi, A dangerous irrelevant UV-completion of the composite Higgs, J. High Energy Phys. 02 (2017) 094.

[76] T. Ma and G. Cacciapaglia, Fundamental composite 2HDM: SU(N) with 4 flavours, J. High Energy Phys. 03 (2016) 211.

[77] D. Buarque Franzosi, G. Cacciapaglia, and A. Deandrea, Sigma-assisted low scale composite Goldstone-Higgs, Eur. Phys. J. C **80,** 28 (2020).

[78] Y. Aoki, T. Aoyama, M. Kurachi, T. Maskawa, K. Miura, K.-i. Nagai, H. Ohki, E. Rinaldi, A. Shibata, K. Yamawaki, and T. Yamazaki (LatKMI Collaboration), Light composite scalar in eight-flavor QCD on the lattice, Phys. Rev. D **89,** 111502(R) (2014).

[79] Y. Aoki *et al.* (LatKMI Collaboration), Light flavor-singlet scalars and walking signals in $N_f = 8$ QCD on the lattice, Phys. Rev. D **96,** 014508 (2017).

[80] T. Appelquist *et al.*, Strongly interacting dynamics and the search for new physics at the LHC, Phys. Rev. D **93,** 114514 (2016).

[81] A. D. Gasbarro and G. T. Fleming, Examining the low energy dynamics of walking gauge theory, Proc. Sci., LATTICE2016 (**2017**) 242.

[82] T. Appelquist *et al.* (LSD Collaboration), Linear sigma EFT for nearly conformal gauge theories, Phys. Rev. D **98,** 114510 (2018).

[83] T. Appelquist *et al.* (Lattice Strong Dynamics Collaboration), Nonperturbative investigations of SU(3) gauge theory with eight dynamical flavors, Phys. Rev. D **99,** 014509 (2019).

[84] T. Appelquist *et al.* (Lattice Strong Dynamics (LSD) Collaboration), Goldstone boson scattering with a light composite scalar, Phys. Rev. D **105,** 034505 (2022).

[85] T. Appelquist, J. Ingoldby, and M. Piai, Nearly Conformal Composite Higgs Model, Phys. Rev. Lett. **126,** 191804 (2021).

[86] E. Bennett, D. K. Hong, J. W. Lee, C.-J. D. Lin, B. Lucini, M. Piai, and D. Vadacchino, Sp(4) gauge theory on the

lattice: Towards SU(4)/Sp(4) composite Higgs (and beyond), J. High Energy Phys. 03 (2018) 185.

[87] J. W. Lee, E. Bennett, D. K. Hong, C. J. D. Lin, B. Lucini, M. Piai, and D. Vadacchino, Progress in the lattice simulations of Sp(2N) gauge theories, Proc. Sci., LATTICE2018 (**2018**) 192.

[88] E. Bennett, D. K. Hong, J. W. Lee, C. J. D. Lin, B. Lucini, M. Piai, and D. Vadacchino, Sp(4) gauge theories on the lattice: $N_f = 2$ dynamical fundamental fermions, J. High Energy Phys. 12 (2019) 053.

[89] E. Bennett, D. K. Hong, J. W. Lee, C. J. D. Lin, B. Lucini, M. Mesiti, M. Piai, J. Rantaharju, and D. Vadacchino, $Sp(4)$ gauge theories on the lattice: Quenched fundamental and antisymmetric fermions, Phys. Rev. D **101**, 074516 (2020).

[90] E. Bennett, J. Holligan, D. K. Hong, J. W. Lee, C. J. D. Lin, B. Lucini, M. Piai, and D. Vadacchino, Color dependence of tensor and scalar glueball masses in Yang-Mills theories, Phys. Rev. D **102**, 011501(R) (2020).

[91] E. Bennett, J. Holligan, D. K. Hong, J. W. Lee, C. J. D. Lin, B. Lucini, M. Piai, and D. Vadacchino, Glueballs and strings in $Sp(2N)$ Yang-Mills theories, Phys. Rev. D **103**, 054509 (2021).

[92] K. Holland, M. Pepe, and U. J. Wiese, The deconfinement phase transition of Sp(2) and Sp(3) Yang-Mills theories in $(2 + 1)$-dimensions and $(3 + 1)$-dimensions, Nucl. Phys. **B694**, 35 (2004).

[93] Y. Hochberg, E. Kuflik, T. Volansky, and J. G. Wacker, Mechanism for Thermal Relic Dark Matter of Strongly Interacting Massive Particles, Phys. Rev. Lett. **113**, 171301 (2014).

[94] Y. Hochberg, E. Kuflik, H. Murayama, T. Volansky, and J. G. Wacker, Model for Thermal Relic Dark Matter of Strongly Interacting Massive Particles, Phys. Rev. Lett. **115**, 021301 (2015).

[95] Y. Hochberg, E. Kuflik, and H. Murayama, SIMP spectroscopy, J. High Energy Phys. 05 (2016) 090.

[96] N. Bernal, X. Chu, and J. Pradler, Simply split strongly interacting massive particles, Phys. Rev. D **95**, 115023 (2017).

[97] A. Berlin, N. Blinov, S. Gori, P. Schuster, and N. Toro, Cosmology and accelerator tests of strongly interacting dark matter, Phys. Rev. D **97**, 055033 (2018).

[98] N. Bernal, X. Chu, S. Kulkarni, and J. Pradler, Self-interacting dark matter without prejudice, Phys. Rev. D **101**, 055044 (2020).

[99] H. Cai and G. Cacciapaglia, Singlet dark matter in the SU(6)/SO(6) composite Higgs model, Phys. Rev. D **103**, 055002 (2021).

[100] Y. D. Tsai, R. McGehee, and H. Murayama, Resonant Self-Interacting Dark Matter from Dark QCD, Phys. Rev. Lett. **128**, 172001 (2022).

[101] A. Maas and F. Zierler, Strong isospin breaking in Sp(4) gauge theory, Proc. Sci., LATTICE2021 (**2021**) 130.

[102] F. Zierler and A. Maas, $Sp(4)$ SIMP dark matter on the lattice, Proc. Sci., LHCP2021 (**2021**) 162.

[103] S. Kulkarni, A. Maas, S. Mee, M. Nikolic, J. Pradler, and F. Zierler, Low-energy effective description of dark $Sp(4)$ theories, arXiv:2202.05191.

[104] B. Lucini and M. Teper, SU(N) gauge theories in four-dimensions: Exploring the approach to $N = $ infinity, J. High Energy Phys. 06 (**2001**) 050.

[105] B. Lucini, M. Teper, and U. Wenger, Glueballs and k-strings in SU(N) gauge theories: Calculations with improved operators, J. High Energy Phys. 06 (2004) 012.

[106] B. Lucini, A. Rago, and E. Rinaldi, Glueball masses in the large N limit, J. High Energy Phys. 08 (2010) 119.

[107] B. Lucini and M. Panero, SU(N) gauge theories at large N, Phys. Rep. **526**, 93 (2013).

[108] A. Athenodorou, R. Lau, and M. Teper, On the weak N-dependence of SO(N) and SU(N) gauge theories in $2 + 1$ dimensions, Phys. Lett. B **749**, 448 (2015).

[109] R. Lau and M. Teper, SO(N) gauge theories in $2 + 1$ dimensions: Glueball spectra and confinement, J. High Energy Phys. 10 (2017) 022.

[110] D. K. Hong, J. W. Lee, B. Lucini, M. Piai, and D. Vadacchino, Casimir scaling and Yang–Mills glueballs, Phys. Lett. B **775**, 89 (2017).

[111] N. Yamanaka, A. Nakamura, and M. Wakayama, Interglueball potential in lattice SU(N) gauge theories, arXiv:2110.04521.

[112] A. Athenodorou and M. Teper, SU(N) gauge theories in $3 + 1$ dimensions: Glueball spectrum, string tensions and topology, J. High Energy Phys. 12 (2021) 082.

[113] P. Hernández and F. Romero-López, The large $N_c$ limit of QCD on the lattice, Eur. Phys. J. A **57**, 52 (2021).

[114] F. Sannino, Conformal windows of SP(2N) and SO(N) gauge theories, Phys. Rev. D **79**, 096007 (2009).

[115] T. A. Ryttov and R. Shrock, Infrared fixed point physics in $SO(N_c)$ and $Sp(N_c)$ gauge theories, Phys. Rev. D **96**, 105015 (2017).

[116] B. S. Kim, D. K. Hong, and J. W. Lee, Into the conformal window: Multirepresentation gauge theories, Phys. Rev. D **101**, 056008 (2020).

[117] J. W. Lee, Conformal window from conformal expansion, Phys. Rev. D **103**, 076006 (2021).

[118] T. Appelquist, P. S. Rodrigues da Silva, and F. Sannino, Enhanced global symmetries and the chiral phase transition, Phys. Rev. D **60**, 116007 (1999).

[119] B. Lucini, E. Bennett, J. Holligan, D. K. Hong, H. Hsiao, J. W. Lee, C. J. D. Lin, M. Mesiti, M. Piai, and D. Vadacchino, Sp(4) gauge theories and beyond the standard model physics, EPJ Web Conf. **258**, 08003 (2022).

[120] E. Bennett, J. Holligan, D. K. Hong, H. Hsiao, J. W. Lee, C. J. D. Lin, B. Lucini, M. Mesiti, M. Piai, and D. Vadacchino, Progress in $Sp(2N)$ lattice gauge theories, arXiv:2111.14544.

[121] M. E. Peskin, The alignment of the vacuum in theories of technicolor, Nucl. Phys. **B175**, 197 (1980).

[122] M. Bando, T. Kugo, S. Uehara, K. Yamawaki, and T. Yanagida, Is $\rho$ Meson a Dynamical Gauge Boson of Hidden Local Symmetry?, Phys. Rev. Lett. **54**, 1215 (1985).

[123] R. Casalbuoni, S. De Curtis, D. Dominici, and R. Gatto, Effective weak interaction theory with possible new vector resonance from a strong Higgs sector, Phys. Lett. **155B**, 95 (1985).

[124] M. Bando, T. Kugo, and K. Yamawaki, Nonlinear realization and hidden local symmetries, Phys. Rep. **164**, 217 (1988).

[125] R. Casalbuoni, S. De Curtis, D. Dominici, F. Feruglio, and R. Gatto, Vector and axial vector bound states from a

strongly interacting electroweak sector, Int. J. Mod. Phys. A **04**, 1065 (1989).

[126] M. Harada and K. Yamawaki, Hidden local symmetry at loop: A new perspective of composite gauge boson and chiral phase transition, Phys. Rep. **381**, 1 (2003).

[127] H. Georgi, Vector realization of chiral symmetry, Nucl. Phys. **B331**, 311 (1990).

[128] M. Piai, A. Pierce, and J. G. Wacker, Composite vector mesons from QCD to the little Higgs, arXiv:hep-ph/0405242.

[129] D. Buarque Franzosi, G. Cacciapaglia, H. Cai, A. Deandrea, and M. Frandsen, Vector and axial-vector resonances in composite models of the Higgs boson, J. High Energy Phys. 11 (**2016**) 076.

[130] S. R. Coleman and E. J. Weinberg, Radiative corrections as the origin of spontaneous symmetry breaking, Phys. Rev. D **7**, 1888 (1973).

[131] A. G. Cohen and H. Georgi, Walking beyond the rainbow, Nucl. Phys. **B314**, 7 (1989).

[132] C. N. Leung, S. T. Love, and W. A. Bardeen, Aspects of dynamical symmetry breaking in gauge field theories, Nucl. Phys. **B323**, 493 (1989).

[133] D. B. Kaplan, Flavor at SSC energies: A new mechanism for dynamically generated fermion masses, Nucl. Phys. **B365**, 259 (1991).

[134] Y. Grossman and M. Neubert, Neutrino masses and mixings in nonfactorizable geometry, Phys. Lett. B **474**, 361 (2000).

[135] T. Gherghetta and A. Pomarol, Bulk fields and supersymmetry in a slice of AdS, Nucl. Phys. **B586**, 141 (2000).

[136] Z. Chacko and R. K. Mishra, Effective theory of a light dilaton, Phys. Rev. D **87**, 115006 (2013).

[137] L. Del Debbio, A. Patella, and C. Pica, Higher representations on the lattice: Numerical simulations. SU(2) with adjoint fermions, Phys. Rev. D **81**, 094503 (2010).

[138] N. Cabibbo and E. Marinari, A new method for updating SU(N) matrices in computer simulations of gauge theories, Phys. Lett. **119B**, 387 (1982).

[139] M. A. Clark and A. D. Kennedy, The RHMC algorithm for two flavors of dynamical staggered fermions, Nucl. Phys. B, Proc. Suppl. **129**, 850 (2004).

[140] T. Takaishi and P. de Forcrand, Testing and tuning new symplectic integrators for hybrid Monte Carlo algorithm in lattice QCD, Phys. Rev. E **73**, 036706 (2006).

[141] T. A. DeGrand and P. Rossi, Conditioning techniques for dynamical fermions, Comput. Phys. Commun. **60**, 211 (1990).

[142] T. Banks and A. Casher, Chiral symmetry breaking in confining theories, Nucl. Phys. **B169**, 103 (1980).

[143] J. J. M. Verbaarschot, The Spectrum of the QCD Dirac Operator and Chiral Random Matrix Theory: The Threefold Way, Phys. Rev. Lett. **72**, 2531 (1994).

[144] J. J. M. Verbaarschot and T. Wettig, Random matrix theory and chiral symmetry in QCD, Annu. Rev. Nucl. Part. Sci. **50**, 343 (2000).

[145] S. Hands, I. Montvay, S. Morrison, M. Oevers, L. Scorzato, and J. Skullerud, Numerical study of dense adjoint matter in two color QCD, Eur. Phys. J. C **17**, 285 (2000).

[146] M. Lüscher, Properties and uses of the Wilson flow in lattice QCD, J. High Energy Phys. 08 (2010) 071; 03 (2014) 092(E).

[147] M. Lüscher, Future applications of the Yang-Mills gradient flow in lattice QCD, Proc. Sci., LATTICE2013 (**2014**) 016.

[148] G. P. Lepage, The analysis of algorithms for lattice field theory, in *Proceedings of TASI, Boulder, CO* (Report No. CLNS-89-971, 1989), pp. 97–120.

[149] P. A. Boyle, A. Juttner, C. Kelly, and R. D. Kenway, Use of stochastic sources for the lattice determination of light quark physics, J. High Energy Phys. 08 (2008) 086.

[150] S. Gusken, A study of smearing techniques for hadron correlation functions, Nucl. Phys. B, Proc. Suppl. **17**, 361 (1990).

[151] M. Albanese *et al.* (APE Collaboration), Glueball masses and string tension in lattice QCD, Phys. Lett. B **192**, 163 (1987).

[152] M. Luscher and U. Wolff, How to calculate the elastic scattering matrix in two-dimensional quantum field theories by numerical simulation, Nucl. Phys. **B339**, 222 (1990).

[153] B. Blossier, M. Della Morte, G. von Hippel, T. Mendes, and R. Sommer, On the generalized eigenvalue method for energies and matrix elements in lattice field theory, J. High Energy Phys. 04 (2009) 094.

[154] E. Bennett, D. K. Hong, H. Hsiao, J. W. Lee, C. J. D. Lin, B. Lucini, M. Piai, and D. Vadacchino, Sp(4) theories on the lattice: Dynamical antisymmetric fermions (to be published).

[155] L. Del Debbio, L. Giusti, M. Luscher, R. Petronzio, and N. Tantalo, Stability of lattice QCD simulations and the thermodynamic limit, J. High Energy Phys. 02 (2006) 011.

[156] G. Martinelli and Y. C. Zhang, The connection between local operators on the lattice and in the continuum and its relation to meson decay constants, Phys. Lett. **123B**, 433 (1983).

[157] G. P. Lepage and P. B. Mackenzie, On the viability of lattice perturbation theory, Phys. Rev. D **48**, 2250 (1993).

[158] I. Montvay and G. Munster, *Quantum Fields on a Lattice* (Cambridge University Press. Cambridge, England, 1994), 10.1017/CBO9780511470783.

[159] E. Bennett, D. K. Hong, H. Hsiao, J. W. Lee, C. J. D. Lin, B. Lucini, M. Mesiti, M. Piai, and D. Vadacchino, Lattice studies of the Sp(4) gauge theory with two fundamental and three antisymmetric Dirac fermions—Data release (v1.1.0) [Data set], Zenodo, 10.5281/zenodo.6637515 (2022).

[160] E. Bennett, D. K. Hong, H. Hsiao, J. W. Lee, C. J. D. Lin, B. Lucini, M. Mesiti, M. Piai, and D. Vadacchino, Lattice studies of the Sp(4) gauge theory with two fundamental and three antisymmetric Dirac fermions—Code release (v1.1.0), Zenodo, 10.5281/zenodo.6637743 (2022).

[161] D. Arndt and C. J. D. Lin, Heavy meson chiral perturbation theory in finite volume, Phys. Rev. D **70**, 014503 (2004).

[162] J. Bijnens and J. Lu, Technicolor and other QCD-like theories at next-to-next-to-leading order, J. High Energy Phys. 11 (2009) 116.